Technical University
of Munich

Max Planck Institute
for Physics

Characterization and mitigation of the background in KATRIN

Charakterisierung und Reduktion des Untergrundes in KATRIN

Anna Katharina Schaller

Vollständiger Abdruck der von der Fakultät für Physik der Technischen Universität München zur Erlangung des akademischen Grades eines

Doktor der Naturwissenschaften (Dr. rer. nat.)

genehmigten Dissertation.

Vorsitzender:

Prof. Dr. Alejandro Ibarra

Prüfer der Dissertation:

Prof. Dr. Susanne Mertens

Prof. Dr. Lothar Oberauer

Die Dissertation wurde am 24.07.2020 bei der Technischen Universität München eingereicht und durch die Fakultät für Physik am 12.08.2020 angenommen.

Doctoral supervisor: Prof. Dr. Susanne Mertens

Document compiled on September 17, 2020.

Abstract

The **Ka**rlsruhe **Tri**tium **N**eutrino (KATRIN) experiment is designed to determine the neutrino mass with a sensitivity of 0.2 eV at 90 % C.L. in a model-independent way by investigating the tritium β-decay spectrum close to the endpoint. A low background rate is crucial to achieve this goal. Currently, the design background level is exceeded by more than one magnitude. Within this thesis the origin of this background is investigated by means of dedicated test measurements at the KATRIN **m**ain **s**pectrometer. Further, the background properties were characterized for the first neutrino mass results published in 2019. Finally, a novel technique to reduce the background by up to a factor of two based on an optimized electromagnetic field configuration, the **S**hifted **A**nalyzing **P**lane approach, was successfully tested.

Zusammenfassung

Das Ziel des **Ka**rlsruhe **Tri**tium **N**eutrino (KATRIN) Experiments ist eine modellunabhängige Bestimmung der Neutrinomasse mit einer Sensitivität von 0.2 eV (90 % C.L.). Dafür wird das Tritium β-Spektrum nahe dem Endpunkt präzise vermessen. Um die angestrebte Sensitivität zu erreichen ist eine sehr niedrige Untergrundrate wesentlich. Derzeit ist die angestrebte Untergrundrate um mehr als eine Größenordnung überschritten. In dieser Arbeit wurde die Ursache dieses Untergrundes anhand spezieller Messungen am KATRIN Hauptspektrometer untersucht. Des Weiteren wurden die Untergrundeigenschaften für das erste Neutrinomassenergebnis, welches 2019 veröffentlicht wurde, charakterisiert. Letztlich wurde ein neuer Ansatz zur Reduktion der Untergrundrate, basierend auf einer optimierten elektromagnetischen Feldkonfiguration, erfolgreich getestet. Diese sogenannte verschobene Analysierebene ermöglicht eine Reduktion der Untergrundrate um mehr als einen Faktor zwei.

Contents

Acronyms

1 Introduction

"All men by nature desire to know"

Aristotle

This striving resulted in the understanding of physics as we know it today. Research is continuously driven by theoretical predictions and experimental observations that raise new insights and questions. One example is the development of neutrino physics. Although the neutrino is the second most abundant particle within our universe it was not predicted until the year 1930 [1]. Given the extraordinary properties of this particle, causing it to interact only weakly, it took many years until its actual existence was experimentally confirmed in 1956 [2]. Still today neutrino physics remains a challenging and exciting research area. The observation of neutrino oscillation in the year 2001 [3] represents an important milestone in the history of neutrinos. It proved that neutrinos are massive particles. Since the absolute mass scale can not be accessed in oscillation experiments, this observation encouraged the so far efforts of determining the absolute neutrino mass. Several experimental approaches are pursued in this regard [4, 5, 6]. A promising way is the study of the tritium β-decay spectrum. This method does not depend on the neutrino's nature and offers a high sensitivity.

To improve the sensitivity to the neutrino mass the **Ka**rlsruhe **Tri**tium **N**eutrino (KATRIN) experiment [4] was designed as a successor of the Mainz [7] and Troitsk [8] experiments. These experiments improved laboratory upper limits on the neutrino mass to $m_\nu < 2.3\,\mathrm{eV}$ at 95 % C.L. (Mainz) and $m_\nu < 2.05\,\mathrm{eV}$ at 95 % C.L. (Troitsk). KATRIN targets a neutrino mass sensitivity of 0.2 eV at 90 % C.L. by investigating the tritium β-decay spectrum close to the endpoint. To reach this goal KATRIN employs a higher luminosity tritium source together with a spectrometer of improved resolution compared to the former experiments. An additional major performance requirement is a low background rate of less than 100 mcps. Currently the background rate exceeds its technical design value of 10 mcps by more than an order of magnitude[1]. The largest part of this background origins from processes within the spectrometer. It is hence essential for the experiment's success to understand and mitigate contributing

[1] By the time of **K**atrin **N**eutrino **M**ass 1 (KNM1) the background rate is 292 mcps on 117 detector pixels. For KNM2 the background already improved to 221 mcps on 117 pixels.

background processes. This is the main subject of the thesis at hand which focuses on:

- Detailed characterization of the dominant background component: The associated background model is reviewed by measurements of the electron energy spectrum and an experimental simulation with an radioactive source.
- Background characteristics during the first neutrino mass measurement: Based on the background properties during this campaign and in reference measurements the inputs for the analysis of the measured tritium spectrum are defined.
- Background mitigation: A potential strategy, the so-called **S**hifted **A**nalyzing **P**lane, for background mitigation is studied. Based on first test and characterization measurements the achievable neutrino mass uncertainty is calculated under consideration of associated systematics.

The thesis is structured as follows. Chapter 2 conveys the theoretical background on neutrino physics. It is followed by an introduction to the KATRIN experiment in chapter 3. This chapter includes also a description of the model used to describe the measured tritium β-decay spectrum and an outline on the software used within this thesis. An overview of the background processes contributing to the spectrometer background is depicted in chapter 4. This chapter is followed by chapter 5, where the carried out background characterization measurements, including the determination of the energy spectrum as well as the measurements involving the radioactive source, are described. The background properties during the first neutrino mass measurement campaign, KNM1, are summarized within chapter 6. A potential strategy to mitigate the elevated background, the **S**hifted **A**nalyzing **P**lane, is presented in chapter 7. Chapter 8 summarizes the obtained results.

2 Neutrino physics

Neutrinos are the most abundant matter particles in our universe. Their existence was first postulated by Wolfgang Pauli in 1930 to explain the continuous electron energy spectrum in beta-decay [1]. The particle is a neutral lepton with spin $\frac{1}{2}$. For a long time it was assumed to be massless, until neutrino oscillations were observed. Since the neutrino has no charge and a tiny mass, it only interacts via the weak force and to a small extent with gravity, making direct detection very challenging. As a consequence there are still many open questions related to this second-most abundant particle.

2.1 Discovery of the neutrino

The neutrino was first detected in 1956 by Clyde Cowan and Frederick Reines in the so-called Cowan-Reines experiment [2]. As direct detection method, the unique signature of inverse beta-decay was used. Electron anti-neutrinos from a nuclear reactor react with a proton to a neutron and a positron:

$$\bar{\nu}_e + p \rightarrow n + e^+ \tag{2.1}$$

The created positron will quickly annihilate with an electron, resulting in the emission of two gamma rays. To detect the neutron, a strong neutron absorber, cadmium chloride, is employed, resulting in a subsequent gamma ray. This sequence of gamma rays provides a distinct signature for this reaction and serves as direct verification of electron anti-neutrinos.

A few years later, in 1962, Leon Max Lederman, Melvin Schwartz and Jack Steinberger observed the first interaction with a neutrino of another flavor, the muon neutrino [9]. A third kind of neutrinos, tau neutrinos, were detected at Fermilab by the **D**irect **O**bservation of **Nu** **T**au (DONUT) experiment in the year 2000 [10].

Further investigations on the nature of neutrinos were carried out. From the width of the Z^0 resonance, the number of active light neutrinos was determined by four experiments at the **L**arge **E**lectron-**P**ositron (LEP) collider, to be $N = 2.984 \pm 0.008$

[11]. Measurements of the helicity, by Maurice Goldhaber, showed that the neutrino has negative helicity (left-handed) [12]. Based on these observations, three kinds of neutrinos, one for each charged lepton, were added to the **S**tandard **M**odel (SM) as massless left-handed particles. Note that the neutrinos are the only electrically neutral and solely left-handed fermions in the SM.

2.2 Neutrino oscillations

The picture of neutrinos was fundamentally changed through the observation of neutrino oscillations. First indications for such behavior were already observed in 1968 at the Homestake experiment [13], which measured the neutrino flux from the decay

$$^{8}\mathrm{B} \rightarrow {}^{8}\mathrm{Be}^{*} + \mathrm{e}^{+} + \nu_{\mathrm{e}} \tag{2.2}$$

in the Sun. Electron neutrinos were detected via the capture reaction:

$$\nu_{\mathrm{e}} + {}^{37}\mathrm{Cl} \rightarrow {}^{37}\mathrm{Ar} + \mathrm{e}^{-} \tag{2.3}$$

The observed electron neutrino flux was with $2 \cdot 10^{6}\,\mathrm{cm}^{-2}{\cdot}\mathrm{s}^{-1}$ three times lower than expected from **S**tandard **S**olar **M**odel (SSM) predictions. This discrepancy is known as the solar neutrino problem. It was resolved in 2001 by the **S**udbury **N**eutrino **O**bservatory (SNO) experiment, a water Cherenkov detector featuring 1000 t of heavy water shielded by pure water. It is sensitive not only to electron neutrinos, but also to muon and tau neutrinos by using the reactions:

$$\begin{aligned} \nu_{\mathrm{e}} + \mathrm{d} &\rightarrow \mathrm{p} + \mathrm{p} + \mathrm{e}^{-} \\ \nu_{\mathrm{x}} + \mathrm{d} &\rightarrow \mathrm{p} + \mathrm{n} + \nu_{\mathrm{x}} \\ \nu_{\mathrm{x}} + \mathrm{e}^{-} &\rightarrow \nu_{\mathrm{x}} + \mathrm{e}^{-} \end{aligned} \tag{2.4}$$

The experimental results confirmed the missing ν_{e} flux, but in terms of total neutrino flux no deficit was observed with respect to the SSM prediction. This observation can be explained by neutrino flavor oscillations, which implies a splitting of the squared neutrino mass eigenvalues [3]. Therefore not all neutrinos can be massless.

2.2.1 Theoretical description

The theoretical description of neutrino oscillations is based on the formulation by Bruno Pontecorvo. He suggested neutrino-anti-neutrino transitions in analogy to

$K^0 \rightarrow \bar{K}^0$ mixing [14]. This idea was later reformulated for neutrino flavor oscillations [15, 16]. In the simple case of only two neutrino flavors, the mixing depends only on the mixing angle θ_{12} and not on a CP-violating phase. Analogous to the Cabbibo angle in the quark sector, two flavor eigenstates ν_α and ν_β are described as superposition of two mass eigenstates ν_1 and ν_2. The relation is given by the 2×2 rotation matrix as depicted in eq. (2.5).

$$\begin{pmatrix} \nu_\alpha \\ \nu_\beta \end{pmatrix} = \begin{pmatrix} \cos\theta_{12} & \sin\theta_{12} \\ -\sin\theta_{12} & \cos\theta_{12} \end{pmatrix} \cdot \begin{pmatrix} \nu_1 \\ \nu_2 \end{pmatrix} \tag{2.5}$$

The probability of oscillation is given by eq. (2.6)

$$\begin{aligned} P(\nu_\alpha \rightarrow \nu_\beta) = P(\nu_\beta \rightarrow \nu_\alpha) &= P(\bar{\nu}_\alpha \rightarrow \bar{\nu}_\beta) = P(\bar{\nu}_\beta \rightarrow \bar{\nu}_\alpha) \\ &= \sin^2(2\theta_{12}) \cdot \sin^2\left(\frac{\Delta m^2_{12} c^3}{4\hbar}\frac{L}{E}\right) \\ &= 1 - P(\nu_\alpha \rightarrow \nu_\alpha) \end{aligned} \tag{2.6}$$

and depends on the squared mass differences $\Delta m^2_{12} = m^2_1 - m^2_2$, the mixing angle θ_{12}, the energy of the neutrino E and the distance L between neutrino source and detector (baseline). For massless neutrinos, $\Delta m_{12} = 0$, the oscillation probability is zero. Therefore the observation of flavor transitions, directly implies non-zero mass splitting $\Delta m_{12} > 0$ (and $\theta_{12} > 0$).

In case of three flavor oscillations, the additional mass splitting m^2_{23}, as well as two further mixing angles θ_{23}, θ_{31} and a CP-violating phase δ_{CP} need to be considered. The mixing of mass and flavor eigenstates is then connected via the 3×3 **P**ontecorvo-**M**aki-**N**akagawa-**S**akata (PMNS) matrix analogous to the **C**abibbo-**K**obayashi-**M**askawa (CKM) matrix in the quark sector. For details of three flavor transitions, see [17].

To access oscillation parameters experimentally, measurements with different neutrino flavors and specific $\frac{L}{E}$ ratio, adopted for best sensitivity of the desired parameter, are carried out. This is realized by using various neutrino sources. They differ in terms of neutrino flavor composition, energy and spatial distribution when produced and can be categorized as solar, atmospheric, reactor and accelerator neutrinos. For example solar and atmospheric neutrinos are best suited for the determination of θ_{12} and θ_{23}, respectively.

2.2.2 Neutrino oscillations in matter

When neutrinos propagate through matter their oscillation properties are changed. This is called **M**ikheev-**S**mirnov-**W**olfenstein (MSW)-effect according to the physicists who predicted this behavior. In matter an additional term, comprising

the interactions of neutrinos, needs to be added to the Hamiltonian resulting in eq. (2.7).

$$H = H_0 + H_{\text{int}} \tag{2.7}$$

Here H_0 denotes the system in vacuum and H_{int} the interaction term. For solar neutrinos only coherent elastic scattering needs to be considered, other mechanism have negligible impact [18]. H_{int} can be described in terms of a potential difference U, given in eq. (2.8), with G_F as the Fermi coupling constant. It is determined by charged current scatterings of ν_e on electrons, such that it only depends on the electron density in matter n_e. Neutral current interactions would affect all neutrino types in equal measure, leading to no change in the oscillation pattern.

$$U = \sqrt{2} G_F n_e \tag{2.8}$$

The modified Hamiltonian leads to a change of eigenvalues and eigenstates. In the simple two flavor scenario this leads to

$$\begin{pmatrix} \nu_\alpha \\ \nu_\beta \end{pmatrix} = \begin{pmatrix} \cos\theta_m & \sin\theta_m \\ -\sin\theta_m & \cos\theta_m \end{pmatrix} \cdot \begin{pmatrix} \nu_{1m} \\ \nu_{2m} \end{pmatrix} \tag{2.9}$$

with the matter mixing angle θ_m, depending on the neutrino energy and the matter electron density as given in eq. (2.10) [19].

$$\sin^2(2\theta_m) = \frac{\sin^2(2\theta)}{\left[-\frac{U \cdot E}{\Delta m^2} - \sin^2(2\theta)\right]^2 + \sin^2(2\theta)} \tag{2.10}$$

This leads to matter density dependent oscillation properties and effects like resonantly enhanced oscillations [20]. Their observation confirmed the existence of the MSW-effect. The oscillation property is defined analogous to eq. (2.6) just with matter modified mixing angles and mass eigenstates. Since eq. (2.10) is sensitive to the sign of Δm^2, matter effects can be used to determine the sign of a mass splitting. This way Δm^2_{12} can be determined from solar neutrino experiments, like Super-Kamiokande that measured $\Delta m^2_{12} = (4.8^{+1.5}_{-0.8} \cdot 10^{-5})\ \text{eV}^2$ [21].

2.3 Neutrino mass determination

Via neutrino oscillations the differences between the neutrino mass squares can be determined as well as the minimal sum of neutrino masses ($\sum_i m_i > 0.06\,\text{eV}$ (0.1 eV) for normal and (inverted) hierarchy [22]). However their absolute values and the resulting hierarchy (normal: $m_1 < m_2 < m_3$, inverted: $m_3 < m_1 < m_2$, degenerate: $m_1 \approx m_2 \approx m_3$) can not be accessed. Hence experiments other than those based on neutrino oscillations are required to determine the absolute neutrino mass. In the following most commonly used methods are summarized shortly.

2.3.1 Cosmology

The evolution of our universe since the Big Bang is described within the ΛCDM model (cosmological constant Λ, **c**old **d**ark **m**atter (CDM)). With its six parameters, amongst others the Hubble constant H_0, a baryonic matter fraction Ω_b and a matter fraction Ω_m, good consistency with experimental results is achieved. Based on the ΛCDM model, cosmology is sensitive to the density of neutrinos, the number of active left-handed flavors and their summed masses $M = \sum_i m_i$.

Neutrinos affect the formation of structure in the early universe. With velocities close to c, they free-stream over large distances. Density fluctuations below that distance are washed out, preventing the growth of smaller scale structures. The neutrino mass affects the free-streaming length, hence up to which scale fluctuations are flattened out, as well as the contribution of neutrinos to the overall matter density [23].

Strongest constraints on the summed neutrino masses are provided by the Planck satellite, that investigated anisotropies of the **c**osmic **m**icrowave **b**ackground (CMB) [24]. With $M < 0.12\,\text{eV}$ at 95 % C.L., the measurement provided currently the most stringent limits on the neutrino mass from cosmology.

2.3.2 Neutrinoless double β-decay

Besides cosmology, neutrinoless double β-decay offers the potential to push neutrino mass limits down to $\mathcal{O}(\text{meV})$. The decay is illustrated in fig. 2.1. In case of Majorana neutrino nature the electron (anti-)neutrino is emitted and absorbed by the other vertex, such that only two electrons are emitted. Hence this process also probes the Dirac or Majorana nature of neutrinos.

If the decay is mediated by a light neutrino, its rate is given by

$$\frac{1}{T_{1/2}} = G|M|^2|m_{\beta\beta}|^2 \tag{2.11}$$

and depends on the phase space factor G, the nuclear matrix element M and the effective Majorana mass $m_{\beta\beta}$. The Majorana mass is defined as the coherent sum

$$|m_{\beta\beta}| = \left|\sum U_{ei}^2 m_i\right| \tag{2.12}$$

of the neutrino mass eigenstates m_i with the PMNS-matrix U_{ei}. In principle U_{ei}^2 contains also complex CP-phases enabling cancellations.

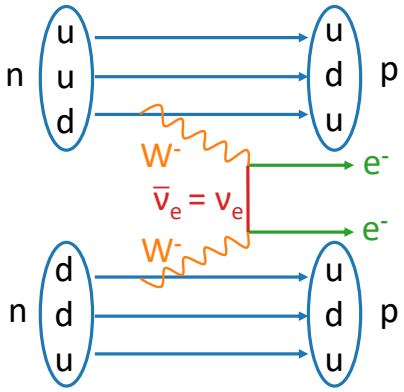

Figure 2.1: Scheme of neutrinoless double β-decay. In case of Majorana nature, the emitted neutrino is absorbed by the other vertex, such that only two electrons are emitted.

From the measured half-life of the decay, the effective Majorana mass can be extracted based on eq. (2.11). This equation also reveals the model dependencies of this method, namely precise knowledge of the nuclear matrix elements, which remains challenging [25]. One promising ^{76}Ge based experimental approach is the **Ger**manium **D**etector **A**rray (GERDA) experiment. Its current limit is $T_{1/2} > 0.9 \cdot 10^{26}$ yr at 90 % C.L. based on an exposure of 82.4 kg·yr providing an upper limit on the effective Majorana mass $m_{\beta\beta} < 104$ to 224 meV depending on the nuclear matrix elements [26].

2.3.3 Kinematics

Experiments based on kinematics do not depend on the neutrino's nature. Therefore those approaches are referred to as 'model-independent'. Such experiments are based either on electron capture or β-decay. The observable is in both cases the incoherent sum of the neutrino masses:

$$m_\nu^2 = \sum_i |U_{ei}|^2 m_i^2 \tag{2.13}$$

In the SM this quantity is the same for electron capture and β-decay, regardless of whether an electron neutrino or electron anti-neutrino is emitted.

Electron capture

In case of electron capture the most promising isotope is ^{163}Ho. After electron capture, the created electron neutrino escapes and ^{163}Dy is left in an excited state, de-exciting via Coster-Kronig transistions and under emission of X-rays and Auger electrons.

$$\begin{aligned} {}^{163}_{67}\mathrm{Ho} &\rightarrow {}^{163}_{67}\mathrm{Dy}^{*} + \nu_{\mathrm{e}} \\ {}^{163}_{67}\mathrm{Dy}^{*} &\rightarrow {}^{163}_{66}\ \mathrm{Dy} + E_{\mathrm{C}} \end{aligned} \tag{2.14}$$

The decay energy is carried by the electron neutrino and the de-excitation energy E_C

$$E_C \propto \sqrt{1 - \frac{m_\nu^2}{(Q_{\mathrm{EC}} - E_{\mathrm{C}})^2}} \tag{2.15}$$

with the decay energy Q_{EC}. Thus by a precise measurement of E_{C}, information on the electron neutrino mass can be obtained. The current best limit on the electron neutrino mass based on this technique is $m_\nu < 150\,\mathrm{meV}$ at 90 % C.L. [27] and was determined by the **E**lectron **C**apture in **Ho**lmium (ECHo) experiment [28].

Tritium β-decay

When using β-decay for determining the neutrino mass, tritium is usually the isotope of choice. Its super-allowed decay results not only in the short half-life of $T_{1/2} = 12.3\,\mathrm{yr}$, but also in an easy computable nuclear matrix element. In addition tritium has a low endpoint energy of $E_0 = 18.6\,\mathrm{keV}$, increasing the statistics close to the endpoint E_0 of the tritium β-decay electron energy spectrum. In the decay

$${}^{3}\mathrm{H} \rightarrow {}^{3}\ \mathrm{He} + \mathrm{e}^{-} + \bar{\nu}_{\mathrm{e}} \tag{2.16}$$

an electron and an electron anti-neutrino is emitted. In case of zero neutrino mass, the electron carries the complete decay energy. For non-zero masses the maximal energy of the electron E_0 is reduced by the neutrino mass, leading to a reduced maximal electron energy. This behavior is reflected in the differential electron energy spectrum, based on the Fermi theory, which is given by

$$\frac{\mathrm{d}\Gamma}{\mathrm{d}E}(E) = C \cdot F(Z,E) \cdot p \cdot (E + m_e) \cdot (E - E_0) \cdot \sqrt{(E - E_0)^2 - m_\nu^2}\ \Theta(E_0 - E - m_\nu) \tag{2.17}$$

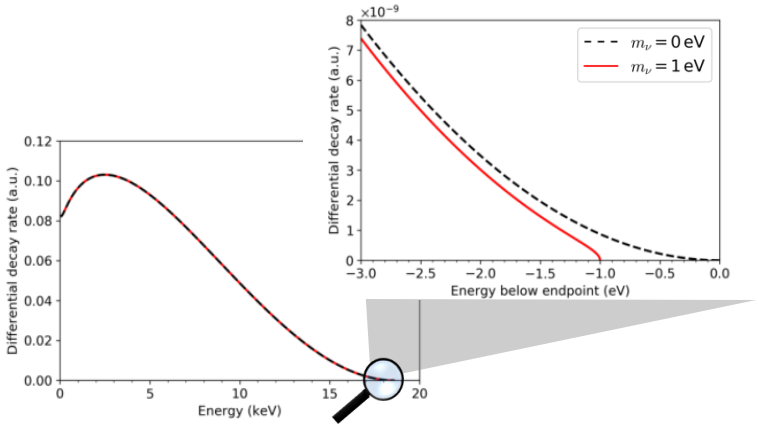

Figure 2.2: Differential electron β-decay spectrum and zoom into the region close to the endpoint. The red line shows the imprint of a non-zero mass of $m_\nu = 1\,\mathrm{eV}$.

with the electron energy E and momentum p. The term $F(Z,E)$ is the Fermi function taking into account the interaction of the emitted electron with the daughter nucleus. The constant C is defined as

$$C = \frac{G_F^2 \cdot \cos^2\theta_\mathrm{c}}{2\pi^3} \cdot |M|^2 \tag{2.18}$$

where G_F denotes the Fermi constant, θ_c the Cabbibo angle and M the nuclear matrix element. Figure 2.2 shows the imprint of the neutrino mass on the β-electron energy spectrum with a close view on the region close to the endpoint.

A precise measurement of the electron energy spectrum shape around the endpoint thus contains information on m_ν^2. Based on this concept the current best model-independent upper limit on the electron anti-neutrino mass was obtained by the **Ka**rlsruhe **Tri**tium **N**eutrino (KATRIN) experiment with $m_\nu < 1.1\,\mathrm{eV}$ at 90 % C.L. [29].

3 The KATRIN Experiment

The **Ka**rlsruhe **Tri**tium **N**eutrino (KATRIN) experiment is designed to determine the effective electron anti-neutrino mass in a model-independent way, by investigating the tritium β-decay electron energy spectrum close to the endpoint. After three years of measurement time it aims for a sensitivity of 0.2 eV[1] at 90 % C.L. [4]. It is located at the **K**arlsruhe **I**nstitute of **T**echnology (KIT) and partially hosted by the **T**ritium **L**aboratory **K**arlsruhe (TLK). In the following chapter the setup of this experiment is introduced (section 3.1) as well as the modeling of the measured tritium β-decay spectrum (section 3.2). Further the software packages used for simulation and analysis within this thesis are presented in section 3.3. The chapter is completed with section 3.4, which outlines the relevance of the background for the experiment's performance.

3.1 Experimental setup and measurement principle

The KATRIN experiment is the successor of the Mainz and Troitsk experiments. Those experiments achieved the best model-independent upper limits on the electron anti-neutrino mass with $m_\nu < 2.3\,\text{eV}$ at 95 % C.L. [7] (Mainz) and $m_\nu < 2.05\,\text{eV}$ at 95 % C.L. [8] (Troitsk), prior to KATRIN. The successor was built with the goal to improve the sensitivity by one order of magnitude down to $m_\nu < 0.2\,\text{eV}$ at 90 % C.L..

A scheme of the 70 m long experiment is shown in fig. 3.1. Tritium is injected into the **w**indowless **g**aseous **t**ritium **s**ource (WGTS) (b). Created electrons are guided by magnetic field lines through the transport section (c) into the spectrometer section (d) and (e), where their energy is analyzed using **m**agnetic **a**diabatic **c**ollimation combined with an **e**lectrostatic filter (MAC-E). Passing electrons are detected by the **f**ocal **p**lane **d**etector (FPD). The back side of the experiment is closed by the so-called rear section. In the following, those five individual sections and their functionality are explicated, mainly based on the **T**echnical **D**esign **R**eport (TDR) [4] and [30].

[1] For better readability natural units are used within this work such that the reduced Planck constant $\hbar = 1$ and the speed of light $c = 1$

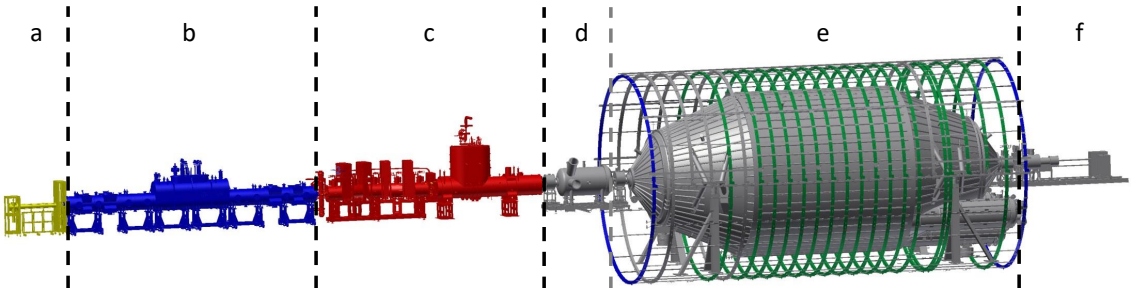

Figure 3.1: Scheme of the KATRIN experiment: a) rear section, b) **w**indowless **g**aseous **t**ritium **s**ource, c) transport section, d) **p**re-**s**pectrometer, e) **m**ain **s**pectrometer, f) **f**ocal **p**lane **d**etector.

Rear section

The rear section is located at the end of the 70 m long beam line, shown in figure fig. 3.1. It consists of the rear wall, a gold plated stainless steel plate, and diagnostic tools. An important tool is the electron gun [31], a mono-energetic, angular selective electron source. It is used to determine important tritium source properties, like the gas density and to investigate electron transmission properties through the whole setup. Another electron source in the rear section is an ultraviolet illumination of the rear wall. It can be used to counteract positive charges building up in the tritium source. Electrons created in the rear section are guided towards the WGTS by a superconducting magnet. The rear section further hosts a β-**I**nduced **X**-ray **S**pectroscopy (BIXS) system [32], consisting of two detectors, that measures the X-ray spectrum from β-electrons hitting the rear wall. This system is one of the tools monitoring the source activity.

Windowless gaseous tritium source

The WGTS [33] is a ultra-luminous and stable tritium source with an activity of 10^{11} Bq. It is hosted in a 10 m long cryostat with a diameter of $d = 90$ mm. Gaseous tritium with a purity larger than 95 % is continuously injected into the cryostat's center and pumped out on both sides to ensure stable conditions. The source incorporates an integrated gas density of $\rho d = 5 \cdot 10^{17}\,\mathrm{cm}^{-2}$, which corresponds to $N = 2 \cdot A \cdot \rho d$ tritium atoms (purity neglected). Here A denotes the source area and the factor two considers the two tritium atoms per molecule. A **la**ser **Ra**man (LARA) system [34, 35] monitors the current source composition. To maintain the high column density, the WGTS is cooled to a temperature of 30 K. Superconducting magnets, inducing a magnetic flux of $\Phi = 191\,\mathrm{T{\cdot}cm}^2$, guide created β-electrons towards the transport or rear section. For calibration purposes, the isotope $^{83\mathrm{m}}$Kr can be injected

into the WGTS [36]. In this operation mode the source temperature is raised to 90 K to prevent freezing of krypton.

Transport section

KATRIN employs a windowless gaseous tritium source. Therefore tritium needs to be prevented from entering the **s**pectrometer and **d**etector **s**ystem (SDS), where it would be a source of background. Sufficient tritium flow reduction is achieved in the transport section, which hosts the **d**ifferential **p**umping **s**ection (DPS) [37] and the **c**ryogenic **p**umping **s**ection (CPS) [38]. Both sections are arranged in chicanes to avoid a direct line of sight for tritium molecules. The β-electrons are magnetically guided through this arrangement towards the spectrometer section. In the DPS tritium is pumped out by multiple **t**urbo **m**olecular **p**umps (TMPs). Tritium ions are blocked by ring electrodes and additional dipole electrodes drift ions out of the flux tube. The subsequently installed CPS acts as a cold trap. Its inner surface is covered by an argon frost layer, trapping tritium molecules. Both, DPS and CPS, together reduce the neutral tritium flow by more than 14 orders of magnitude.

Spectrometer section

The spectrometer section is a tandem arrangement of two spectrometers, the **p**re-**s**pectrometer (PS) and the **m**ain **s**pectrometer (MS). Both filter the β-electrons according to their energy using **m**agnetic **a**diabatic **c**ollimation combined with an **e**lectrostatic filter (MAC-E), which was first proposed by Kruit in 1983 [40]. It is the same principle employed in the predecessor experiments Mainz and Troitsk. The working principle is illustrated in fig. 3.2. Electrons are guided by magnetic field lines, defined by two superconducting solenoids at the entrance and exit and the air coils, through the spectrometer. High voltage applied on the spectrometer vessel defines the filter potential U, also called retarding potential, related to the retarding energy qU through the electron charge $q < 0$. Consequently only electrons with longitudinal energies larger than the applied potential can pass the spectrometer and are counted by the detector. Through variation of the filter potential an integrated spectrum is acquired. However such a filtering is only precise for small transversal energies, such that

$$E_{\text{kin}} = E_{\parallel} + E_{\perp} \approx E_{\parallel}. \tag{3.1}$$

The residual transversal energy defines the energy resolution of such a filtering. In KATRIN electrons are generated isotropically in the WGTS thus collimation of

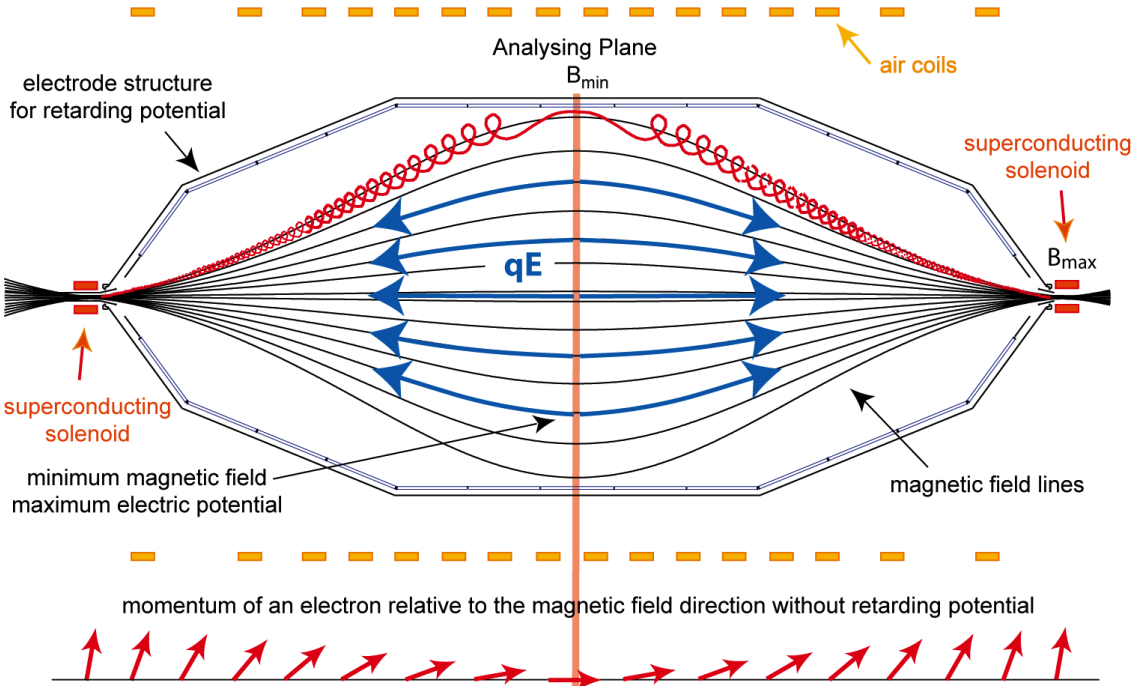

Figure 3.2: Principle of **m**agnetic **a**diabatic **c**ollimation combined with an **e**lectrostatic filter (MAC-E) applied in the KATRIN spectrometers. Figure adapted from [39]

energy is essential for good energy resolution. Given adiabatic electron transport, the magnetic moment of the electrons is conserved and in the non-relativistic limit given by

$$\mu = \frac{E_\perp}{B}. \tag{3.2}$$

Hence the transversal energy is dependent on the local magnetic field with $E_\perp = \mu \cdot B$. Therefore collimation can be achieved by a reduction of magnetic field. For precise filtering the electrons experience the maximal retarding potential at minimal magnetic field B_{min}, where their energy is most collimated. Here, in the so-called analyzing plane, the electrons energy is analyzed. The energy resolution follows from conservation of magnetic moment and is given by

$$\frac{\Delta E}{E} = \frac{B_{\text{min}}}{B_{\text{max}}}. \tag{3.3}$$

The KATRIN MS is designed for a maximal magnetic field of $B_{\text{max}} = 6\,\text{T}$ and an analyzing plane field of $B_{\text{min}} = 3 \cdot 10^{-4}\,\text{T}$. In this configuration[2] the energy resolution is $\Delta E = 0.93\,\text{eV}$ at the tritium endpoint $E_0 = 18.6\,\text{keV}$. Such tremendous reduction of

[2]This configuration is currently not used due to the elevated background rate.

magnetic field in the MS results in a very wide flux tube in the analyzing plane giving reason for the large diameter of the KATRIN MS of 10 m. The angular acceptance of KATRIN follows also magnetic moment conservation and is

$$\theta_{\text{max}} = \arcsin\left(\sqrt{\frac{B_{\text{Source}}}{B_{\text{max}}}}\right) \approx 51^{\circ}. \tag{3.4}$$

Here B_{Source} denotes the magnetic field where the electron is created, which is in KATRIN usually the WGTS, with $B_{\text{Source}} = 3.6\,\text{T}$. Electrons with polar angles larger than θ_{max} will be reflected by the high magnetic field of the pinch magnet with $B_{\text{max}} = B_{\text{Pinch}} = 6\,\text{T}$, located at the exit of the MS. The low magnetic field over the 20 m long MS is precisely shaped by the **l**ow **f**ield **c**orrection **s**ystem (LFCS), an air-coil system, around the MS shown green in fig. 3.1. Additional coils compensate the earth magnetic field, the so-called **E**arth **M**agnetic field **C**ompensation **S**ystem (EMCS).

The retarding potential is shaped by an **I**nner **E**lectrode (IE) system covering the whole inner surface. A scheme of this system is shown in fig. 3.3. Viewing on the MS from above, it is divided into two dipole halves, the east and west dipole. To each a separate voltage can be applied. Additionally individual voltages can be set on the rings 2 to 16 as well as to the two **A**nti-**P**enning **E**lectrodes (APEs). The last mentioned were installed to prevent the formation of a Penning trap, a source of background, close to the electrodes. With this system the high voltage can be fine-tuned for optimal electron transmission and filter characteristics. Usually a radial symmetric potential is applied with equal voltages on the east and west dipole. For good transmission properties the two steep cones (downstream and upstream side) are slightly more positive with respect to the other IEs. Note that ring 5 and 6 on the east part were short-circuited by the bake-out[3]. Stability of the electrostatic filter potential is of highest importance for precise energy filtering. Therefore the high voltage is monitored by a precision voltage divider on the parts per million level [41]. To suppress fluctuations caused by remaining AC components of the power supplies a so-called **p**ost **r**egulation (PR) system is installed. It was commissioned at the end of the year 2017. Detailed information on the high voltage performance can be found in [42].

As mentioned above, two spectrometers are installed in KATRIN. In the PS low energetic electrons are rejected to reduce the flux of β-electrons into the MS to prevent background creation. Ring electrodes at both PS sides serve as last ion blocking step. The subsequent MS precisely analyzes the energy of the transmitted high energy electrons. To reduce background due to scattering on residual gas both spectrometers are evacuated to a pressure of 10^{-11} mbar.

[3] complete spectrometer is heated up to 350 °C to improve vacuum conditions

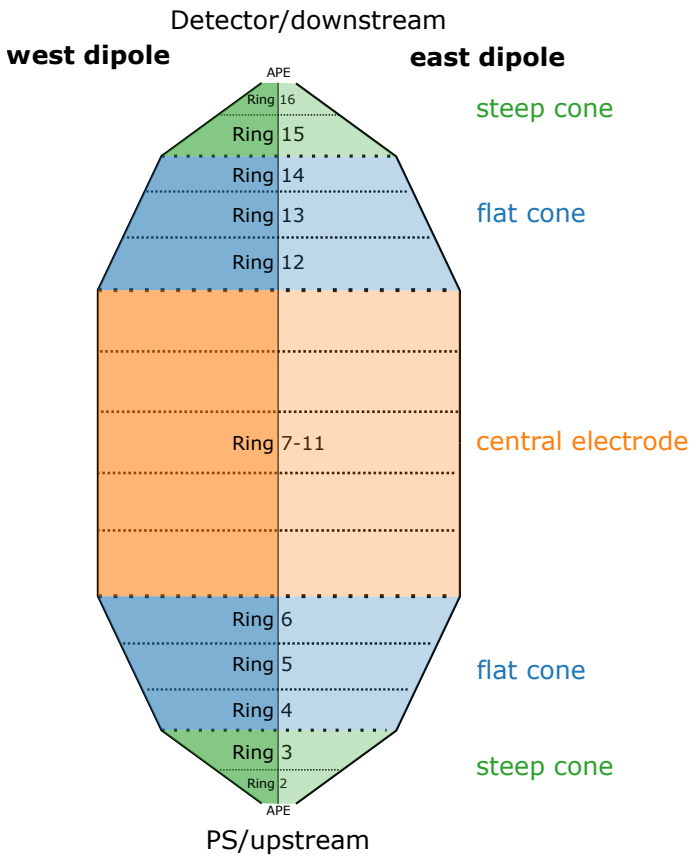

Figure 3.3: Scheme of the IE partition in the MS, viewing from above. Each of the 15 rings can be supplied by an individual voltage. The rings 2 to 3 and 15 to 16 form the so-called upstream and downstream steep cones, rings 4 to 6 and 12 to 14 build the respective flat cones and rings 7 to 11 belong to the central electrode. In addition the whole system can be split in east and west allowing separate voltage supply. Two APEs prevent formation of a Penning trap, see section 4.2.4.

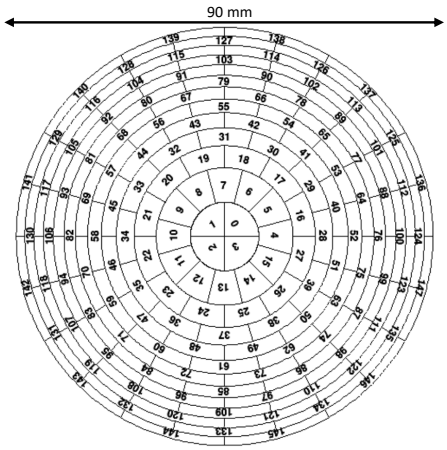

Figure 3.4: Pixel arrangement of the **f**ocal **p**lane **d**etector (FPD).

Focal plane detector

The **f**ocal **p**lane **d**etector (FPD) is located at the exit of the MS and counts all electrons passing the MAC-E-filters. It is a silicon p-i-n diode array of 148 pixels, divided in 12 rings with 12 pixels each and the bulls-eye with 4 pixels, on a single wafer. The pixels are arranged as shown in fig. 3.4 with each pixel having the same size of $44\,\mathrm{mm}^2$ [43]. Such segmentation reduces uncertainties arising from magnetic field and retarding potential variations. The detector is located in the same magnetic field as the WGTS such that the magnetic flux tube is fully mapped. Before hitting the FPD, electrons are post-accelerated with typically $U_{\mathrm{PAE}} = 10\,\mathrm{kV}$ to reduce backscattering and intrinsic detector background in the region of interest. The energy resolution of this detector is with about 2 keV (**f**ull **w**idth at **h**alf **m**aximum (FWHM)) [44] rather poor, but since the resolution of the KATRIN experiment is given by the MAC-E filter this satisfies requirements.

3.2 Model of the integrated tritium β-decay spectrum

KATRIN measures an integrated tritium β-decay spectrum emitted from a molecular tritium source. The basic modeling of this spectrum is described in the following based on [45, 46, 47]. For a precise description of the measured spectrum further physics needs to be considered (e.g. Synchrotron radiation, Doppler effect, detailed source model), which are not discussed here. Employment of a molecular tritium source causes modifications to the theoretical differential spectrum, eq. (2.17), which are introduced in section 3.2.1. The integrated spectrum acquired by the MAC-E

filter is given by

$$I(qU) = N \cdot \int_{qU}^{E_0} \frac{\mathrm{d}\Gamma}{\mathrm{d}E}(E) \cdot R(qU,E)\,\mathrm{d}E + B \tag{3.5}$$

with the constant factor

$$N = N_{\mathrm{eff}} \cdot \frac{1 - \cos\theta_{\mathrm{max}}}{2} \cdot \epsilon_{\mathrm{detector}}. \tag{3.6}$$

Here qU denotes the retarding potential, $\frac{\mathrm{d}\Gamma}{\mathrm{d}E}(E)$ the differential spectrum, $R(qU,E)$ the response function described in section 3.2.2, E_0 the endpoint of the tritium β-decay spectrum and B the background. The factor N depends on the number of tritium atoms in the source N_{eff}, the accepted solid angle $(1 - \cos\theta_{\mathrm{max}})/2$ and the detection efficiency $\epsilon_{\mathrm{detector}}$.

3.2.1 Final state distribution

After the β-decay of T_2 the energy is shared between electron, electron anti-neutrino and excitations of the daughter molecule. The molecule can be left in a rotational or vibrational excitation of the ground state or in a electronically excited state. This reduces the available energy for electron and neutrino leading to a shift of the maximal electron energy E_0. For precise neutrino mass determination accurate knowledge of the energy attributed to excitations is required. The probabilities of the different excitation energies are described within the **f**inal **s**tate **d**istribution (FSD). In KATRIN, tritium occurs in form of three isotopes T_2, HT and DT. For each the respective FSD needs to be considered. An example of such a distribution for HT as calculated within [48] is shown in fig. 3.5. The lower energetic part corresponds to excitations of the ground state and the higher energetic contributions to electronic excitations. By summing over the individual contributions based on the concentrations in the WGTS the resulting differential spectrum is calculated. The source constituents are precisely determined by the LARA system.

3.2.2 Response function

The response function gives the probability of an electron with energy E to be transmitted through the experimental apparatus. This probability depends predominantly on the transmission properties of the MAC-E filter and on the energy loss of electrons within the tritium source through scattering. The transmission probability $T(qU, E)$

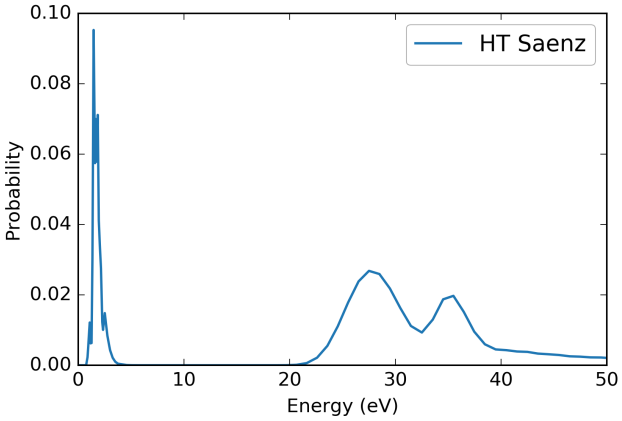

Figure 3.5: Final state distribution of the tritium isotope HT calculated by Saenz et al. [48]. The peak below 10 eV is attributed to rovibrational excitations of the ground state. Higher energetic contribution are from electronic excitations.

of the MAC-E filter is given by

$$T(qU,E) = \begin{cases} 0 & E < qU \\ \dfrac{1-\sqrt{1-f\cdot\frac{B_{\text{Source}}}{B_{\text{min}}}\cdot\frac{E-qU}{E}}}{1-\sqrt{1-\frac{B_{\text{Source}}}{B_{\text{max}}}}} & qU \leq E \leq qU\cdot\frac{f\cdot B_{\text{max}}}{f\cdot B_{\text{max}}-B_{\text{min}}} \\ 1 & E > qU\cdot\frac{f\cdot B_{\text{max}}}{f\cdot B_{\text{max}}-B_{\text{min}}} \end{cases} \tag{3.7}$$

with the relativistic factor f:

$$f = \frac{\frac{E-qU}{m_e}+2}{\frac{E}{m_e}+2}. \tag{3.8}$$

For the experiment's configuration used in the first neutrino mass measurement [29], the transmission function is shown in fig. 3.6(a). Depending on the electron's starting angle a certain amount of surplus energy $E-qU$ is required to pass the MAC-E-filter. For electrons with surplus energies larger than the energy resolution, all are transmitted up to the acceptance angle (see eq. (3.4)). Integrating over all accepted angles results in the shown shape valid for an isotropic source.

The second contribution to the response function are scatterings in the tritium source. Due to the high column density in the WGTS there is a non-negligible probability for inelastic scattering within the source section. Elastic scattering can be neglected because of the 12 times lower cross section [4]. The probability of an electron with the emission angle θ to scatter i times is given by

$$P_i = \frac{1}{1-\cos\theta_{\text{max}}}\int_0^{\theta_{\text{max}}}\sin\theta\int_0^1 P_{\text{inel,i}}(y,\theta)\,\mathrm{d}z\,\mathrm{d}\theta \tag{3.9}$$

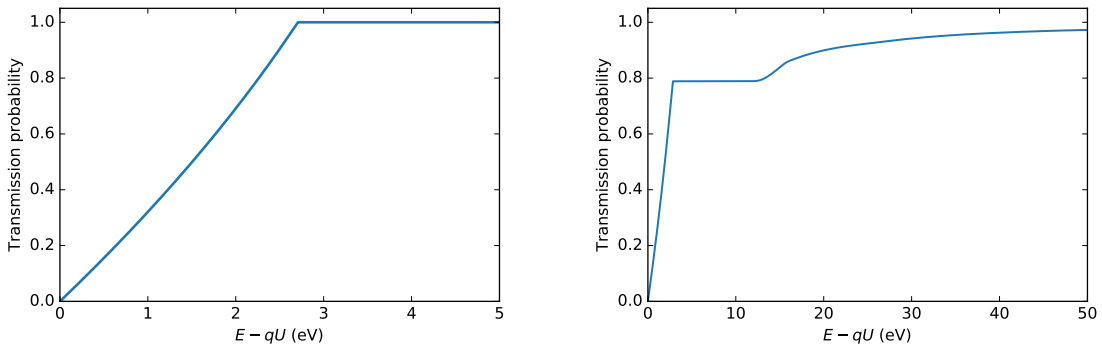

(a) Transmission function (b) Response function

Figure 3.6: Transmission function of the MAC-E filter (a) and the corresponding response function (b) at a retarding potential of −18.6 kV in the configuration used in the first neutrino mass measurement (KNM1). Response function kindly provided by Martin Slezák.

with the inelastic scattering probability

$$P_{\text{inel,i}}(z,\theta) = \frac{(\lambda(z,\theta)\cdot\sigma_{\text{inel}})^i}{i!}\cdot e^{-\lambda(z,\theta)\cdot\sigma_{\text{inel}}} \qquad \text{with} \qquad \lambda(z,\theta) = \frac{z\cdot\rho d}{\cos\theta}. \tag{3.10}$$

The energy dependent cross section is given in [49] to be

$$\sigma_{\text{inel}}(E) = \frac{4\pi a_0^2}{E/E_{\text{Ryd}}}\left[1.5487\ln\left(\frac{\beta^2}{1-\beta^2}\right) + 17.4615\right] \tag{3.11}$$

where E_{Ryd} denotes the Rydberg energy, a_0 the Bohr radius and $\beta = \frac{v}{c}$ with the velocity v and the speed of light c.

Each scattering processes is associated with a loss of energy. The probability to loose the energy ϵ in one inelastic scattering process is given by the energy loss function $f(\epsilon)$. In KATRIN the characteristics of single and multiple inelastic scattering are measured with the mono-energetic electron gun [29]. The measured energy loss function is parametrized by three Gaussian distributions, that describe the excitation spectrum, and an ionization tail.

The complete response function, see fig. 3.6(b), is then given by

$$R(qU,E) = \int_0^{E-qU} T(qU, E-\epsilon)\sum_{i=0}^{\infty} P_i\cdot f_i(\epsilon)\,\mathrm{d}\epsilon \tag{3.12}$$

3.3 Software packages

KATRIN is a large and complex experiment. To monitor the relevant parameters more than 10 000 sensors are installed. They are essential for stable and controlled operation, which requires for instance continuous source conditions, constant magnetic fields, temperatures and pressures along the whole setup. For studying the electron's motion in such environment a detailed simulation software is required. Extensive understanding of transmission conditions as well as the impact of source properties are of high importance not only for the design of the experiment but also for modeling of the measured β-decay spectrum. For the KATRIN experiment the KATRIN Analysis and Simulations Package (KASPER) was developed which comprises software for data access, data analysis including fitting procedures, field calculation and a particle tracking software. The most important features in terms of this thesis, are summarized in section 3.3.1. In addition to this software package, an independent tool for spectrum modeling and fitting, Fitrium, was developed [46] which is described in section 3.3.2.

3.3.1 KATRIN Analysis and Simulations Package

KASPER is a collection of various software tools, written in C++ by the KATRIN Collaboration. It contains e.g. software for data readout of specific sensors, source simulation and full particle tracking **M**onte **C**arlo (MC). Detailed information on the individual components can be found in multiple theses [39, 50, 51, 52]. Here only a short summary on Beans and Kassiopeia will be given which are most relevant for this work. An overview of all KASPER tools can be found in appendix A.1.

Beans

Beans is a C++ toolkit developed at the University of Washington [53]. It offers various predefined analysis functions that can be easily combined in a configuration file for user specified applications without good knowledge of C++. Through its flexible and easy usability, it is a valuable tool for near online analysis not only of FPD data, but also for slow control parameters like high voltage, pressure, etc. The tool includes functions to access raw data directly from the **K**ATRIN **d**ata **b**ase (KDB) and for applying the correct calibrations. For further analysis user specified analysis cuts, like **r**egion **o**f **i**nterest (ROI), pixel selection, etc. can be applied. As output images as well as `.root` [54] files are provided. An event by event readout of FPD data is also available providing a simple text file with event

timestamp, pixel number and energy. Beans is also used to create the so-called **r**un **s**ummaries (RS). Those are text files, built up in tree format, that include relevant data necessary for tritium spectrum analysis. To be easily accessible they are stored on the IDLE. Data analyzed within this thesis is either read out directly with Beans by specific scripts or based on RS.

Kassiopeia

Kassiopeia is a particle tracking software developed for the KATRIN experiment [55]. It offers electromagnetic field calculation together with particle navigation through complex geometries and fields. A tracking of particles through the complete experimental setup requires a precise and fast calculation of electric and magnetic fields. For this task KEMfield was developed, which uses the **B**oundary **E**lement **M**ethod (BEM) and the Robin Hood algorithm [56] for efficient and accurate computation. More information on the field calculation can be found in [51]. For a flexible and easy use, also by non expert programmers, simulations are configured with E**x**tensible **M**arkup **L**anguage (XML) files. In these files geometry, physical processes (e.g. particle generation and termination, interactions) and output parameters are specified. Geometries, of any kind, can be defined with XML files using KGeoBag. In general Kassiopeia simulations, and correspondingly the output files, are organized in steps, events, tracks and runs. A step is the smallest unit, describing the motion of a particle, through solving the equations of motions, in a predefined geometry. The complete trajectory from generation to termination is called track, which is essentially a collection of consecutive steps. All tracks that origin from a single particle belong to one event. A common case is a primary particle generating secondary particles through interaction processes. The largest entity is a run. It consists of a user specified number of events.

According to this structure the algorithm for a simulation of one run is shown in fig. 3.7. The start of a simulation initiates the run, where events, tracks and steps are started accordingly. An event begins with the generation of a particle with user defined kind, energy and starting position. Afterwards track and navigation are initialized. A sequence of steps follows, based on the specified electric and magnetic fields, propagation, geometry and interactions until the particle is terminated. If more than one event is simulated, the next event is created.

For the propagation of a particle two kinds are differentiated, exact and adiabatic trajectories. In case of an exact trajectory the particle is described, by the position vector $\mathbf{r}$ and momentum vector $\mathbf{p}$, as a function of time t. For a particle with charge q in an electric field $\mathbf{E}$ and magnetic field $\mathbf{B}$ the equation of motion is given by the Lorentz equation. If the particle's motion can be approximated as adiabatic, in case

that magnetic and electric fields are nearly constant within one cyclotron radius, the state as a function of time can be given with the guiding center of motion $\mathbf{r}_c$, the momentum $p_\perp$ and $p_\parallel$ and the gyration phase ϕ. Since the particles trajectory is calculated along the position of the guiding center instead of the complete cyclotron turns a much larger step size is possible. This speeds up the computation. The exact trajectory of the particle can be reconstructed after each step. In addition so-called magnetic trajectories are available. Here the particle is represented only with the position $\mathbf{r}$ for the different times. This trajectory is frequently used to illustrate magnetic field lines. Based on those field lines for example the magnetic flux volume mapped onto the detector can be calculated. In case of very small cyclotron radii such trajectory can also be a good approximation computable with low effort. A track is ended if one fo the termination criteria are met. A selection of available options for termination are

- **Trapped**: Based on user defined number of particle turns.
- **Maximal x/y/z**: Exceeding of a specific coordinate, e.g. leaving the spectrometer.
- **Maximal radius r**: Exceeding of a radius, for example if its too large to fit into in the setup.
- **FPD**: Hitting of the detector.
- **Surface**: Hitting of a specific surface of the geometry like an electrode or the spectrometer vessel.
- **Minimal energy**: Particle's energy falling below a specified energy.

3.3.2 Fitrium

Fitrium (Fit Tritium) is a modeling and fitting tool developed for KATRIN by Christian Karl and Martin Slezák [46]. It is written in C++ and based on the Fitness Studio, an interface for fitting models to data. The software includes a model for tritium β-decay, as described in section 3.2, ^{83m}Kr conversion electrons [57] and the electron gun [58]. It further contains relevant features of the KATRIN apparatus and command line tools for fitting and MC data generation. Fitrium is configured with a configuration file (`.ini`), where the fit parameters with their initial values, model specifications, etc. are set. In- and output files are in HDF5 format [59].

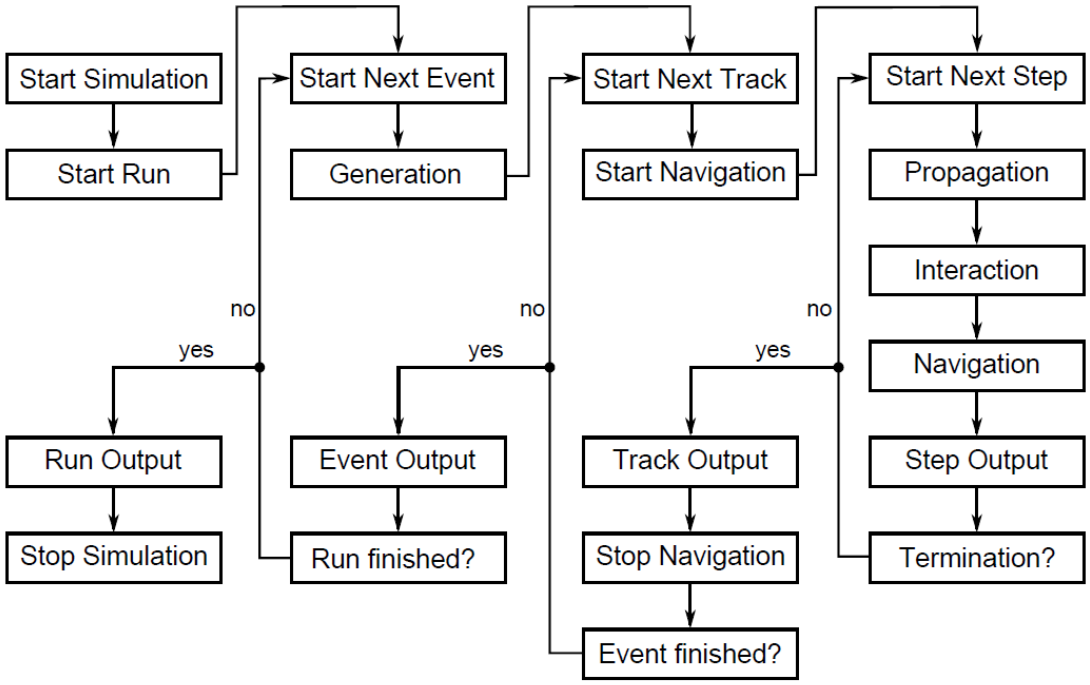

Figure 3.7: Schematic view of a Kassiopeia simulation of one run, organized in steps, tracks and events. Figure from [50].

For fitting of a model to data (measured or MC) the maximum likelihood estimation is used, where the likelihood function is defined as

$$\mathcal{L} = \mathcal{L}(\theta, \mu|x). \tag{3.13}$$

It gives the probability of a model μ with the parameters θ to describe the data x. Through variation of θ the likelihood is maximized. For numerical reasons it is more efficient to minimize $-\ln \mathcal{L}$ instead of $\mathcal{L}$. In the limit of Gaussian statistics, meaning high number of counts N, this is equivalent to a χ^2 minimization

$$-\ln \mathcal{L}(\mu|x) = -\frac{1}{2}\chi^2(\mu|x). \tag{3.14}$$

with

$$\chi^2(\mu|x) = \sum_{i=0}^{n-1} \frac{(x_i - \mu_i)^2}{\sigma_i^2} \tag{3.15}$$

where n is the number of data points and σ_i their uncertainty.

With respect to systematic effects, three methods are implemented in Fitrium. One option are additional free parameters θ_{syst} in the model, e.g. magnetic fields, so called pull-terms or nuisance parameters. Through these additional degrees of freedom,

the uncertainties of the fitting parameters are increased reflecting the impact of systematic uncertainties. This method is straightforward, but goes along with increasing complexity of minimization.

Another possibility is the covariance matrix approach. Here the χ^2 function, eq. (3.15), is extended to

$$\chi^2(\mu|x) = (x-\mu)^{\mathrm{T}} V^{-1} (x-\mu) \tag{3.16}$$

with the covariance matrix V

$$\begin{bmatrix} V[x_1] & \mathrm{cov}[x_1, x_2] & ... & \mathrm{cov}[x_1, x_n] \\ \vdots & ... & ... & \vdots \\ \vdots & ... & ... & \vdots \\ \mathrm{cov}[x_n, x_1] & ... & ... & V[x_n] \end{bmatrix}. \tag{3.17}$$

The diagonal entries are the variances given by $V[x] = E[x^2] - E[x]^2$ with the expectation value E. Off-diagonal elements represent covariances, in case of uncorrelated data points, e.g. only statistics, $\mathrm{cov}[x_i, x_j] = 0$. Systematic effects, like varying tritium source properties, do not affect each point independently but alter the spectrum in a correlated way, such that $\mathrm{cov}[x_i, x_j] \neq 0$. The covariance matrix is computed from thousands of model spectra where the systematic parameter is varied according to its distribution. From those the variances and covariances are computed. These matrices are additive such that combinations of systematic effects can be studied easily. The covariance matrix approach can be applied for data sets with large statistics where a χ^2 minimization is valid [47].

The third systematics option in Fitrium is Monte Carlo propagation of uncertainty [46]. Here the model parameters are varied randomly based on their distribution and a fit is performed. By fitting the spectrum multiple times with a different model, a distribution of fit parameters, e.g. neutrino mass squared, is obtained. The width reflects the uncertainty, which grows according to the systematic error. This way parameter uncertainties are propagated into the fit result. An example of such a distribution with statistics only and under consideration of an additional systematic (exaggerated for visualization) is shown in fig. 3.8. For statistical fluctuations only, the orange distribution of neutrino mass squares is obtained. Its width reflects the statistical uncertainty. Adding a systematic, in this case a very exaggerated one, the distribution gets broadened. The increased width directly reflects the worsened sensitivity.

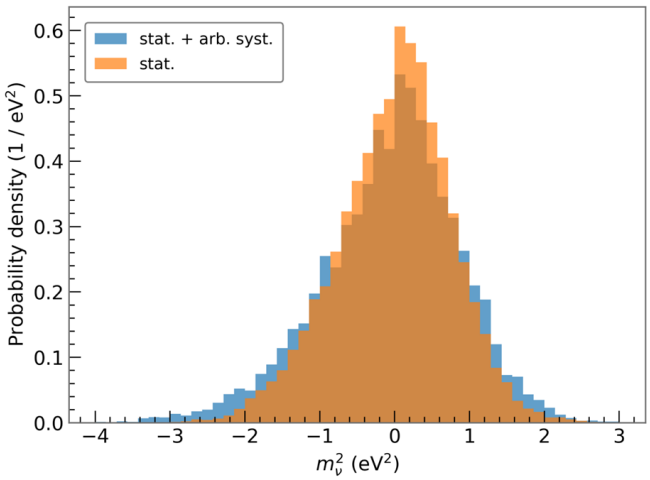

Figure 3.8: Example neutrino mass squared distribution from a MC Propagation with statistics only (orange). Through systematic effects the distribution is broadened displaying the impact of such an uncertainty on the neutrino mass (blue). Figure from [60].

3.4 Importance of low background in KATRIN

The KATRIN experiment is designed for a neutrino mass sensitivity of 0.2 eV at 90 % C.L. after three years of data taking, corresponding to five calendar years. This challenging goal implies a tight systematics budget and a low background level in the order of 10 mcps (technical design value [4]). By the time of the first measurements with tritium, the background rate was in the order of 400 mcps (whole detector). The impact of such elevated background rates on the integrated tritium β-spectrum is shown in fig. 3.9(a). It is calculated from the ratio of integrated tritium spectra with and without neutrino mass of $m_\nu = 0.5\,\text{eV}$. The blue dotted curve corresponds to the design case with a background rate of 10 mcps. For increasing background rates, the neutrino mass signal decreases significantly and moves deeper into the tritium spectrum.

This behavior directly translates into a worsened neutrino mass sensitivity shown in fig. 3.9(b). The curve is computed considering statistics of three years and the fit range from the TDR of $E_0 - 30\,\text{eV}$ [4]. The detailed settings are based on the configuration used in the first KATRIN neutrino mass measurement campaign (**K**atrin **N**eutrino **M**ass 1 (KNM1)) and are listed within appendix A.2. With the KATRIN design background value of 10 mcps, the targeted neutrino mass sensitivity of 0.2 eV at 90 % C.L. is achieved. With highly elevated background rates this goal can not be accomplished. There are several ways to improve this situation:

- **Increased measurement time**: The statistical sensitivity improves with the measurement time until systematic uncertainties prevail. Considering only statistics this dependency goes via $t^{-1/4}$. Therefore the worsened sensitivity due to highly elevated background can not be easily balanced by an increased measurement time.
- **Extended analysis interval**: Increasing the analysis interval from $E_0 - 30\,\mathrm{eV}$, further into the tritium spectrum, to for instance 45 eV, improves the statistical sensitivity. However, deeper into the spectrum, the impact of systematic uncertainties strongly increases, especially from FSD and response function [47]. Therefore without improved knowledge on both, this approach is not beneficial.
- **ROI**: A more narrow ROI leads to a lower background rate (see section 4.3). But this way not only background events are reduced, also the signal is. Therefore this approach can only improve the sensitivity to a limited extent.
- **Magnetic flux volume**: The background rate is approximately proportional to the magnetic flux volume (see section 4.3). Increasing B_{min} reduces this volume and thus the background rate. However an increase of B_{min} comes together with a worsened energy resolution. For KNM1 (and also for the first injection of tritium [61], so-called **F**irst **T**ritium (FT)) those parameters were optimized in terms of best achievable sensitivity. Like the ROI this adjustment can only improve the situation to a limited extent.

It follows from above considerations that the background rate needs to be reduced by other means to reach the targeted neutrino mass sensitivity. This requires a detailed understanding of the contributing processes and development of efficient countermeasures. That is the main subject of this work, which focuses on the characterization of the residual elevated background and its potential mitigation. Precise knowledge is not only of importance in terms of mitigation but also in context of spectral analysis.

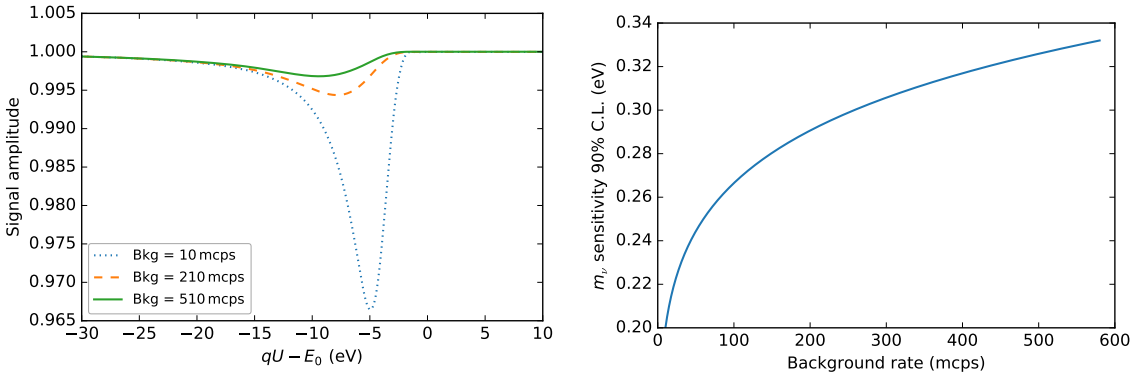

(a) (b)

Figure 3.9: (a) Neutrino mass signal amplitude for different background levels. The signal amplitude is defined as the ratio of the integrated tritium spectra without and with neutrino mass of 0.5 eV.
(b) KATRIN neutrino mass sensitivity for different background levels.

4 Overview of background processes

Potential background generation mechanisms were studied during various commissioning measurements and possible countermeasures developed. Contributions arise from intrinsic detector background and electrons generated within the spectrometers. All electrons created inside the magnetic flux tube of the spectrometer volume potentially generate background. Those created outside the flux volume but within the spectrometer are not mapped onto the detector and can hence not contribute to the measured background. Due to the much higher volume of the MS with $V_{\mathrm{MS}} = 1240\,\mathrm{m}^3$ in comparison to the PS with $V_{\mathrm{PS}} = 24\,\mathrm{m}^3$ the latter contribution is negligible. This is reinforced by the potential settings. The PS is usually at lower retarding potential than the MS, hence low energetic background electrons created in the PS cannot pass towards the detector. Currently the background rate in KATRIN is with a level of few hundreds of mcps by more than a factor of ten above the design. Predominantly three processes create this elevated rate: Detector, radon and Rydberg induced backgrounds. They are discussed in section 4.1. Minor contributions are presented in section 4.2. This chapter is concluded by the evolution of the overall background rate from the year 2015 to 2019.

4.1 Main background components

4.1.1 Detector background

All electrons within the ROI contribute to the background. The design intrinsic background rate of the FPD is 1 mcps [4]. It is dominated by environmental radiation, mainly arising from β-electrons of ^{40}K, and cosmic-ray muons. In order to counteract these background sources a layered Pb-Cu shielding and a muon scintillator veto were introduced. In addition materials with low radioactive contamination were chosen. Another means for background reduction is the **p**ost **a**cceleration **e**lectrode (PAE) which accelerates the signal to a region of lower intrinsic detector background. It is usually at a voltage of $U_{\mathrm{PAE}} = 10\,\mathrm{kV}$. This results in a detector background of $2\,\mathrm{mcps{\cdot}keV^{-1}}$ during KNM1 [62]. In this campaign a ROI of 14 to 32 keV was used (with the PAE at 10 kV β-electrons close to the endpoint have energies around

28.6 keV when they are detected), resulting in 36 mcps. Compared to the overall background rate of (291 ± 1) mcps this corresponds to about 12 %. It can be reduced through multi-pixel coincidence cuts and by using the information from the installed detector muon veto to 18 mcps. So far the cuts are not applied since radon and Rydberg induced backgrounds prevail. However promising mitigation strategies potentially raise the detector background's contribution to 30 % necessitating known reduction strategies.

4.1.2 Radon-induced background

The MAC-E filter configuration of the KATRIN spectrometers enables precise energy analysis. At the same time this configuration creates through the high magnetic fields at both ends a magnetic bottle for electrons created within the spectrometers. An electron generated inside the MS is accelerated by the decreasing potential towards the ends of the spectrometer, gaining longitudinal energy. At the same time it is guided towards regions with higher magnetic field. On this way longitudinal energy is transformed to transversal energy. If transversal energy prevails the electron will be reflected by the high magnetic field, hence stored within the spectrometer. Stable storing is achieved when

$$E_\perp > U_{\mathrm{ret}}(x) \cdot \frac{B(x)}{B_{\mathrm{max}}} \tag{4.1}$$

where $U_{\mathrm{ret}}(x)$ and $B(x)$ are retarding potential and magnetic field at the position of electron generation. In other words, electrons created within the MS are stored when their transversal energy is larger than the spectrometers energy resolution (see eq. (3.3) in section 3.1). The motion of such a trapped particle within the MS is depicted in fig. 4.1. It is composed of three parts: axial motion along the magnetic field lines, a cyclotron orbit around the magnetic field line with the frequency

$$\omega_{\mathrm{c}} = \frac{q \cdot B}{m} \tag{4.2}$$

and a magnetron drift. The radius of cyclotron motion, also referred to as radius of gyration, is given by

$$r_{\mathrm{c}} = \frac{m \cdot v_\perp}{q \cdot B}. \tag{4.3}$$

Therefore electrons with very large transversal velocities can have cyclotron radii larger than the spectrometer's dimensions. With a magnetic field of $B = 3\,\mathrm{G}$ this is the case for $E_\perp > 200\,\mathrm{keV}$. Such electrons hit the spectrometer wall and are not stored. Trapped particles can only escape by breaking the storage conditions.

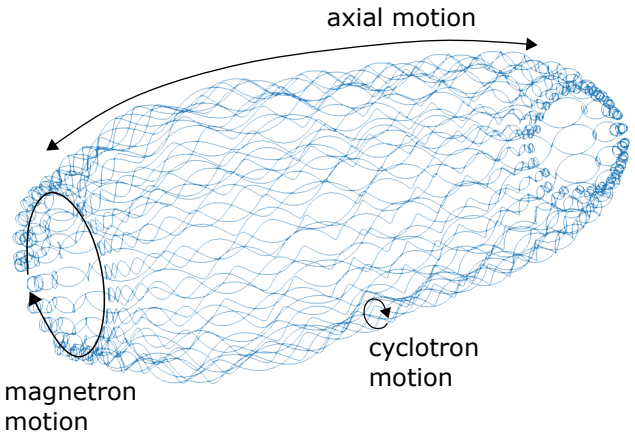

Figure 4.1: Trajectory of a trapped particle inside the MS. Besides its axial motion along the magnetic field lines, it performs a cyclotron motion around the magnetic field line and magnetron drift (because of field inhomogeneities).

This can be achieved by either (multiple) scattering(s), where the angle and hence transversal energy is changed, or by non-adiabatic motion. Due to the enormous mean free path in the **U**ltra **H**igh **V**acuum (UHV) of the spectrometers electrons can be stored up to several hours. During their storage low energetic secondary electrons are created along their trajectory through ionization of residual gas. Those electrons are usually not stored but leave the spectrometer undisturbed and elevate the background until the primary electron no longer fulfills storing conditions. Such events are correlated in time and hence not Poisson distributed. This background property has significant consequences in terms of neutrino mass sensitivity [63] and will also be discussed in context of KNM1 in chapter 6.

The dominant source of stored electrons in KATRIN are radon decays. Due to the short pumping time achieved by large TMPs of 360 s [63], only short living isotopes are of importance for KATRIN. Therefore ^{222}Rn with a half-live of 3.8 d is pumped off before decaying and can not contribute to the background. However two short living radon isotopes, ^{219}Rn and ^{220}Rn, with the half-lives of 4 s and 56 s, can decay within the sensitive flux volume before being pumped. They decay homogeneously distributed in the spectrometer volume and create background events in the same manner. In the following the origin of radon in KATRIN, subsequent electron creation and mitigation strategies are summarized. More detailed information can be found in [64, 65, 66, 67, 63, 68].

Sources of radon in KATRIN

Radon is a noble gas also abundant in ambient air (in Germany the typical level is at the order of $50\,\mathrm{Bq{\cdot}m^{-3}}$ inside buildings [69]) originating from natural radioactivity of uranium and thorium. Before evacuation radon could accumulate in the stainless steel of the spectrometers. Hence small amounts of radon emanate from the spectrometer walls, which can be estimated from measurements. From the surfaces $(4 \pm 4) \cdot 10^{-5}\,\mathrm{s^{-1}}$ and $(12 \pm 8) \cdot 10^{-5}\,\mathrm{s^{-1}}$ of ^{219}Rn and ^{220}Rn, respectively, is emanated. Measurements showed that the radon activity on the walls is in agreement with zero [64] and hence negligible. However the **n**on-**e**vaporable **g**etter (NEG) strips, installed to suppress potential tritium activity in the spectrometers, emanate ^{219}Rn with a rate of $(0.12 \pm 0.03)\,\mathrm{s^{-1}}$ [63] causing significant radon activity.

Electron emission following radon α-decay

When radon decays, high energetic electrons are created as a consequence of α-decay. In one α-decay multiple electrons can be generated via shake-off, internal conversion and relaxation processes. Those processes are schematically shown in fig. 4.2. ^{219}Rn decays under emission of an α-particle to ^{215}Po. The emitted α-particle can interact through the Coulomb field with inner shell electrons when leaving the nucleus and ionize e.g. K-shell electrons [70]. These so-called shake-off electrons have energies up to $\mathcal{O}(\mathrm{keV})$. This process occurs mainly for inner shell electrons where the α-particle causes an adiabatic perturbation. Outer shell electrons adopt to the sudden change of nuclear charge by emitting so-called shell reorganization electron. This is the most common electron emission process, emitting electrons with energies less than 1 keV. The emerging vacancy is filled by relaxation processes, where binding energy is released in form of either X-rays or electrons. Radiation will be absorbed by the spectrometer walls and is of no concern in terms of background. Electrons can be either emitted via an Auger process (depicted in fig. 4.2) or by Coster-Kronig transitions. This results in low energetic electrons with energies less than 1 keV. In about 20 % of ^{219}Rn decays, polonium is left in an excited state. One possibility to leave this state is internal conversion. Here the energy is not emitted in from of γ-radiation but transferred to an electron. The electron leaves with the energy $E_{\mathrm{IE}} = E^* - E_{\mathrm{B}} - E_{\mathrm{recoil}}$, where E^* is the excitation energy, E_{B} the binding energy and E_{recoil} the radon recoil. In radon the daughter nucleus can be left in excited states with for example the energies 401.8 keV and 271.2 keV [71], as shown in fig. 4.2. Generated vacancies are compensated by relaxation processes, like after shake-off electron emission.

Electrons emitted from radon decay have energies in the range of 10^{-3} to 10^{2} keV.

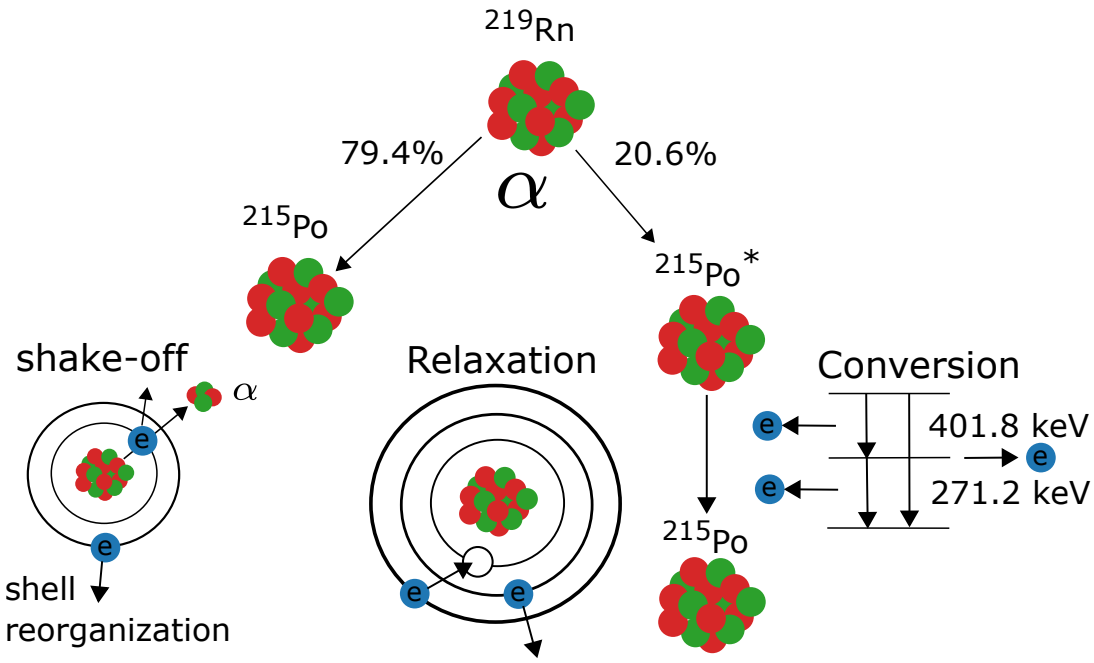

Figure 4.2: Electron creation following the α-decay of ^{219}Rn. Electrons are created through shake-off, conversion and relaxation processes. Figure adopted from [68].

Hence they have a high chance of obtaining transversal energies larger than the spectrometer resolution, leading to a significant storage probability. Their storage time determines the number of secondary electrons produced through residual gas ionization. For an emitted primary electron with the energy E_{primary}

$$N_{\text{secondary}}(E_{\text{primary}}) \approx \frac{E_{\text{primary}}}{\langle E_{\text{loss}} \rangle} \tag{4.4}$$

secondary electrons are produced in the spectrometer. The term $\langle E_{\text{loss}} \rangle$ denotes the average energy loss for ionization. Hence higher energetic primary electrons create more secondary electrons and hence higher background. An electron with $E_{\text{primary}} = \mathcal{O}(\text{keV})$ creates up to $\mathcal{O}(100)$ secondary electrons. For very high energies, $E_{\text{primary}} > 10\,\text{keV}$, the number of created secondary electrons $N_{\text{secondary}}$ decreases again due to non-adiabatic effects [65].

Radon retention

The dominant origin of radon is the material of the NEG pumps. To prevent radon from entering the MS volume liquid nitrogen cooled baffles were installed in front of every getter pump in each of the pumping ports. Those baffles are several copper

strips installed as visualized in fig. 4.3. They are arranged such that there is no direct line of sight into the MS for radon. Emanating radon will stick to the cooled surface and is thus prevented from entering the sensitive spectrometer volume. The sticking time to the baffle surface is defined by the sojourn time τ_{des}. As long as radon decays when it is still attached to the surface it can not contribute to the background within the flux tube. For ^{219}Rn a sojourn time of 10 s is sufficient [72]. The baffle's sojourn time depends on its surface condition and temperature as shown in fig. 4.4. Even under UHV conditions formation of an oxide layer is unavoidable causing degraded efficiency. In normal operation the baffles are at temperatures of 82 to 88 K resulting in a suitable sojourn time. Their performance at the MS was investigated for instance in [64] and confirmed by background measurements within [73]. With all three baffles cooled down, only a background fraction of (1.99 ± 0.07) ‰ [73] at nominal pressure of 10^{-11} mbar shows correlated characteristics, indicating a very small radon contribution. The remaining radon-induced background from the NEG pumps was determined based on measurements and simulations by [64] to be (36^{+18}_{-15}) mcps. This is confirmed by measurements in [51] and within this thesis, see section 5.1.3. Hence radon-induced background is of similar order as the detector induced background. Given its additional non Poisson characteristic mitigation is essential. Possible strategies are:

- **Electron Cyclotron Resonance (ECR)**: Through application of a high frequency pulse, tuned to ω_{c}, stored electrons gain energy until their cyclotron radius gets larger than the spectrometer radius. It is sufficient to remove stored electrons within a timescale of $\mathcal{O}$(ms). This principle was successfully tested at the PS in [65], where the background could be reduced by a factor of 7. The hardware for application at the MS is at present not installed.

- **Magnetic pulse**: In normal operation the magnetic flux tube embedded within the MS is shaped by the air coil system. Through reduction of the magnetic field, e.g. change of air coil polarities, the flux tube is distorted and opened such that the magnetic field lines connect to the walls. In this process stored particles collide with the walls and are removed from the spectrometer volume. Necessary hardware was installed at the MS and tested with a radon and krypton source [74]. With a reduction efficiency of 0.6, this method is suitable for stored particle removal. The application of such a magnetic pulse takes only $\mathcal{O}$(s) and can hence be applied in between retarding voltage steps without prolonging the overall KATRIN measurement time significantly.

- **Electric dipole**: The applied high voltage at the MS is tuned by the **I**nner **E**lectrode (IE) system, see section 3.1. By putting different voltages on the MS east and west dipole halves, an electric dipole field is created as shown in fig. 4.5(a). Thereby stored electrons are removed by an $E \times B$ drift as depicted

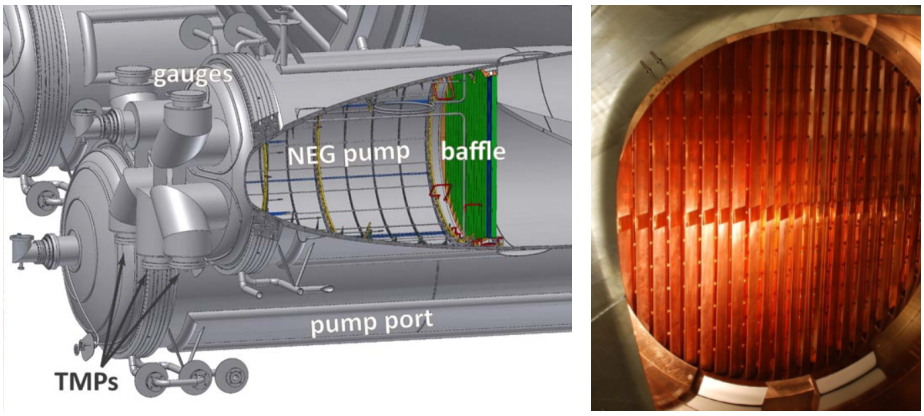

(a) MS pump port (b) Baffle

Figure 4.3: (a) Schematic view on one of the MS pump ports with the NEG pump. In front a cold baffle is installed to prevent radon from entering the spectrometer. Picture from [72]. (b) Close view on the installed copper baffle. Picture from [75].

in fig. 4.5(b). For removal of a 1 keV electron, a dipole field of $50\,\mathrm{V{\cdot}m^{-1}}$ is sufficient [68]. With a background level of (530.8 ± 8.6) mcps a reduction by (45.6 ± 16.2) mcps was observed in measurements performed within [51]. This is in agreement with the residual radon-induced background determined in [64]. Hence this method is suitable to remove radon-induced background. Like the magnetic pulse the electric dipole pulse takes only $\mathcal{O}(\mathrm{s})$. It could be applied in tritium β-decay measurements during high voltage changes such that only minor time loss occurs.

For two of those active background reduction methods the required hardware is currently installed. They could in principle be applied during neutrino mass measurements. However long-term background rate investigations should be carried out prior to guarantee a stable rate since both methods can potentially also capture electrons from the walls into the flux volume. They are also essential to determine the repetition rate of applied measures.

4.1.3 Rydberg induced background

Detector and radon-induced background together generate a background rate of less than 100 mcps. The dominant residual background fraction is

- increasing for outer spectrometer radii,
- proportional to the volume (except the outer radii),

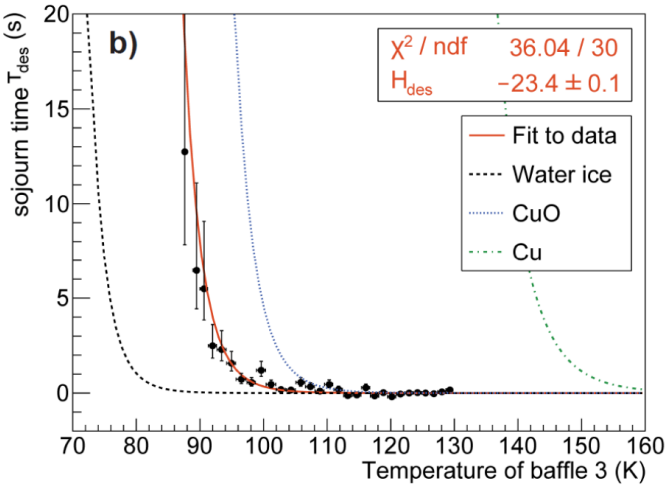

Figure 4.4: Sojourn time of copper baffles as a function of temperature. There is a strong dependency of the sticking time on the surface condition. The shown data was taken with an artificial ^{220}Rn source. In normal operation the baffles are operated below 90 K. Figure from [76].

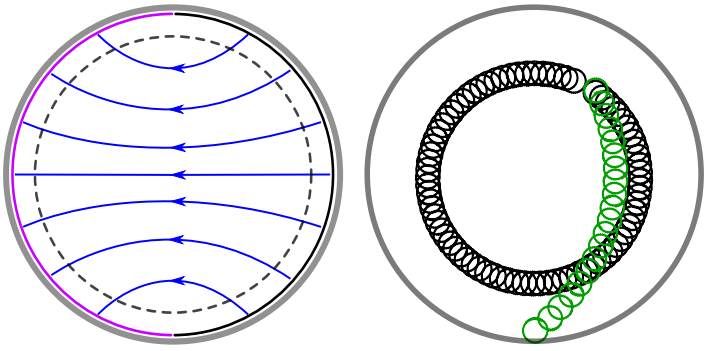

(a) Dipole field (b) Electron removal

Figure 4.5: (a) Induced electric dipole field in the MS achieved through application of different voltages on the east and west electrodes. (b) Principle of electron removal with an electric dipole field. Electrons drift out via the Lorentz force. Figures from [68].

- increased with raised spectrometer hull temperature,
- suppressed by more negative IE voltages,
- decreasing for very low retarding potentials qU.

Those characteristics are to a large extent in agreement with low energetic electrons created within the MS volume. Since charged particles are prevented by electric and magnetic shielding from entering the MS, see section 4.2.3, a neutral messenger particle is required that 'carries' the background electron into the spectrometer. A potential candidate are highly excited atoms, so-called Rydberg atoms, that are ionized in the sensitive flux volume. This background mechanism is schematically summarized within fig. 4.6. Rydberg atoms can be created through α-decays in the spectrometer walls. A potential candidate is the decay of ^{210}Po, a daughter of ^{222}Rn, which accumulated in the spectrometer prior to evacuation. The decay chain of ^{222}Rn is given in eq. (4.5), where channels with less than 1 % probability are neglected.

$$\begin{aligned} {}^{222}\mathrm{Rn} &\xrightarrow[3.82\,\mathrm{d}]{\alpha} {}^{218}\mathrm{Po} \xrightarrow[3.1\,\mathrm{min}]{\alpha} {}^{214}\mathrm{Pb} \xrightarrow[26.8\,\mathrm{min}]{\beta} {}^{214}\mathrm{Bi} \xrightarrow[19.9\,\mathrm{min}]{\beta} {}^{214}\mathrm{Po} \\ &\xrightarrow[164.3\,\mu\mathrm{s}]{\alpha} {}^{210}\mathrm{Pb} \xrightarrow[22.2\,\mathrm{yr}]{\beta} {}^{210}\mathrm{Bi} \xrightarrow[5.01\,\mathrm{d}]{\beta} {}^{210}\mathrm{Po} \xrightarrow[138\,\mathrm{d}]{\alpha} {}^{206}\mathrm{Pb} \end{aligned} \tag{4.5}$$

Through radioactive decays the radon daughter ^{210}Pb is deposited in the spectrometer walls. Abundance of ^{210}Pb in the MS was experimentally confirmed within [64]. Its polonium daughter ^{210}Po decays to ^{206}Pb under emission of an α-particle. The high nuclear recoil in particular of the daughter atom of 103 keV [77], can potentially sputter off atoms from the spectrometer surface. Sputtered atoms together with the daughter nucleus can be implanted again causing a cascade of sputtering processes. Thereby created atoms are neutral and thus not affected by electric and magnetic shielding. Through ionization low energetic electrons can be created. Since there are no high intensity light sources in the MS, ionization through **b**lack-**b**ody **r**adiation (BBR) is an option. At room temperature this requires the atom to be in a highly excited state. Created low energetic electrons are not stored within the magnetic bottle, but leave the spectrometer guided by the magnetic field lines. Accelerated by the retarding potential they are indistinguishable from signal β-electrons. So far this background model could neither be clearly confirmed nor rebutted. Detailed simulations of the mechanism could reproduce the residual background characteristics, aside from the qU dependence, indicating validity of the 'Rydberg model' [73]. In the following the origin of the Rydberg atoms and the expected electron energies are discussed predominantly based on [73, 78]. To verify the Rydberg background

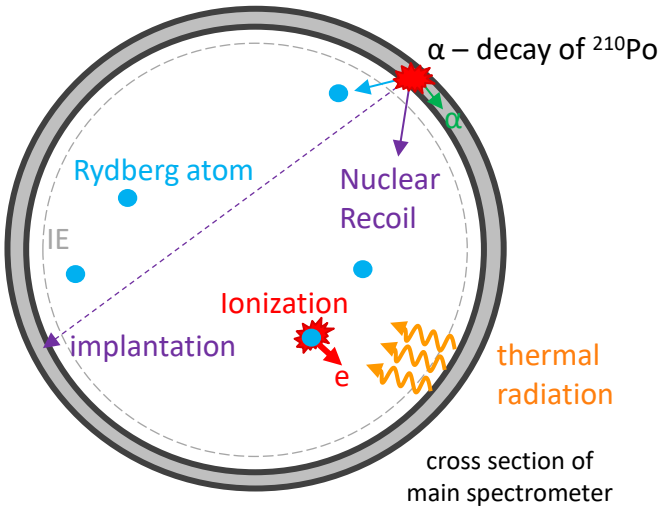

Figure 4.6: Rydberg background generation mechanism: α-decays in the walls induce a sputtering process emitting highly excited atoms. Through ionization by e.g. thermal radiation low energetic electrons are created.

hypothesis experimentally, dedicated measurements are carried out within this thesis described in chapter 5.

Sputtering in the KATRIN main spectrometer - origin of the Rydberg atoms

From measurements it is known that the spectrometer is contaminated with ^{210}Pb [64]. Dedicated investigations with an artificial radon source, ^{228}Th, further showed a clear correlation between surface activity and observed background [79, 80]. Those results are confirmed by measurements with ^{223}Ra, see section 5.2. Both point towards surface contamination as a source of background. A possible generation mechanism of Rydberg atoms at the spectrometer surface is a sputtering process. Investigations within [81] also indicate that ^{206}Pb emitted from ^{210}Po decay is re-implanted again in the walls. This is confirmed by simulations with the software **S**topping **R**ange of **I**ons in **M**atter (SRIM)[1], where sputter yields, implantation profiles, velocity distributions of sputtered particles, etc. can be calculated [78, 77]. The sputter yield depends on the energy and mass of the sputtering particle, the recoiling mass and the energy transfer. It denotes the number of sputtered atoms produced per radioactive decay. In case of α-decay induced sputtering, it is mainly determined by the heavy daughter nuclei, not the α-particle, hence its impact can be neglected [73]. In the simulations the surface composition of the MS is considered as well as the implantation profile. Based on this, the kind of sputtered atoms as

[1] www.srim.org

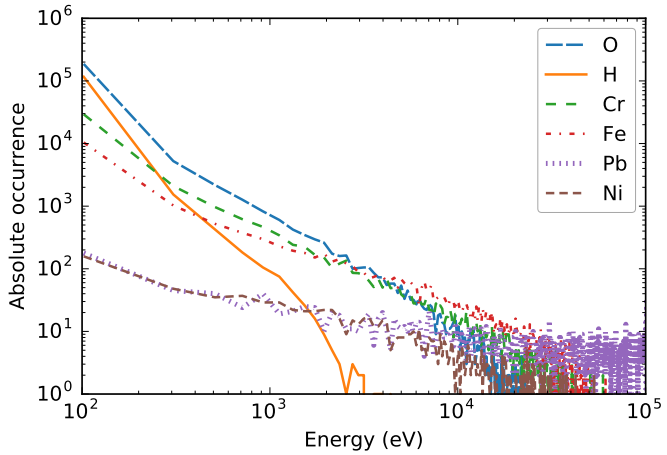

Figure 4.7: Energy distribution of sputtered atoms following the α-decay of ^{210}Po. The most abundant atoms are hydrogen and oxygen. Simulation carried out by Alexander Osipowicz.

well as their energy distribution can be determined. Figure 4.7 shows the number of atoms and their energies for 30 000 ^{206}Pb atoms (primary atom) emitted from the surface. The results show that mostly hydrogen and oxygen atoms are emitted in this process. Assuming a water coverage instead of hydrogen increases the sputter yield by about 25 % especially for oxygen [73]. Therefore removal of water from the system, by baking the spectrometer[2], helps to reduce the induced background. This can also be seen in the long term evolution of the background rate, discussed in section 4.3.

During the sputtering process the primary atom forces surface atoms to leave the solid. A fraction of those atoms can be ionized or in an excited state [82, 83]. Various processes as well as the properties of the solid determine this fraction. Excitations can for example occur through scattering by electrons. Further details can be found in [73, 82]. In conclusion, α-decay induced sputtering creates neutral atoms, which can be in excited states, distributed nearly uniform over the spectrometer volume. Depending on their excitation state they will decay via spontaneous emission before reaching the spectrometer center. The lifetime τ depends on the excitation level n with $\tau \propto n^{-3}$. Therefore close to the walls a larger number of Rydberg atoms is expected and hence a higher background rate, consistent with observations (see for instance fig. 4.18(a)).

[2] complete spectrometer is heated to 350 °C

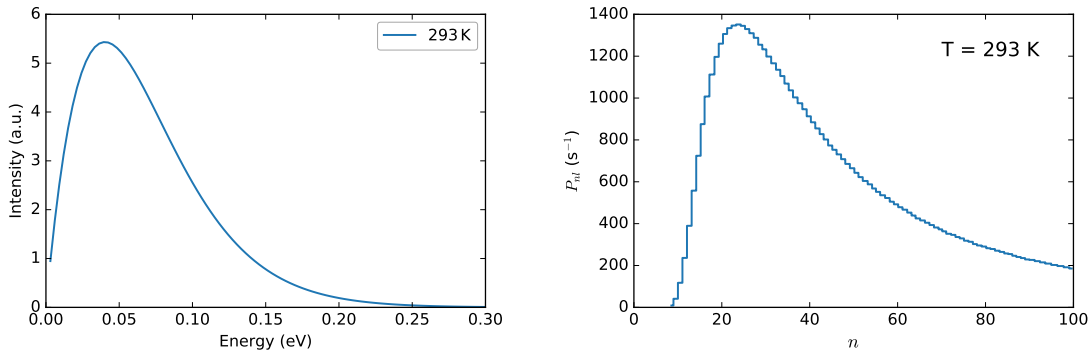

(a) BBR spectrum

(b) Photoionization rate

Figure 4.8: (a) BBR-spectrum at room temperature. (b) Photoionization rate P_{nl} for $l = 1$ as a function of quantum number n. Ionization rates calculated by Ferenc Glück.

Ionization of Rydberg atoms - creation of low energetic electrons

Only through ionization the above described sputtering process contributes to the background. Given the lack of light sources in the MS possibilities are restricted. One eventuality is ionization through thermal radiation. The spectrum of **b**lack-**b**ody **r**adiation (BBR) at room temperature is shown in fig. 4.8(a). For Rydberg states the energy difference between two states n_1, n_2 is given by

$$\Delta E = E_{\mathrm{Ryd}} \left(\frac{1}{n_1^2} - \frac{1}{n_2^2} \right) \tag{4.6}$$

with the Rydberg energy $E_{\mathrm{Ryd}} = 13.6\,\mathrm{eV}$. BBR at room temperature has a maximal energy of 300 meV. Therefore the lowest Rydberg state that can be ionized is $n = 7$. The ionization rates for n up to 100 are shown in fig. 4.8(b). Although states with $n = 7$ can be ionized at room temperature, more probable are states with lower binding energies with $n > 15$. Ionization of Rydberg states through thermal radiation results in electrons with energies shown in fig. 4.9. Electrons created in this way have energies below 100 meV. Due to this exceedingly small energy such electrons are not stored within the spectrometer and will be directly detected as background. If BBR ionizes the Rydberg atoms a temperature dependency of the background rate should be observed. This was experimentally confirmed in [73] indicating that BBR radiation contributes to background generation.

An additional ionization mechanism that should be considered is field ionization. External electric fields distort the atom's potential. If this field is sufficiently large, the distortion of the field causes ionization. Without external field, electrons are bound in the Coulomb potential, as illustrated in fig. 4.10. If they gain enough

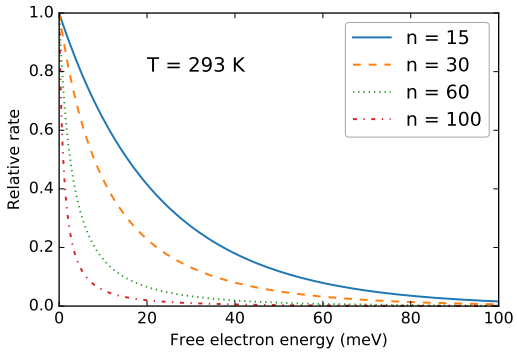

Figure 4.9: Expected electron energies from ionization of Rydberg atoms for some states with $n > 15$ by BBR. Electron energies calculated by Ferenc Glück.

energy to overcome the ionization limit, they become free electrons. Under influence of an external electric field the binding potential gets strongly distorted. This lowers the ionization limit allowing bound electrons to become free, field ionization occurs. In addition there is a probability for tunneling, however this decreases exponentially below the ionization limit. Field ionization is especially prominent at sharp edges that are on high potential. Such environment is given close to the inner electrodes and their holding structure [78]. Electric fields also appear when an electron moves through a magnetic field. However due to the low field strengths in KATRIN this can be neglected. Since field ionization can only occur close to the wire electrodes it can not create electrons distributed over the whole spectrometer volume. But it can potentially contribute to the radial dependency of the background. In addition this ionization mechanism leads to an IE voltage dependency. With higher voltages more Rydberg states are field ionized close to the electrodes. Those states can no longer contribute to the background rate within the volume, leading to a decreasing background rate. Good agreement between simulation and measurement confirms this hypothesis [73].

4.2 Minor background contributions

4.2.1 Tritium β-decay in the MS

Blocking of tritium, in form of gas or ions is of highest importance, because β-decay electrons created in the spectrometers would intermix with those emitted in the WGTS and create a retarding potential dependent background within the measured tritium β-electron spectrum. In addition, those electrons have high surplus energies

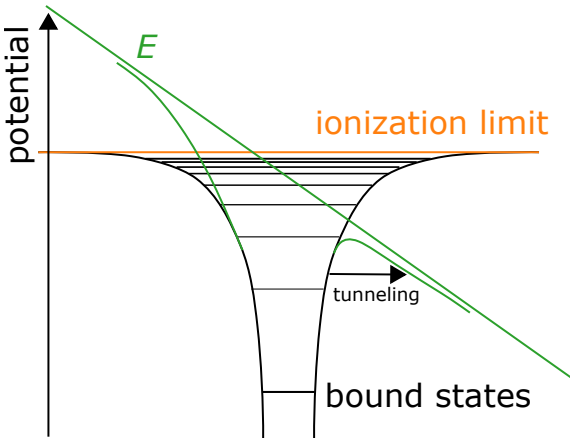

Figure 4.10: Coulomb potential of an hydrogen atom. In an external electric field this potential is strongly distorted, causing bound states to be below the ionization limit. This is referred to as field ionization.

going along with a high storage probability in the spectrometers. Like radon (see section 4.1.2), they create background events through scattering with residual gas until the primary electron escapes the magnetic trap. To minimize such background generation multiple countermeasures are installed.

The flow of neutral tritium molecules is reduced in the **s**ource and **t**ransport **s**ection (STS). In the initial design a reduction by 14 orders of magnitude is foreseen to limit induced background to 1 mcps. Simulations of the DPS and CPS retention capability yield a total reduction factor of larger than $2 \cdot 10^{19}$, exceeding the design value by five orders of magnitude [84]. This result is supported by ongoing measurements. Remaining tritium activity entering the spectrometer section is additionally reduced by NEG strips that pump hydrogen and nitrogen with a higher speed than the TMPs.

Tritium ions however are not as affected by those measures since they are guided through the transport section by the magnetic field lines like β-electrons. Altogether $2 \cdot 10^{11}$ positive tritium ions T^+ and $2 \cdot 10^{10}$ T^- ions per second are created in the WGTS [85]. Whereas negative ions are reflected by the potential in the PS, positive ions are accelerated. Their motion becomes non-adiabatic such that most ions hit the spectrometer surface, where they are implanted. Those ions can emerge again from the solid, mainly in form of neutral HT molecules, and eventually reach the MS [86]. Besides β-decay, a high ion flux into the spectrometers also causes background through ionization of residual gas. To prevent ions already from entering the spectrometers multiple countermeasures are installed. Positive ions are blocked by three ring electrodes operated at positive potential, installed in the DPS and at the entrance of the PS. To prevent forming of a local charge between the ring

electrodes, stored ions are removed by electric dipoles through an $\vec{E} \times \vec{B}$ drift. Those dipoles are operated on negative voltage thus also blocking negative ions. This arrangement of blocking voltages and dipoles reduces the ion flux such that no significant background increase is observed [86, 30].

4.2.2 β-induced background

During neutrino mass measurements a high β-electron flux enters the spectrometer section. This high flux generates low energetic electrons together with positive ions through ionization of residual gas. A large fraction of the created electrons is reflected by the high negative potential in the MS and can therefore not contribute to the background. However, the created positive ions are accelerated by this potential into the MS volume and create electrons by residual gas ionization that are likely to be detected.

To reduce the flux of β-electrons into the MS, the PS is operated at slightly less negative voltage than the MS, hence acting as a pre-filter. In addition positive ions created in the PS can be prevented from entering the MS by a positively charged ring electrode between the two spectrometers. To investigate the background suppression efficiency commissioning measurements with an electron flux of $\mathcal{O}(10^8)$ were carried out. They showed that in neutrino mass measurement configuration even without voltage on the PS only an induced background in the order of 10 mcps is expected [30].

4.2.3 Secondary electron emission from the MS surface

High energetic particles, like cosmic-ray muons or gamma radiation emitted primarily from the concrete of the spectrometer hall, can traverse the **m**ain **s**pectrometer hull. They can cause the emission of electrons from metal into vacuum, so-called secondary electrons. The large inner surface of the MS provides a huge area for such secondary electron emission. Just the steel vessel has an inner surface of 690 m^2 and the IEs together with their holding structure offer additional 532 m^2. Electrons emitted from the surface have energies smaller than 50 eV [87]. Such particles are retained from the spectrometer volume by electric and magnetic shielding, described in the following.

The MS is covered by an IE system, shown in fig. 4.11, which also shapes the retarding potential. In normal operation the voltage of these electrodes is more negative than of the vessel, $U_{\mathrm{IE}} < U_{\mathrm{vessel}}$. Therefore electrons created at the vessel walls, e.g. secondary electrons generated from muon or environmental radiation, will

Figure 4.11: The inner surface of the MS is covered by an IE system. Being on more negative potential than the vessel hull, electrons created at the surface are guided back to the walls.

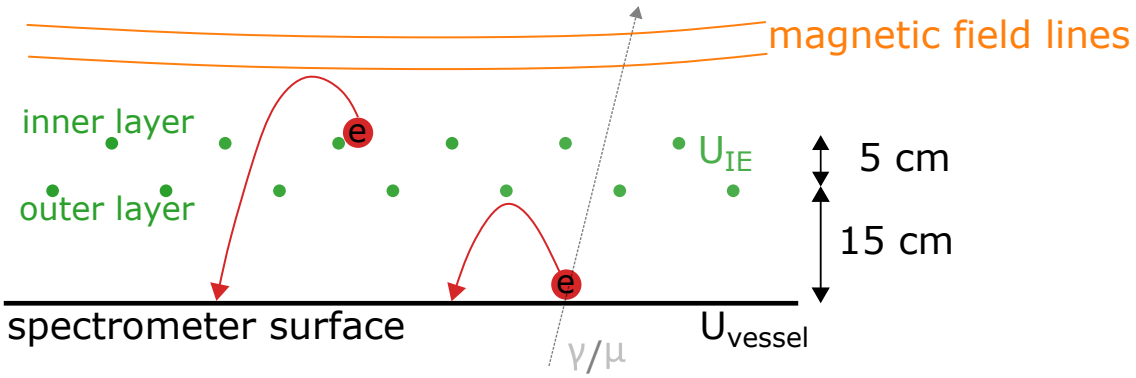

Figure 4.12: Scheme of electric and magnetic shielding in the KATRIN MS. The two layers of inner electrodes are on more negative potential than the vessel, therefore secondary electrons created on the spectrometer surface can not enter the volume. Electron generated at the electrodes are guided back to the walls by the Lorentz force.

be guided back to the walls, as visualized in fig. 4.12. With this configuration the inner volume of the MS is electrically shielded. Two layers of electrodes build this system, originally designed for applying different voltages [88]. This way electrons generated on the outer layer could be repelled by the more negative voltage on the innermost electrodes. However due to shorts between the layers, caused by spectrometer baking, only one common voltage can be applied to the two layers of the electrode system [89]. Hence secondary electrons created at the IEs are not repelled electrically. Such electrons are prevented from entering the flux tube by the magnetic field, referred to as magnetic shielding. With the guiding magnetic field lines parallel to the spectrometer surface, electrons generated at the IEs are guided back to the walls by the Lorentz force. However in case of non parallel magnetic fields electrons can also be brought into the flux volume. Dedicated measurements to investigate induced backgrounds from muons and gamma radiation were performed during the **S**pectrometer and **D**etector **S**ection commissioning phase II (SDS-II) (2014 to 2015). For the former, muon panels were installed around the spectrometer and the correlation of muon flux and background events was evaluated. With standard magnetic field settings no correlation between muon flux and background rate was observed. Based on this measurement an upper limit on the muon induced fraction was derived. From the total background rate at this time of 692 mcps, less than 115 mcps are muon induced [90]. Given the overall rate this fraction was not significant. This measurement should be repeated to estimate the current amount of muon induced background. To investigate induced events from environmental gamma radiation a ^{60}Co source was positioned next to the MS. The results show that less than 6 % of surface emitted electrons are induced from external radiation. In standard measurement configuration this corresponds to a contribution of less than 5.6 mcps at 90 % C.L. [91] to the overall background rate. Those observations confirm efficient shielding of the spectrometer volume.

Another creation possibility of electrons at the surface is field emission. This is likely to occur in UHV conditions when some parts are on high negative voltage. In an early measurement phase, the **S**pectrometer and **D**etector **S**ection commissioning phase I (SDS-I), this was observed [92, 93], already at inner electrode offset voltages of −160 V with respect to the vessel. In later commissioning campaigns this could not be observed anymore. Additionally H^- anions can be created in the same way. Such events can be distinguished from electrons because ions loose more energy in the detector's dead layer. Therefore their peak in the energy spectrum is shifted to lower energies, allowing retention via an appropriate ROI cut. Nevertheless measurements with this kind of background should be avoided, because there are indications for a correlation between H^- creation and field electron emission. Background from anion emission was observed in SDS-I [93] and prior to KNM1 which will be discussed in chapter 6.

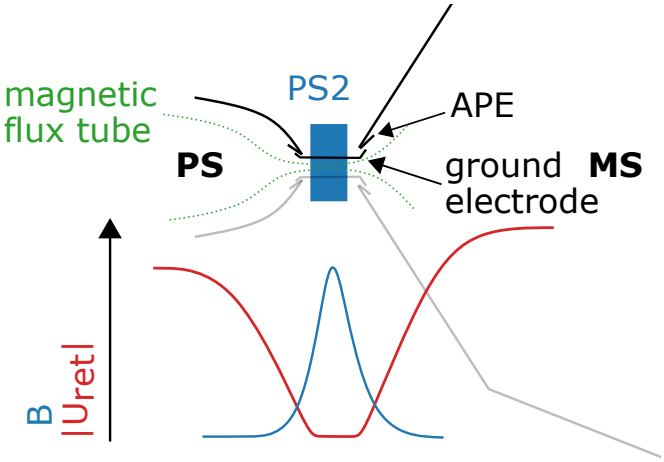

Figure 4.13: Schematic of electric and magnetic fields in between the KATRIN spectrometers. The green lines indicate the magnetic field lines. The APE was installed to prevent formation of Penning traps close to the ground electrode.

4.2.4 Penning trap

Both spectrometers are designed to operate in parallel on voltages below −18 keV, shown schematically in fig. 4.13. In between, where the magnet PS2 is located, the electric potential drops to a minimum. Electrons can become trapped in this region with much less negative potential. Trapping conditions are improved by the high magnetic field of the PS2 magnet with 3.1 T in KNM1 settings. If electrons become trapped they ionize residual gas, creating ions and additional electrons. The positive ions move towards more negative potential and can produce secondary particles when hitting the cathode. Given stable trapping conditions, an avalanche of electrons can be induced. Through scattering, where the angle relative to the magnetic field is changed, electrons can escape the trap, thus creating background events. Whether that happens depends on pressure and electromagnetic field configuration. This was investigated in many measurements at the PS [94, 95]. As a result of these investigations the **A**nti-**P**enning **E**lectrode (APE) was installed to avoid formation of Penning traps close to the ground electrode. This way traps around the electrodes can be prevented by an appropriate electromagnetic configuration, obtained by detailed simulations. To prevent background by the Penning trap between the spectrometers, so-called Penning wipers [96] were installed. These are three movable rods located between the spectrometers. When not operated they are positioned outside of the flux tube. For operation they are moved towards the beam tube center. Through the largely constrained motion of electrons within the trap all of them hit the catcher. Thereby electron creation within the Penning trap is interrupted and background

generation suppressed. Detailed information on the wipers can be found in [96]. Especially under the high flux of β-electrons they are a valuable tool for background suppression, see chapter 6.

4.3 Long-term evolution of background in KATRIN

In section 4.1 and section 4.2, background sources in KATRIN were introduced. At the end of the year 2014 the liquid nitrogen cooled baffle system was installed to suppress radon-induced background. After its installation the contribution from radon/stored particle induced background is significantly reduced. Therewith the background rate is dominated by Rydberg processes supplemented by detector and radon-induced fractions. In this section the time evolution of the overall background rate from the year 2015 to 2019 is evaluated and discussed. Over this time period various measurement configurations and analysis cuts were employed. For comparison their impact on the background rate needs to be taken into account. The main factors influencing the background rate are:

- **Flux volume**: As outlined in section 4.1.3 the background in KATRIN is approximately homogeneously distributed over the spectrometer. Hence the detected rate changes in dependence on the size of the flux volume, determined by the magnetic field configuration. Therefore not the absolute rate is compared but the rate per cubic meter, which is expected to be time-independent. This is not perfectly accurate since the Rydberg induced background increases towards larger spectrometer radii but it is a suitable approximation. The flux volumes for the different configurations are calculated using Kassiopeia (see section 3.3.1). An example of three flux tubes and their corresponding flux volume is shown in fig. 4.14(a).

- **Inner electrode offset voltage**: Due to field ionization processes the Rydberg background depends on the inner electrode voltage. More negative IE offsets lead to a lower background rate. The exact dependency was measured within [73] and is shown in fig. 4.14(b). This measurement is used to scale the background rates to the same IE voltage of −200 V.

- **High voltage**: Towards low retarding potentials the background rate decreases. So far the origin of this behavior is not yet fully understood (investigations on the origin are summarized in section 5.3). Background measurements are usually performed at a retarding potential of 18.6 eV, close to the tritium endpoint. This is also the case for the data sets compared in the following. Therefore no corrections need to be applied in this respect.

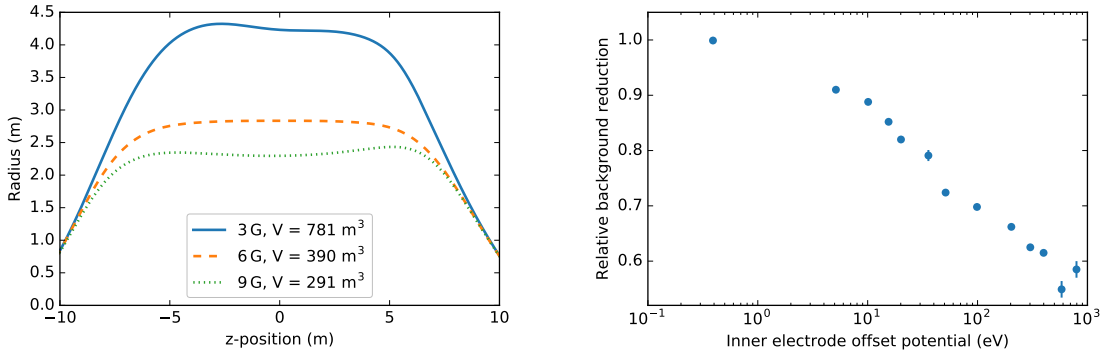

(a) Flux tubes

(b) Inner electrode voltage dependency

Figure 4.14: (a) Outermost radius for three different analyzing plane magnetic fields in the MS (center at $z = 0\,\mathrm{m}$, entrance and exit at $z = \pm 12.5\,\mathrm{m}$). Shown volumes are calculated with Kassiopeia. (b) Dependency of the background rate on the applied IE offset as measured within [73]. As expected from the Rydberg model, the rate is lower for higher potentials.

- **Active pixels**: Depending on the detector setup and magnetic flux tube, not all pixels can be used. Reasons are magnetic flux tube collisions with spectrometer walls or electrodes or defect readout electronics for individual pixels. Under the approximation of a homogeneously distributed background, the rate can be easily scaled to all 148 pixels.

- **Region of interest**: For rate analysis a ROI cut is applied to the measured energy spectrum. Figure 4.15 shows the complete energy spectrum recorded by the FPD with a post-acceleration voltage of 10 kV. Three features are recognizable. The lowest energy peak with about 5 keV is caused by electronic noise. At 10 keV is the so-called PAE-peak resulting from particles accelerated by the PAE onto the detector. The signal peak is at $qU_{\mathrm{ret}} + qU_{\mathrm{PAE}} + qU_{\mathrm{bias}}$ with the detector bias voltage $U_{\mathrm{bias}} = 120\,\mathrm{V}$. In the shown case, where $qU_{\mathrm{ret}} = 18.6\,\mathrm{keV}$, this peak is at $E_{\mathrm{signal}} = 28.7\,\mathrm{keV}$. During SDS measurements, only with spectrometers and detector, the standard ROI is $E_{\mathrm{signal}} \pm 3\,\mathrm{keV}$. For the first two measurement campaigns involving the tritium source, this region was extended to 14 to 32 keV to cut less of the tritium signal. Since only background rates are compared here, the SDS ROI is applied.

Given this knowledge on the background properties, measurements can be analyzed and scaled to generate a comparable data set.

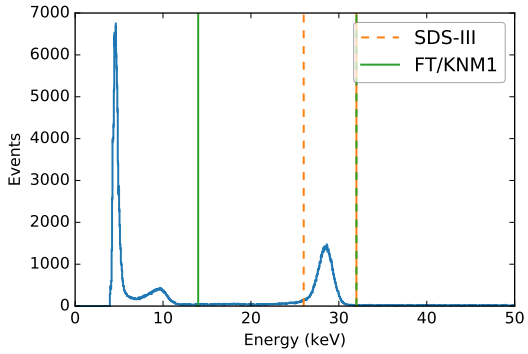

Figure 4.15: Energy spectrum of the FPD detector for a standard background measurement with $U_{\mathrm{PAE}} = 10\,\mathrm{kV}$ and $U_{\mathrm{ret}} = -18.6\,\mathrm{kV}$. Applied ROI cuts in SDS and the first tritium measurements are shown as vertical lines. The visible peaks are described in the text.

4.3.1 Overall background rate from 2015 to 2019

The evolution of the background rate from 2015 to 2019 is shown in fig. 4.16. All data is analyzed with the same ROI cut, scaled to 148 pixels and $U_{\mathrm{IE}} = -200\,\mathrm{V}$. In addition the rates are normalized with respect to the flux volume. For the IE voltage $-200\,\mathrm{V}$ are chosen as reference since most background measurements from December 2017 on are taken with this setting (all that are shown here). The used run numbers for each of the data points are listed in appendix A.3. For standard background measurements one run corresponds to a measurement at constant retarding potential for a specified time. In the analyzed time range the spectrometers were baked two times, indicated by the dashed lines. The different measurement campaigns are indicated in the plot by colored regions. In SDS measurements the valve between spectrometers and the tritium related parts (transport section, WGTS, rear section) is closed. So called STS measurement phases involve also the source and transport section, but no neutrino mass measurements take place. In those campaigns mainly systematic effects are investigated. This includes for example energy loss measurements with the electron gun, calibrations with krypton and background investigations. The most recent phase is called **S**ource and **T**ransport **S**ection commissioning phase 3a (STS3a). During the FT campaign, tritium was injected into the WGTS for the very first time. Two neutrino mass measurement campaigns KNM1 and **K**atrin **N**eutrino **M**ass 2 (KNM2) followed. All measurements from December 2017 on are recorded in nearly equivalent settings, hence there is negligible impact of the applied scalings. In contrast, the data before was taken in various completely different configurations and therefore highly affected by the applied corrections. Here the highest impact of the homogeneous background distribution approximation is expected.

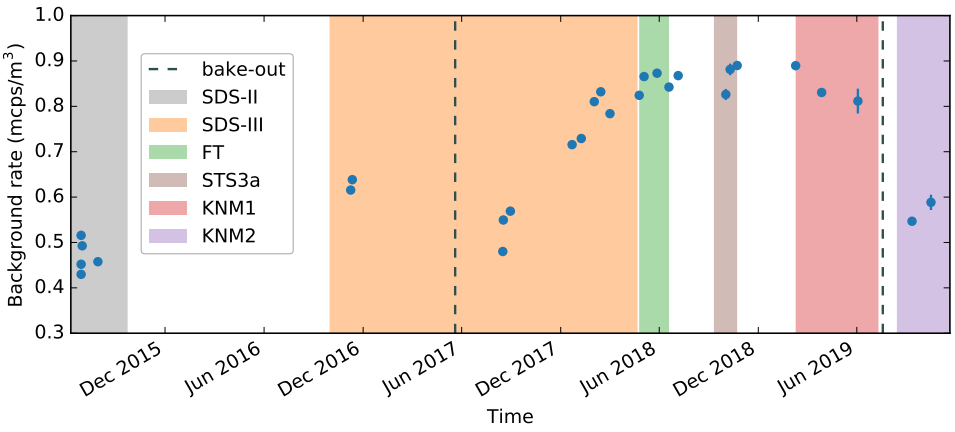

Figure 4.16: Background rate normalized to the flux volume from the year 2015 to 2019. In the shown data all three baffles are cold for radon retention. After 2017 a significant background increase is observed. With the spectrometer bake-out in July 2019, the background rate could be reset.

After installation of the liquid nitrogen cooled baffle system (SDS-II) the background rate was in a range of 0.4 to 0.5 mcps·m^{-3}. In the beginning of **S**pectrometer and **D**etector **S**ection commissioning phase III (SDS-III) the background increased by about 0.1 mcps·m^{-3} to 0.6 mcps·m^{-3}. A baking of the spectrometers decreased the background rate again to nearly the same level as during SDS-II. However over a timescale of months, the rate increased until it reached saturation in June 2018 at a level of nearly 0.9 mcps·m^{-3}. Another baking of the spectrometers accomplished again a temporary reduction of the background rate. But already in KNM2, which took place shortly after the baking, a slight increase is visible. In summary, the background rate shows a significant time dependency that is strongly affected by spectrometer baking. Given the later condition, two components come into considerations as origin of this behavior, namely radon and Rydberg induced backgrounds. Both processes induce background that is expected to be affected by spectrometer baking:

- **Radon**: The radon content in the spectrometer and the subsequently induced background depends decisively on the efficiency of the baffle system. As shown in fig. 4.4, the radon retention capability depends strongly on the surface conditions of the copper. If water freezes onto the material, the baffles can no longer hold radon at temperatures higher than 80 K. Through baking such a water layer is removed, restoring retention efficiency. To keep the radon suppression effective with altered surface conditions in future measurements a sub-cooler is installed in May 2020. It allows operation of the baffles at lower temperatures.

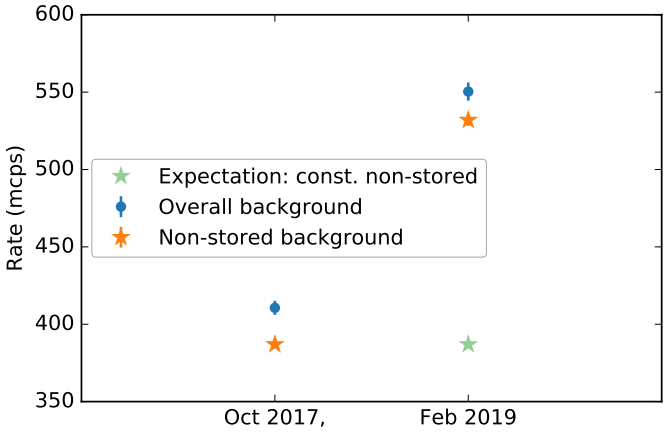

Figure 4.17: Overall background rate and the fraction arising from non-stored electrons measured in October 2017 and February 2019. The green star denotes the expectation in case of a time independent non-stored fraction.

- **Rydberg**: Rydberg atoms are generated through sputtering. In case of a water layer on the spectrometer walls the sputter yield is increased. Hence a higher background rate is expected. Like for the baffle system, baking removes the accumulated water layer from the spectrometer surface. Through reset surface conditions, the sputter yield is lowered again resulting in a decreased background rate.

Independent of the origin of increase, the baking is expected to restore conditions. To determine the time dependent background component, the background composition at low and elevated background needs to be known. One possibility is an experimental determination of the stored particle induced background fraction, described in section 4.3.2. Approaches to separate the background constituents, based on MC simulations, are currently being worked out by Alessandro Schwemmer [97].

4.3.2 Evolution of stored particle induced background

From October 2017 to February 2019 a significant rise in background rate is observed (see fig. 4.16). The stored particle induced contribution can be determined by means of an electric dipole pulse. As described in section 4.1.2 such a pulse removes stored particles. The rate after applying the electric dipole pulse reflects the fraction of non-stored background. The difference in rate corresponds to the amount of trapped particles. Performing a measurement with an electric dipole pulse at low and elevated background gives information on the evolution of stored and non-stored particle

induced fraction. In February 2019 a different detector wafer is installed than in 2017. This impacts the alignment as well as the performance of the individual pixels. Consequently three pixels on the outermost ring are excluded due to misalignment and one pixel due to sporadic noise. The rates are scaled to the whole detector by the factor 148/144 to be comparable to the background rates determined in October 2017. Apart from the pixel cuts, the applied analysis cuts as well as the complete measurement configuration are the same in both measurements. Obtained results are summarized within fig. 4.17. Run numbers of the corresponding data sets are listed in appendix A.3.

Between October 2017 and February 2019 the overall background rate rose by (139.8 ± 7.4) mcps from (410.6 ± 4.6) mcps to (550.4 ± 5.9) mcps. With 'low' background (October 2017) a radon/stored electron contribution of (23.6 ± 5.1) mcps is determined, corresponding at the same time to (387.0 ± 2.4) mcps of non-stored background events (low energetic electrons, e.g. Rydberg mechanism). Assuming an increase of radon contamination as origin of the background increase, the non-stored background component is expected to be the same in February 2019 (indicated by the green star). In case of an elevated Rydberg component, the stored particle induced fraction should stay constant, meaning that the non-stored contribution is expected to increase by the same amount as the overall background rate, so by about 140 mcps. In February 2019, a non-stored electron induced rate of (532.0 ± 3.8) mcps is observed and a stored particle fraction of (18.4 ± 7.0) mcps. The later one is in very good agreement with the radon-induced background observed in October 2017. Hence only the contribution arising from low energetic, non-stored electrons, shows a temporal dependency. This points to an increased Rydberg induced component caused by formation of a water layer on the spectrometer surface (see section 4.1.3).

A look on the radial distribution confirms this hypothesis. Figure 4.18 shows the overall background rate as well as the contribution from stored electrons to this rate as measured in October 2017 and February 2019. The rates are normalized to the flux volume and shown as a function of flux tube radii. Each point corresponds to the background rate of one FPD ring. Comparing the background rates from October and February with each other shows a constant increase over all radii, but an additional stronger pronounced parabolic increase at radii larger than 2 m. Hence the growing background component is not fully proportional to the volume, but increases closer to the MS walls as expected from Rydberg induced events. In contrast to this significant change is the distribution of stored particle induced rate. Here no change is observed from 2017 to 2019. This confirms a constant radon-induced background rate, without time dependence. Given that the Rydberg induced background is not only the dominant origin of the elevated background rate, but also induces a

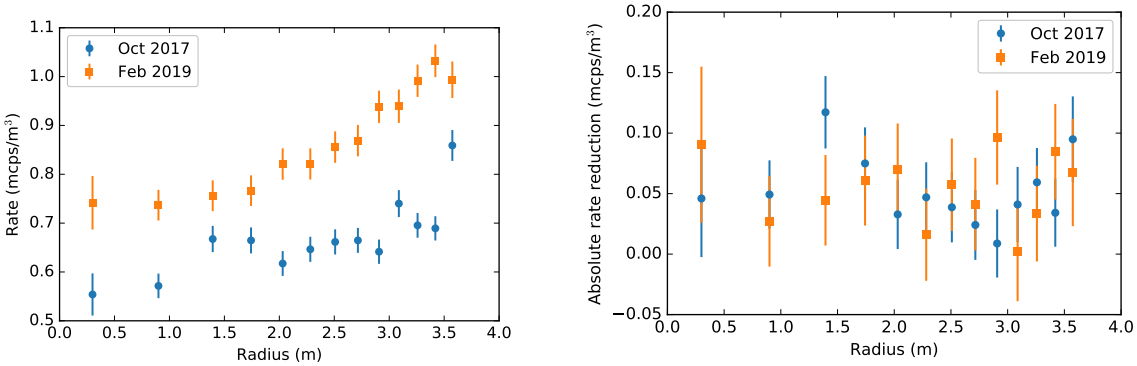

(a) background rate

(b) Stored particle induced fraction

Figure 4.18: Radial distribution of the overall background rate (a) in October 2017 and February 2019. The rates are normalized to the flux volume and shown as a function of MS radius. Each data point corresponds to the rate of one FPD ring. (b) shows the absolute contribution of stored electrons to the overall background rate.

significant time dependency, its mitigation is essential. To get experimental evidence of the background model, specific measurements are carried out that are discussed in chapter 5.

5 Characterization of Radon and Rydberg induced background

To reduce the background a precise understanding of the prevailing background source is essential. Within [73] a detailed model was worked out allowing key characteristics to be reproduced. Dedicated measurements are performed, which target two of the outstanding characteristics of this background mechanism, namely the created very low energetic electrons and the IE dependency. The first is investigated by a measurement of the background electrons energy spectrum described in section 5.1. The second is studied by means of an artificial Rydberg background source described in section 5.2. Up to now the background's vessel voltage dependency eludes all models. To investigate potential creation mechanisms special measurements are carried out. They are described within section 5.3

5.1 Determination of background electron energy spectra

Electrons created by thermal ionization of highly excited Rydberg states have energies less than 100 meV. Their mean energies are expected to be in the order of 15 meV. This offers a possibility to test the Rydberg hypothesis by a measurement of the background electrons energy spectrum. Two complementary methods are applied for this investigation, both based on selective electron trapping. If background electrons with specific energies are trapped, and assuming that they can not escape the trap, they are no longer detected. Therefore their amount can be estimated through rate variation. In KATRIN there are two options to create configurable traps. On the one hand particles can be trapped electrically in a Penning trap. On the other hand they can be magnetically trapped. In the latter case the magnetic bottle property of the MS is exploited. Subsequently both principles (section 5.1.1) together with their experimental realization (section 5.1.2) are presented. Measurement results of the two methods are discussed in sections 5.1.4 and 5.1.5. The analyzed FPD runs are listed in appendix A.4.

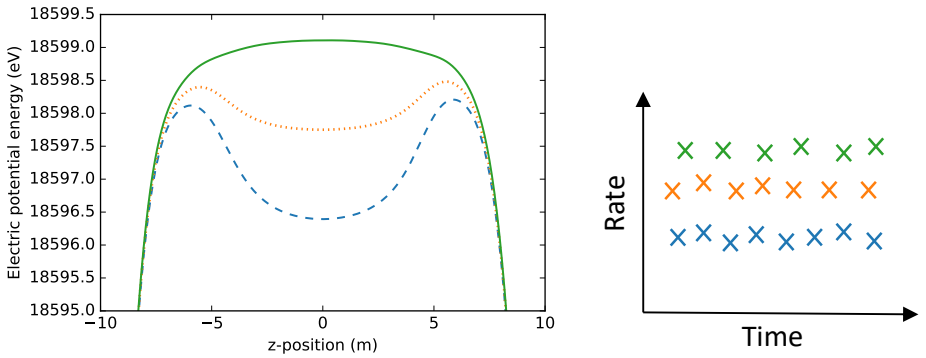

(a) Penning trap in MS center (b) Expected background rate

Figure 5.1: (a) Electric field in the MS at normal settings (green) and with an artificially created Penning trap (orange dotted and blue dashed) in the center. (b) Observed rate depending on the measurement configuration. If electrons become trapped, a reduced rate is observed. The amount of reduction depends on the electron's energies and the dimensions of the created Penning trap.

5.1.1 Concept of electric and magnetic trapping for energy identification

Electric trapping

To trap electrons based on their energy an artificial Penning trap is created in the center of the **m**ain **s**pectrometer. The motion of electrons within the spectrometer is constrained by the guiding magnetic field lines. A Penning trap can be created by a modification of electric potential. This is illustrated in fig. 5.1(a). In normal measurement configuration, the potential over the spectrometer is shaped like the green curve for optimal transmission conditions. Through a small positive offset voltage in the center a symmetric Penning trap can be created. Depending on the strength of this offset a shallow (orange dotted) or deeper (blue dashed) trap is created. In the first case the trap has a depth of about 1 eV. Background electrons with low enough energies become trapped between the two electric potential maxima. Neglecting scattering processes a reduced background rate relative to normal settings (green) will be observed reflecting the amount of trapped background electrons, as visualized in fig. 5.1(b). If not all electrons are trapped already a further rate reduction happens for a deeper trap. By scanning through different trap depths an energy spectrum of the background electrons can be determined based on the observed rate reduction. As electrons can leave the trap via changing their angle through scattering, the expected rate reduction would require complicated scattering

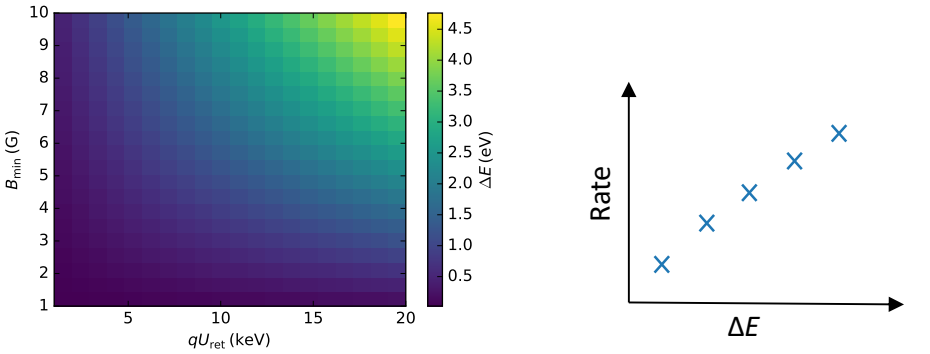

(a) MS energy resolution (b) Expected background rate

Figure 5.2: (a) Energy resolution of the MS for maximal field of $B_{\text{max}} = 4.2\,\text{T}$ depending on the applied retarding potential and the minimal magnetic field. (b) Observed rate depending on the energy resolution. If there are electrons with transversal energies higher than the energy resolution they become trapped and lead to a reduced background rate.

simulations. To avoid this difficulty, the trapped electrons can be removed. In KATRIN this can be achieved by applying an electric dipole pulse (section 4.1.2) every few seconds, which directs stored particles towards the walls by an $E \times B$ drift. That way angular changes can be neglected in the analysis. Given that the (radial dependent) trap dimensions as well as the angular distribution need to be taken into account an energy spectrum can only be obtained through simulations. For analysis detailed MC simulations with Kassiopeia (see section 3.3) are carried out, described within section 5.1.4.

Background electrons with energies $\mathcal{O}(\text{meV})$, as expected from the ionization of Rydberg atoms by BBR, would be trapped already at very small Penning trap depths. Hence for such electrons a significant rate reduction is anticipated for very small voltage offsets $U < 1\,\text{V}$. For larger trap sizes the rate is expected to stay constant. As will be seen in section 5.1.4, the results show a change in background rate for larger trap depths pointing towards a significant fraction of electrons with higher energies.

Magnetic Trapping

The KATRIN MS with its high magnetic fields on both ends forms a magnetic bottle. Charged particles with

$$E_{\perp} > \frac{B_{\text{min}}}{B_{\text{max}}} \cdot qU_{\text{ret}} = \Delta E \tag{5.1}$$

are trapped in the spectrometer volume until they no longer fulfill this trapping condition. After (multiple) scattering(s) and involved angular change(s), every electron can escape the magnetic trap. With varying energy resolution, electrons of different transversal energies are stored. This energy dependency can be used to extract information on the electron energy distribution. Preventing scattering, for instance by removal of trapped electrons, the amount of stored electrons can be observed as background rate reduction. The energy resolution, for retarding energies from 1 to 20 keV and minimal magnetic fields from 1 to 10 G, is shown in fig. 5.2(a) for a maximal magnetic field of 4.2 T. Measuring from large energy resolution towards smaller ones, a reduction of background rate is observed as long as there are additional electrons with $E_\perp > \Delta E$, like illustrated in fig. 5.2(b). Similar to electric trapping, stored electrons are removed and thus scattering is prevented by applying an electric dipole pulse on a regular basis.

In comparison to electric trapping, the magnetic trapping is a complementary approach. With a Penning trap electrons with energies lower than a certain energy are trapped and analyzed. In contrast magnetic trapping is sensitive to all electrons with energies higher than a certain threshold. Electrons created through thermal radiation of Rydberg atoms have total electron energies below 100 meV with mean energies in the order of 10 to 30 meV. Those electrons are not expected to be trapped in any of the $U_{\text{ret}}/B_{\text{min}}$ configurations shown in fig. 5.2(a). Therefore no change in background rate is anticipated for Rydberg induced electrons. However, it will be seen in section 5.1.5, a change is observed pointing towards electrons with larger energies. In principle the measurement can be extended towards lower energy resolutions by even lower retarding potentials or magnetic fields. The current high voltage setup is designed for high precision predominantly close to the tritium endpoint of about 18.6 keV. Towards very low voltages high voltage fluctuations relative to the applied retarding potential become more prominent. Lower magnetic fields would require a larger spectrometer diameter.

5.1.2 Measurement configuration and analysis cuts

Both approaches for background electron energy determination (section 5.1.1) are realized during SDS-III. In this phase the transport section and SDS are separated by a closed valve. The spectrometers are at their nominal pressure in the order of 10^{-11} mbar. For investigation of the dominant MS background the PS voltage is ramped to $U_{\text{PS}} = 0$ V such that created electrons therein are not guided towards the MS. This also simplifies the analysis, since the PS can be neglected in the simulations. Due to maintenance work the PS1 magnet (between PS and transport section) is switched off. If not stated otherwise the PS2 magnet (between PS and

MS) and the Pinch magnet (exit of MS towards FPD) are at the same magnetic field of $B_{\mathrm{PS2}} = B_{\mathrm{Pinch}} = 4.2\,\mathrm{T}$. This is not the standard operation mode for neutrino mass measurement, where the PS2 is at a lower magnetic field than the Pinch magnet. But to prevent more background electrons leaving the MS towards the PS compared to the FPD, both magnets are driven at same field. Compared to the KATRIN design, all magnets run at 70 % of their maximum field to reduce stress. The configuration of high voltage and magnetic field within the spectrometer is outlined in the following.

5.1.2.1 Analyzing plane magnetic field

The analyzing plane magnetic field ($B_{\mathrm{ana}} = B_{\mathrm{min}}$) determines the flux volume and the energy resolution. For different magnetic trapping conditions three magnetic field configurations are chosen, displayed in fig. 5.3. The setting with $B_{\mathrm{ana}} = 3.8\,\mathrm{G}$ is a well suited configuration for background investigations due to its large flux tube coming along with high statistics. Even larger magnetic flux tubes, like with $B_{\mathrm{ana}} = 1.9\,\mathrm{G}$, are also possible, but due to collisions with electrodes outer detector rings need to be excluded in the analysis. Nevertheless this field configuration provides a very good energy resolution of 0.84 eV at $qU_{\mathrm{ret}} = 18.6\,\mathrm{keV}$. The third setting has a minimal magnetic field of 9 G, which requires lower retarding potentials for good energy resolution. Only the energy resolution (assuming constant electron energy distribution) determines the magnetic trapping probability. Therefore independently of how this resolution is achieved, e.g. low B_{ana} and high qU_{ret} or low qU_{ret} and high B_{ana}, the same result is expected.

Measurements with an artificially created Penning trap, referred to as electric trapping, are carried out with $B_{\mathrm{ana}} = 3.8\,\mathrm{G}$ for maximal statistics on each detector ring. This is important since the trap size is radially dependent requiring independent analysis for each FPD ring.

5.1.2.2 MS high voltage setup

The retarding potential in the MS is given by $U_{\mathrm{ret}} = U_{\mathrm{vessel}} + U_{\mathrm{IE}}$. Whereas the vessel voltage is applied to the whole spectrometer, the IE system is partitioned allowing precise shaping of the potential (see also fig. 3.3). For the performed measurements the IE system is configured as visualized in fig. 5.4. In addition to a common voltage offset, $U_{\mathrm{IE\ common}}$, applied to all electrodes with respect to U_{vessel}, individual (positive) voltage offsets can be set to each of the colored regions. For magnetic trapping measurements the following voltage settings are applied:

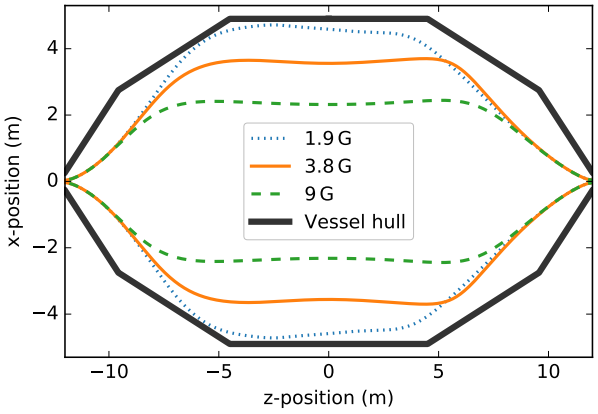

Figure 5.3: Magnetic field lines connecting to the outermost FPD ring for the three different magnetic field configurations. With those three analyzing plane magnetic fields, 1.9, 3.8 and 9 G, different energy resolutions are realized for variable magnetic trapping conditions. Investigations with electric trapping are carried out with $B_{\mathrm{ana}} = 3.8\,\mathrm{G}$.

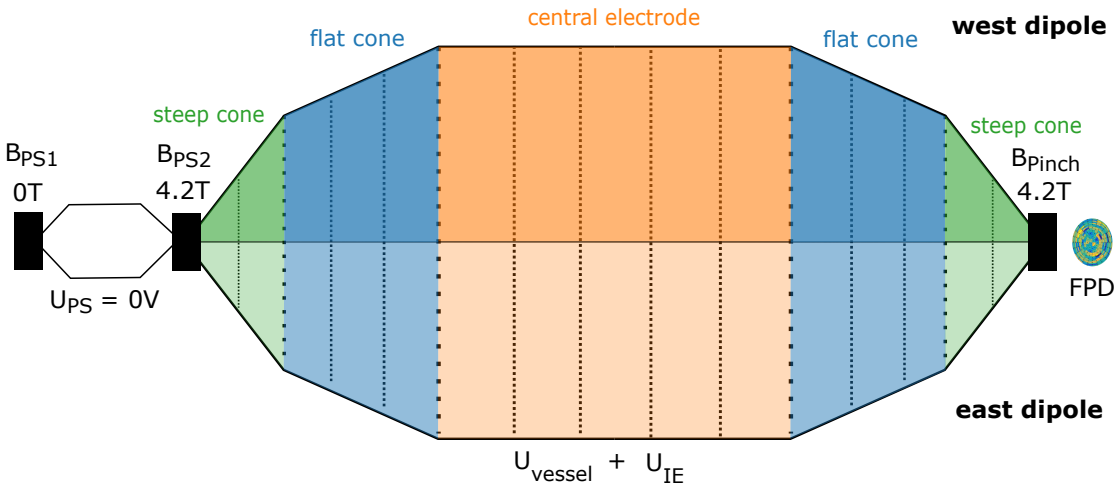

Figure 5.4: Scheme of the high voltage configuration employed for determination of the background electron's energy spectrum. The inner electrode system is connected such that to each colored region a different voltage can be applied.

- PR status: not active
- $U_{\text{vessel}} = -18.5$ to $-0.5\,\text{kV}$
- $U_{\text{IE common}} = -100\,\text{V}$
- $U_{\text{steep cone}} = 97\,\text{V}$
- $U_{\text{flat cone}} = U_{\text{central}} = 0\,\text{V}$
- $U_{\text{dipole west}} = -50\,\text{V}$, pulsed: 1 s on and 4 s off
  for reference background measurements the dipole is switched off.

The vessel voltage is varied to obtain different energy resolutions. At each configuration a reference background measurement without electric dipole pulse is performed. To reduce background from secondary electrons created at the surface the IE is more negative with respect to the vessel. A positive offset voltage of 97 V on the steep cones provides good transmission conditions. Since electrons are only stably trapped without scattering processes, an electric dipole pulse is applied. Every four seconds the west IE partition turns more negative by 50 V for one second. This is sufficient to remove low energetic stored electrons. The PR system (section 3.1) was not available at the time of this measurements and hence not active. However no significant impact of voltage fluctuations is expected. This is confirmed by later performed measurements carried out with post-regulation (see appendix A.6). To create a variable Penning trap in the center of the MS below listed configuration is chosen:

- PR: active
- $U_{\text{vessel}} = -18.5\,\text{kV}$
- $U_{\text{IE common}} = -100\,\text{V}$
- $U_{\text{steep cone}} = 10\,\text{V}$
- $U_{\text{central}} = 0$ to $6\,\text{V}$
- $U_{\text{flat cone}} = 0\,\text{V}$
- $U_{\text{dipole west}} = -50\,\text{V}$, pulsed: 1 s on and 4 s off.

As a reference a measurement without central offset, hence without Penning trap, is performed. For different Penning trap depths the central electrode offsets are varied in a range from 0.3 to 6 V. Compared to the magnetic trapping configuration, the steep cone voltage offsets are less positive. To create a central Penning trap with more positive steep cones requires individual voltages on each of the flat cone rings.

However due to shorts this is not possible for the flat cone on the PS side, resulting in the presented configuration.

5.1.2.3 Analysis cuts

Presented background rates are calculated with a ROI cut of $E_{\text{signal}} \pm 3\,\text{keV}$. This is the standard cut applied for measurements in the SDS. The expected electron/signal energy is given by $qU_{\text{ret}} + qU_{\text{PAE}} + qU_{\text{bias}}$ as described in section 4.3. In presented measurements the PAE is at its standard value of $U_{\text{PAE}} = 10\,\text{kV}$. Depending on analyzing plane magnetic field and applied high voltage some pixels are excluded from the analysis. In case of the 1.9 G configuration the field lines connecting to the outer detector rings collide with the walls, hence only detector rings 0 to 8 are considered. At vessel voltages $U_{\text{vessel}} \geq -2\,\text{kV}$ four pixels with highly elevated rate appear. Those pixels are excluded in the analysis and the rates are scaled to the number of active pixels by 148/144 in case of the whole detector and by 40/36 for the innermost FPD rings (rings 0 to 4). In measurements with pulsed electric dipole, the rate after application of the dipole field is analyzed. Information on the dipole status is saved together with FPD data.

5.1.3 Comparison to previous results with electric dipole pulse

The electric dipole pulse was used in previous works to detect stored particles in the spectrometer, in particular to determine the residual radon-induced background rate. Latest results were obtained within [51], where a rate reduction of (34.0 ± 10.4) mcps was observed at a reference background rate of (530.0 ± 8.6) mcps at a retarding potential of $U_{\text{ret}} = -18.6\,\text{kV}$ and analyzing plane magnetic field of 3.8 G ($\Delta E = 1.68\,\text{eV}$). This is well in agreement with previous results based on a different method, that determined a residual radon-induced background rate of 36^{+18}_{-16} mcps [64]. Those measurements were carried out before the spectrometer bake-out in 2017. As a reference for the radon-induced background fraction and as reproducibility test, this measurement is repeated. Without electric dipole pulse the background rate is (410.61 ± 4.55) mcps (reference background). Due to the baking, the overall background rate is reduced compared to earlier investigations. With application of the pulse a rate reduction is observed as shown in fig. 5.5. At $t = 0\,\text{s}$ an electric dipole field is induced for one second. From $t = 1\,\text{s}$ to $t = 5\,\text{s}$ the field is switched off. This sequence is repeated many times and the events are stacked based on the time after the last dipole pulse. During the dipole pulse not only stored electrons are removed but electrons outside the flux tube e.g. close to the walls are also deflected into the sensitive volume. Therefore the rate in

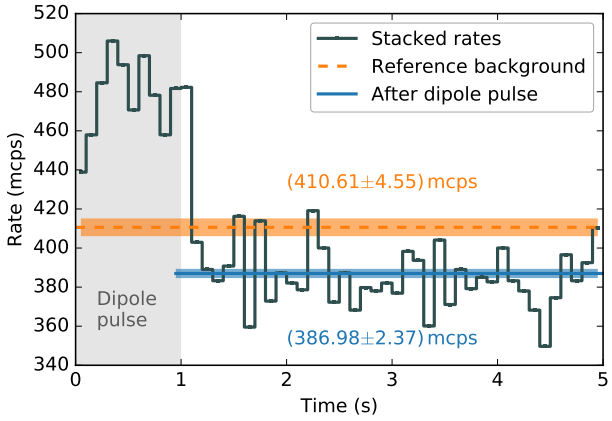

Figure 5.5: Stacked rates during (0 to 1 s) and after application of an electric dipole pulse (1 to 5 s). The orange line shows the background rate without dipole sequence (reference). When stored particles are removed by the dipole pulse a reduced rate is observed (blue) compared to the reference.

this time range can be highly elevated. After the dipole pulse, stored particles are removed and a reduced background rate with respect to the reference background is observed. Here a rate of (386.96 ± 2.37) mcps is detected. Compared to the reference background, this corresponds to a rate reduction and hence stored particle induced background of (23.63 ± 5.13) mcps. This is in agreement with the results obtained in [51] indicating unchanged radon-induced background rate. After the dipole pulse no relaxation of background rate is observed, hence application of a -50 V dipole voltage every 4 s is sufficient for stored particle removal. This is confirmed by separate measurements with an increased time of nearly 5 min between the dipole pulses, see appendix A.5.

5.1.4 Results based on electric trapping

With electric trapping the background electron energies are studied. The observed rates after removal of stored particles for the different positive central voltage offsets, which are approximately proportional to the Penning trap size, are shown in fig. 5.6 for four FPD rings. Through the different flux volumes imaged on the individual detector rings, the overall background rates differ. Especially for ring 0, the bulls-eye, this is noticeable. For voltage offsets $U < 2$ V the rate significantly drops on all rings, indicating presence of stored electrons. For voltage offsets $U > 2$ V the decrease is less significant and the rate starts to saturate to a constant level. One constituent of this constant residual background rate are electrons created between the Penning trap and the spectrometer exit. Since the trapping conditions depend

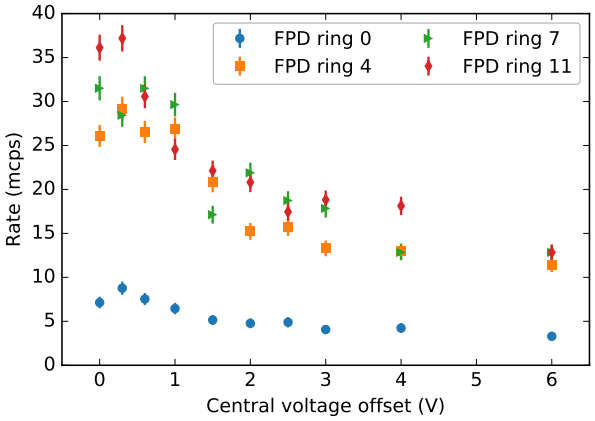

Figure 5.6: Background rate after removal of stored particles for four detector rings. The central voltage offset reflects the Penning trap configurations. With higher voltages, a deeper trap is created.

on the size of the Penning trap as well as the angular distribution of the electrons, this measurement can only be clearly interpreted by means of simulations, described in the following.

Through comparison of simulated events of known energy to measured ones, information on the background electron energies is obtained. Simulations are performed with the software Kassiopeia (see section 3.3). Based on the Rydberg background model, generated electrons are expected to be isotropically distributed. Additionally they are approximately homogeneously spread over the spectrometer volume. For discrete energies $N = 10\,000$ electrons are generated, distributed accordingly within the flux tube volume. The energies 0.01, 0.1, 0.2, 0.4, 1, 1.2, 1.6 and 2 eV are chosen based on the Rydberg expectation and the observed rates at the individual voltage offsets. Since a large rate change is observed up to a voltage offset of $U = 2\,\mathrm{V}$ trapped electrons with energies up to 2 eV are considered. Scattering of electrons with residual gas can be neglected as it is prevented in the measurement by the electric dipole pulse. Hence electrons that become trapped can not escape the trap and will not be detected. In the simulation electrons are terminated

- when leaving the spectrometer towards the PS
- after becoming trapped
- when hitting the detector.

This simulation is performed for each potential setting. Electric fields are calculated by means of equivalent potentials [51] to enable an accurate and at the same time fast calculation. Accuracy is of special importance in this case since already small

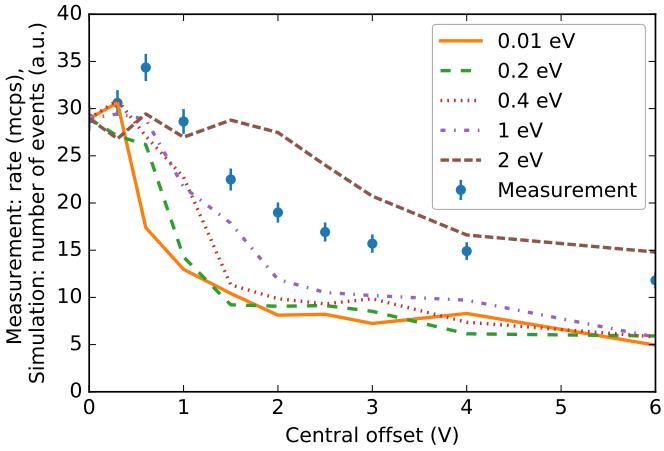

Figure 5.7: Measured background rate and simulated events as a function of central voltage offset for one FPD ring. Each line shows simulated events for a specific electron energy. For visualization they are normalized to the measurement rate without central offset.

distortions in the fields, created by for instance the IE holding structures, impact the shape of the Penning trap and hence the storing conditions. From this simulation the number of detected events on the individual FPD rings is retrieved for each setting. This number is proportional to the amount of not trapped electrons. Figure 5.7 shows the measurement result for one ring and the simulated number of events for selected electron energies. For easier comparison the later ones are normalized to the measured rate without central offset applied. Very low energetic electrons, e.g. with $E = 0.01\,\mathrm{eV}$, are trapped already in small Penning traps corresponding to small central voltage offsets. Therefore the number of detected events in the simulation decreases promptly, much faster than observed in the measurement. For higher energetic electrons a larger trap depth is needed to trap a significant amount of electrons, hence the reduction of rate shifts to larger voltage offsets. A qualitative comparison of measurement and simulation points towards a fraction of background electrons with energies $\mathcal{O}(\mathrm{eV})$.

The real background electrons do not have a single energy but follow a distribution. Therefore the superposition of different energy simulations needs to be compared to the measurement instead of the individual ones. For a quantitative analysis a fit is performed. Measured rates R_i at the different trap configurations of each detector ring i are described by the superposition of the simulations with discrete energies $N_{\mathrm{sim},i,E}$ such that

$$R_i = c_i + \sum_E p_E \cdot N_{\mathrm{sim},i,E}, \tag{5.2}$$

Table 5.1: Parameters obtained from fitting eq. (5.2) to the measurement data. The parameters p_E are normalized such that they sum up to one and reflect the relative contributions of the individual energies. All other parameters are constant rate offsets, one for each FPD ring. They reflect background originating from higher energetic electrons that are not trapped in the chosen configurations.

parameter	value	parameter	value	parameter	value
$p_{0.01\,\mathrm{eV}}$	0	c_0	0.10 mcps	c_8	7.17 mcps
$p_{0.1\,\mathrm{eV}}$	0	c_1	1.35 mcps	c_9	7.62 mcps
$p_{0.2\,\mathrm{eV}}$	0.08	c_2	0.98 mcps	c_{10}	6.98 mcps
$p_{0.4\,\mathrm{eV}}$	0.21	c_3	3.69 mcps	c_{11}	9.31 mcps
$p_{1\,\mathrm{eV}}$	0.41	c_4	2.61 mcps	c_{12}	6.83 mcps
$p_{1.2\,\mathrm{eV}}$	0.07	c_5	5.73 mcps		
$p_{1.6\,\mathrm{eV}}$	0.06	c_6	5.61 mcps		
$p_{2\,\mathrm{eV}}$	0.25	c_7	6.78 mcps		

where c_i denotes the constant background offset per detector ring, comprising higher energetic stored particles like those from radon. The sum goes over the simulated events $N_{\mathrm{sim},i,E}$ of the individual energies E for each ring i weighted by the factor p_E, reflecting the contribution of energy E to the measurement data. The weighting factor p_E displays the relative fraction of the energies. In total 13 constant offsets c_i are fitted (one for each detector ring) as well as 8 parameters (one for each simulated energy) simultaneously to the data of all detector rings. This analysis assumes no radial dependence of the background electron energies. The fit results for the individual detector rings are shown in fig. 5.8. Fitted parameters are listed in table 5.1.

For all rings the measurement can be well described by the fitted superposition of simulations. Due to the large fluctuations in rate, deviations from the fitted model higher than the shown statistical uncertainty occur. The uncertainty due to the finite sample size in the simulation can be neglected. An increased measurement time together with more data points in the most sensitive region, below central voltage offsets of 2 V, could improve the agreement. Nevertheless a $\chi^2/\mathrm{ndof} = 3.35$ (ndof = 109) can be achieved with the current data set. The fitted constant offsets for each detector ring increase with ring number, analogous to the background rate, because of different flux volumes being projected on the detector rings. The factors p_E directly provide the background electron's energy distribution. Since their absolute value depends on the total number of simulated events, they are normalized such that $\sum_E p_E = 1$. The resulting energy spectrum is shown in fig. 5.9. Only energies

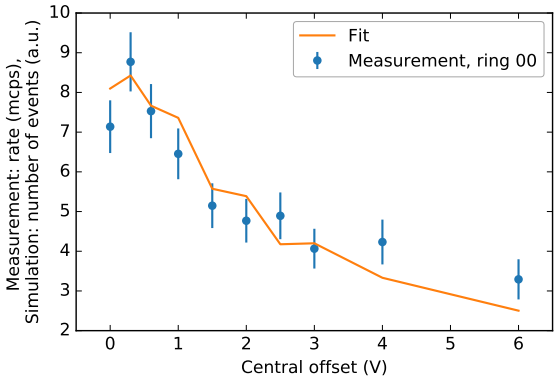

(a) Ring 0

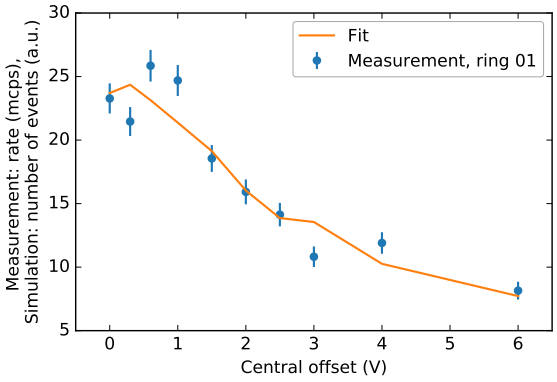

(b) Ring 1

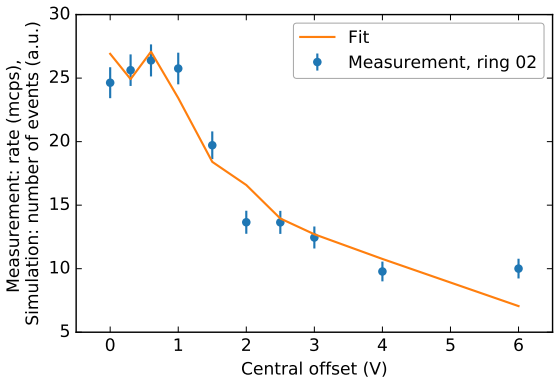

(c) Ring 2

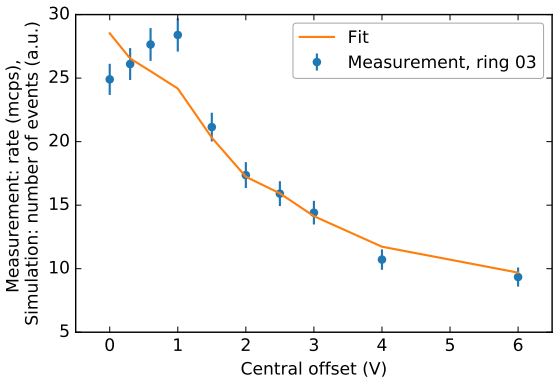

(d) Ring 3

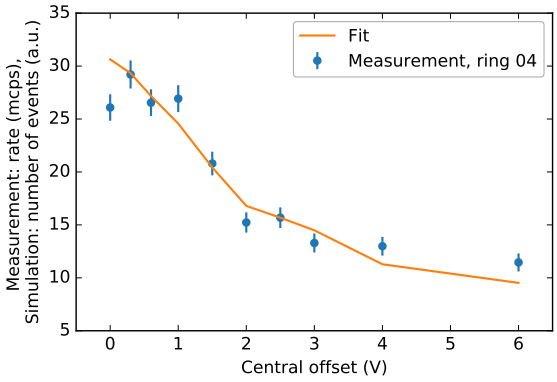

(e) Ring 4

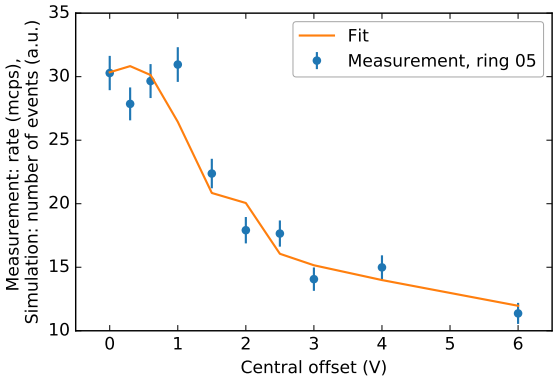

(f) Ring 5

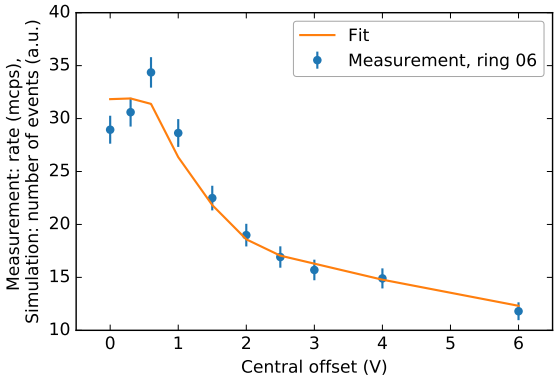

(g) Ring 6

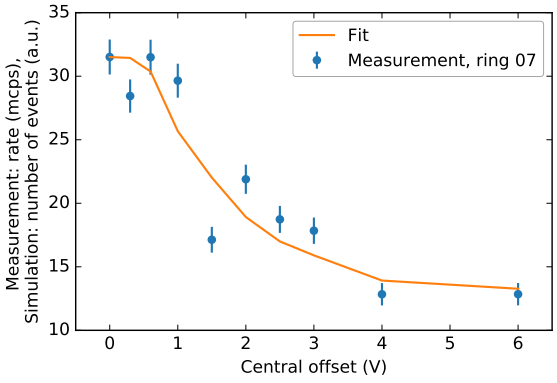

(h) Ring 7

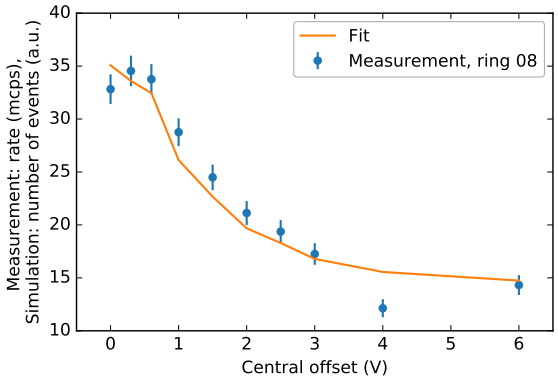

(i) Ring 8

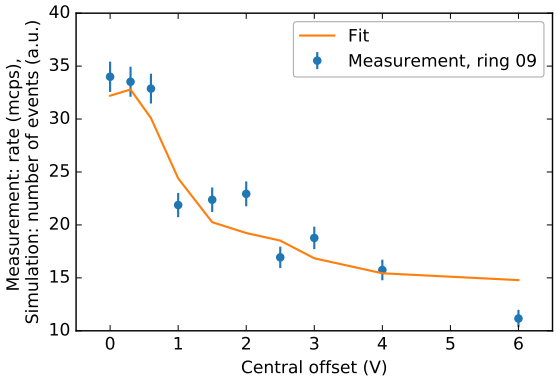

(j) Ring 9

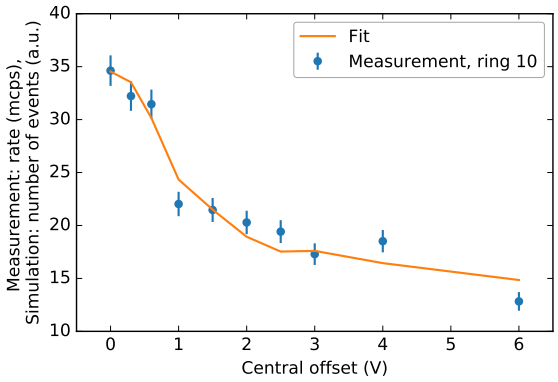

(k) Ring 10

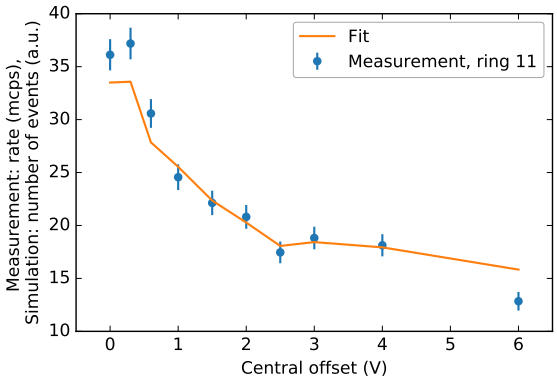

(l) Ring 11

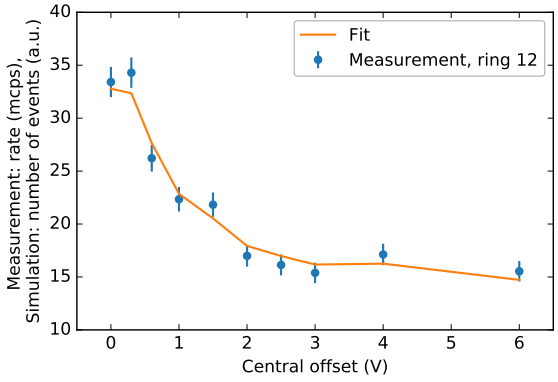

(m) Ring 12

Figure 5.8: Fit of eq. (5.2) to the measurement of each FPD ring. The simulation is able to describe the measurement. Due to the large rate fluctuations, deviations beyond statistical uncertainties remain. With the electron energies 0.01 to 2 eV a $\chi^2/_{\mathrm{ndof}} = 3.35$ is obtained.

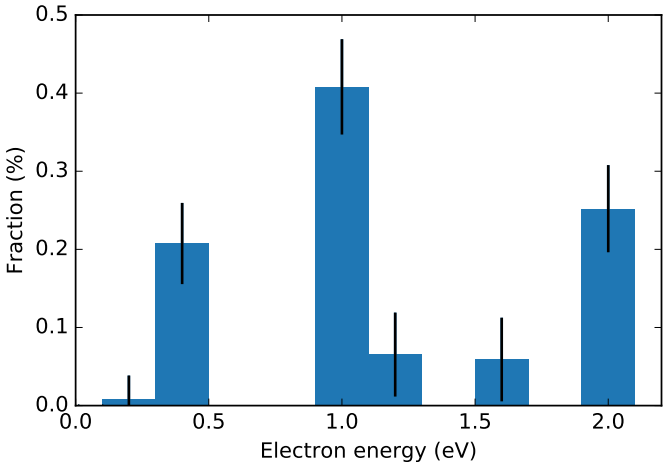

Figure 5.9: Electron energy spectrum obtained from fitting the simulation, eq. (5.2), to the measurement data. The fractions are normalized such that their sum is one. Error bars are obtained from MC.

$E \geq 0.2\,\mathrm{eV}$ have non-zero contributions. To estimate an error on the individual factors a Monte Carlo study is performed, where the data points are randomized based on their uncertainty and the fit is repeated. For each fit parameter a distribution is obtained, whose width reflects the statistical uncertainty. Based on this study, a large fraction of background electrons seems to have energies larger than 200 meV. Such high background electron energies are not expected from thermal ionization of Rydberg atoms. To exclude correlations between high energetic contributions and ring-wise offsets as origin, the goodness of fit χ^2/ndof is evaluated for low energies only. For this the measurement is fitted not with the superposition of all energies 0.01 to 2 eV but only with energies up to 0.1 eV and up to 1 eV.

- $E \leq 0.1\,\mathrm{eV}$: $\chi^2/\mathrm{ndof} = 11.3$ (ndof = 115)
- $E \leq 1\,\mathrm{eV}$: $\chi^2/\mathrm{ndof} = 3.6$ (ndof = 112)
- $E \leq 2\,\mathrm{eV}$: $\chi^2/\mathrm{ndof} = 3.4$ (ndof = 109)

Allowing only the lowest energies gives a significantly worse goodness of fit and is hence not sufficient to describe the measurement. Energies up to 1 eV improve the result by far. The only non-zero contributions in this case are 0.4 eV and 1 eV with the fractions 0.16 and 0.84, respectively. Hence higher energies are clearly preferred to describe the measured data. Best agreement between measurement and simulation is obtained for the full energy range up to 2 eV. In conclusion, this measurement points towards a high proportion of background electrons with energies larger than the expected $\mathcal{O}(10\,\mathrm{meV})$ from the Rydberg background model. Especially dominant are the energies $E = 0.4\,\mathrm{eV}$, 1 eV and 2 eV.

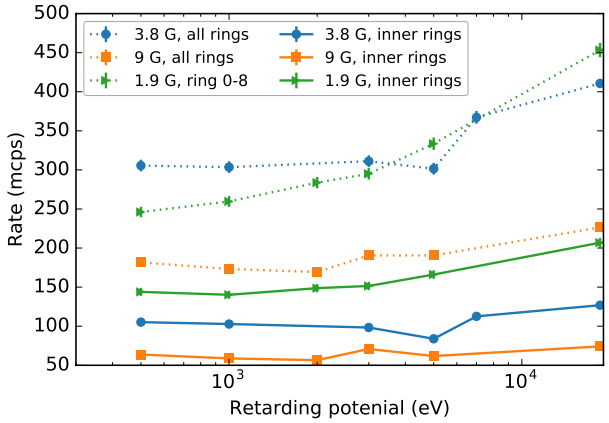

Figure 5.10: Background rate in dependence of the retarding potential for three analyzing plane magnetic fields. Over the whole detector there is a strong relation between rate and voltage. Analyzing only the innermost detector rings this behavior is still present but less pronounced.

5.1.5 Results based on magnetic trapping

In addition to electric trapping, the background electron energies are investigated by means of magnetic trapping. For that the amount of stored particles at the energy resolutions 0.05 to 1.68 eV is evaluated. In case of electrons created by thermal ionization of Rydberg atoms no significant fraction of stored electrons is expected for all of these configurations. Hence after removal of stored electrons by the electric dipole pulse predominantly the residual radon-induced background detectable already with $\Delta E = 1.68\,\text{eV}$ should be observed. For this measurement a large retarding potential range is scanned, wherein the background rate is not constant. Figure 5.10 shows the background rate as a function of retarding potential for the three employed analyzing plane magnetic fields. Due to the different flux tube volumes imaged onto the detector, the overall rates are different depending on the analyzing plane field. The dotted lines show the rates of the whole flux tube imaged onto the detector whereas the solid lines correspond to the inner 4 FPD rings and the bulls-eye (ring 0). Examining the whole detector, a strong dependency on the applied potential is visible. This is enhanced for lower analyzing plane magnetic fields corresponding to larger flux tube radii. The exact origin of this dependency is at the time of this thesis not fully clarified. Dedicated measurements to investigate possible causes are performed within this thesis and are described in section 5.3. Considering only the innermost detector rings, this behavior is less pronounced. To determine the background electron energies the reduced rate after removal of stored electrons relative to the normal background level is evaluated. Since the origin of the retarding potential dependency is not known, interference with background electrons

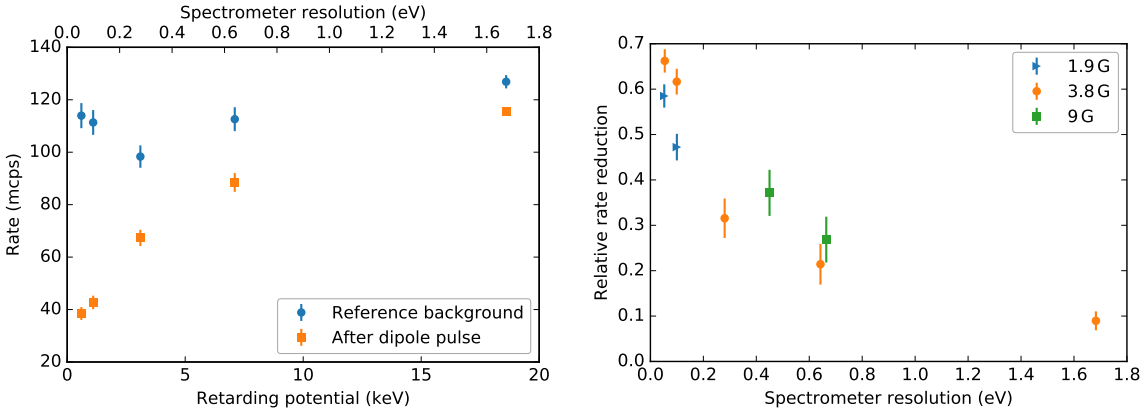

(a) Rate w/o dipole pulse

(b) Relative rate reduction

Figure 5.11: (a) Reference background at $B_{\text{ana}} = 3.8\,\text{G}$ on the innermost pixel rings together with the rate after removal of stored electrons through the pulsed electric dipole. (b) Relative rate reduction by dipole pulse application for different energy resolutions realized by three magnetic field settings.

can not be excluded. Therefore only the innermost detector rings are considered for the analysis to reduce potential impact.

For the analyzing plane field of 3.8 G magnetic trapping measurements are carried out at five retarding potentials. The reference background rates obtained from the innermost detector rings are shown in fig. 5.11(a) (blue). Corresponding energy resolutions of the spectrometer are plotted on the top axis. At each potential the electric dipole pulse is applied. After application of the pulse a reduced background rate is observed (orange). The reduction at $qU_{\text{ret}} = 18.6\,\text{keV}$ represents the residual radon-induced background. Towards lower spectrometer resolutions the rate reduction increases, indicating more trapped electrons. With $\Delta E < 0.2\,\text{eV}$ the background is reduced by the dipole pulse to almost one third of the reference value. This reduction can be expressed as relative rate reduction ΔR_{rel}

$$\Delta R_{\text{rel}} = 1 - \frac{R_{\text{After pulse}}}{R_{\text{ref}}} \tag{5.3}$$

where R_{ref} denotes the reference background rate without application of the dipole sequence and $R_{\text{After pulse}}$ the rate after the electric dipole pulse. The relative rate reduction for all carried out measurement configurations is shown in fig. 5.11(b). Not only with $B_{\text{ana}} = 3.8\,\text{G}$, but also for the other two magnetic field configurations, a strong increase in rate reduction is visible towards smaller spectrometer resolutions. Observed rate reductions at 1.9 G and 3.8 G differ beyond statistical expectations. A possible cause are the different flux radii mapped onto the detector. Whereas the

background rate at 3.8 G shows no radial dependency for the innermost rings, this is not the case for 1.9 G due to the larger flux radius in this configuration. That leads to slight deviations in the relative rate reduction with 1.9 G.

Based on the observed rate reduction and knowing the trapping condition of the spectrometer, a high fraction of stored particles seems to have transversal energies of 0.1 to 1.7 eV. The observed rate reduction at $\Delta E_{\text{max}} = 1.7\,\text{eV}$ further indicates $(9.0 \pm 2.1)\,\%$ of electrons with transversal energies larger than ΔE_{max} in agreement with the residual radon-induced background fraction. This measurement technique can not resolve electron energies lower than $\Delta E_{\text{min}} = 0.05\,\text{eV}$. But the non trapped fraction in the configuration with the smallest energy resolution reflects the amount of electrons having transversal energies less than ΔE_{min}. The two data points with $B_{\text{ana}} = 1.9\,\text{G}$ and 3.8 G and $\Delta E = 0.05\,\text{eV}$ are used for this estimation. Their mean indicates a very low energetic background fraction of $(37.7 \pm 1.8)\,\%$. Based on the two points at around $\Delta E = 0.65\,\text{eV}$ and 0.1 eV the contribution in the intermediate energy range is estimated. This gives the energy distribution

- $E_\perp > 1.7\,\text{eV}$: $(9.0 \pm 2.1)\,\%$
- $0.65\,\text{eV} < E_\perp < 1.7\,\text{eV}$: $(15.1 \pm 4.0)\,\%$
- $0.1\,\text{eV} < E_\perp < 0.66\,\text{eV}$: $(30.3 \pm 3.9)\,\%$
- $0.05\,\text{eV} < E_\perp < 0.1\,\text{eV}$: $(8.0 \pm 2.7)\,\%$
- $E_\perp < 0.05\,\text{eV}$: $(37.7 \pm 1.8)\,\%$.

Since $E_{\text{kin}} \geq E_\perp$ this measurement provides information on the minimal background electron energies. Like the electric trapping measurement this method also points towards a high fraction of electrons with energies larger than $\mathcal{O}(10\,\text{meV})$.

To check whether the magnetic trapping measurement is in agreement with the energies determined by electric trapping a simulation is performed.

Most magnetic trapping measurements are carried out with $B_{\text{ana}} = 3.8\,\text{G}$. At this setting Kassiopeia simulations are performed analogous to those with electric trapping. Electrons are started homogeneously and isotropically distributed within the flux tube with discrete energies. As energies the three dominant fractions determined by electric trapping are chosen: 0.4 eV, 1 eV and 2 eV. Due to application of the electric dipole, stored particles are removed and only the amount of detected electrons is of interest. Therefore scattering processes do not have to be considered. For each measurement configuration 10 000 electrons are generated and the number of detected ones is evaluated. A superposition of simulations is fitted to the rate after the dipole

Table 5.2: Parameters obtained from fitting eq. (5.4) to the measurement data. The parameters p_E are normalized such that they sum up to one and reflect the relative contributions of the individual energies and c the constant offset.

parameter	value
$p_{0.4\,\mathrm{eV}}$	0.38
$p_{1\,\mathrm{eV}}$	0
$p_{2\,\mathrm{eV}}$	0.62
c	35.26 mcps

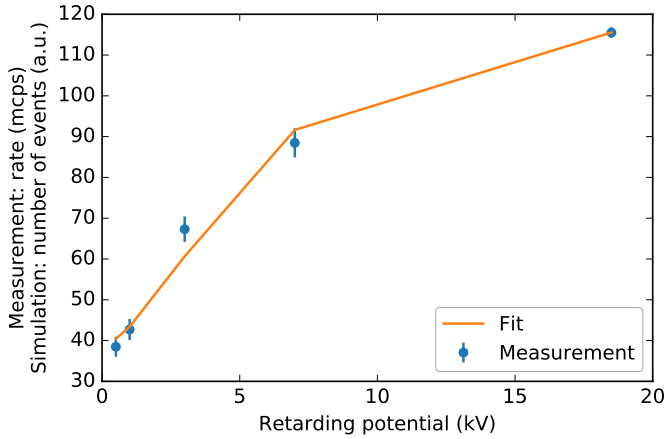

Figure 5.12: Measured rates after removal of stored electrons at $B_{\mathrm{ana}} = 3.8\,\mathrm{G}$. A superposition of simulations (eq. (5.4)) with the energies 0.4 eV, 1 eV and 2 eV is fitted to the data.

pulse, as a function of high voltage. In analogy to the electric trapping, the fit function is given by

$$R(qU) = c + \sum_E p_E N_{\mathrm{sim},E,qU} \tag{5.4}$$

with the constant offset c. The factors p_E correspond to the contributions of the specific energies. The number of simulated events for each energy and retarding energy qU is given by $N_{\mathrm{sim},qU,E}$. Due to the limited amount of measurement points not all energies used in case of electric trapping can be fitted. Figure 5.12 shows the result of this fit. The trend of the measurement can be reproduced by the simulation within statistical uncertainties. Fitted parameters are listed in table 5.2.

5.1.6 Physics interpretation

Two independent measurements of the background electron's energy spectrum point towards a high background fraction with energies that are not in agreement with ionization of Rydberg atoms through BBR. A third method based on partial blocking of electrons was employed in past measurements [98]. The observation therein was similar. Dominant energies of the determined energy spectrum were 0.7 eV and 3 eV. Possible reasons for the observed energies in comparison to the expectation from the Rydberg model are:

- Transmission issues: Low energetic electrons created within the MS are expected to be guided by the magnetic field lines and accelerated by the retarding potential towards the ends of the spectrometer. If this is prevented, for instance by small distortions of the electric potential possibly creating Penning traps or blocking potentials, this changes the interpretation of carried out measurements. Such distortions would be a severe matter, since they could also affect the transmission of signal electrons. It is unlikely though that all measurement methods are affected in the same way. Assuming for instance transmission issues as origin of the background's retarding voltage dependency, the magnetic trapping approach would be highly affected. But measurements at constant retarding potential, like electric trapping, would not be affected. So far investigations of transmission properties, predominantly carried out close to the tritium endpoint, did not point towards any perturbations [99, 100]. Therefore it is unlikely that the electric trapping measurements are disturbed. To exclude problems at low retarding potentials, the transmission would have to be investigated in detail at low retarding potentials.

- Doppler effect: Sputtered atoms are created with kinetic energies of $\mathcal{O}$(keV). Hence the energy of generated electrons can be Doppler shifted. The impact of this is estimated by a MC study. Considering this effect leads to a distribution of electron energies ranging up to 300 meV instead of 100 meV. This is not sufficient to explain the measured electron energies.

- Ionization mechanism: For the Rydberg background very low energetic electrons are expected since ionization through BBR is assumed. However this might not be the only ionization mechanism present in KATRIN. Other processes, like autoionization, are able to generate electrons with energies of multiple electronvolt.

Since transmission issues are unlikely to distort all experimental measurement approaches and the Doppler effect can be excluded other ionization mechanism should be considered. Aside from thermal ionization, field ionization can occur. This was

already mentioned within section 4.1.3. However conditions for this process are only met close to the wire electrodes, such that no background distributed over the whole spectrometer volume can be produced. Other ionization processes were investigated within [78]. The following summary of mechanisms is based on the findings obtained within this work. Major requirements for the ionization process are lifetime and ionization conditions. To generate a homogeneously distributed background, the Rydberg atoms need to live long enough to spread in the spectrometer. This requires a lifetime in the order of 10^{-3} s. In addition the conditions for ionization need to be fulfilled within the volume, not just close to the walls.

Penning ionization

Penning ionization refers to an ionization following the collision of two atoms, where one of them is in an excited state [101].

$$A + B^* \rightarrow e^- + A^+ + B$$

The process is illustrated in fig. 5.13 according to [102]. Atom **A** approaches the excited atom **B***. They are attracted to each other by the van-der-Waals force. As soon as their electron clouds overlap there is a high probability for an electron of atom **A** to jump to a lower energy level of atom **B***. At the same time the excited electron of atom **B*** is emitted and becomes a free electron. The final state consists of the emitted electron, the ionized atom $\mathbf{A}^+$ and atom **B**. This electron balances the energy difference of the excitation potential of the initial state $P(B^*)$ and the ionization potential of the final state $P(A^+)$ and has hence the energy

$$E(e^-) = P(A^+) - P(B^*). \tag{5.5}$$

Emitted electrons can have energies $\mathcal{O}$(eV) [103]. In case of two Rydberg states approaching each other, the electron clouds do not need to overlap because dipole-dipole interaction dominates[1] [104]. When the atoms are close enough one Rydberg atom de-excites to $R(n')$ and the other ionizes [105, 106]:

$$R(n) + R(n) \rightarrow R(n') + e^- + R^+. \tag{5.6}$$

The emitted electron has the energy

$$E(e^-) = E_{\mathrm{Ryd}} \left(\frac{1}{n'^2} - \frac{1}{n^2} \right). \tag{5.7}$$

[1] Rydberg atoms have a large dipole moment because of the large distance between the outer electron and the core

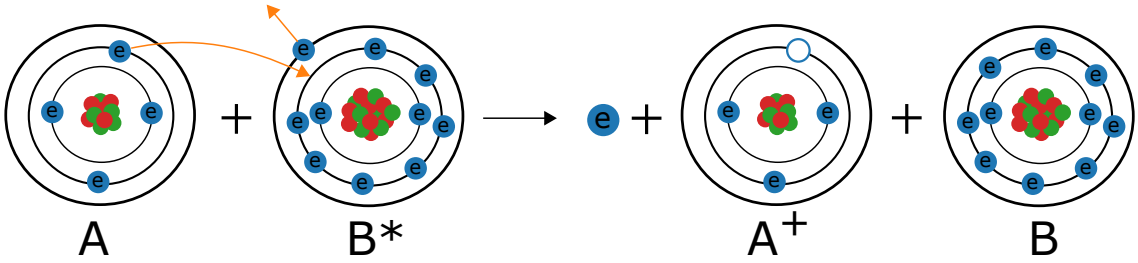

Figure 5.13: Scheme of Penning ionization. An atom collides with an excited atom. When they are close enough to form a quasi molecule, there is a high chance that an electron from atom **A** jumps to a lower energetic level of atom **B***. The excited electron of atom **B*** is emitted in this process, carrying the energy difference of initial and final state.

Penning ionization can potentially generate electrons in the energy range observed in measurements. However this process requires two atoms being close enough to interact. Simulations, where sputtered particles created from the intrinsic MS activity are tracked, show that this is very unlikely inside the spectrometer volume. Close to the surface, where many atoms are sputtered off on a small surface area, Penning ionization is likely to occur. Nevertheless electrons created there do not contribute to the background within the volume.

Autoionization

The term autoionization refers to the spontaneous electron emission of an excited atom or molecule. In Rydberg atoms excited discrete states exist above the ionization limit. The existing discrete and continuum states perturb each other, leading to a mixture of discrete and continuum wave functions [107]. Hence there is a non-zero probability for an electron to traverse into the continuum via the process

$$A^* \rightarrow A^+ + e^-.$$

Depending on the excited atom and its neighborhood different autoionization processes can take place:

1. **Interatomic Coulomb Decay (ICD)** [108, 109] refers to the process schematically illustrated in fig. 5.14. It requires two atoms, labeled here with **A** and **B**. First, one of the atoms, **A**, is excited by for instance photons. This is obviously not possible within the KATRIN MS. But such excitation can also happen by ion or low energetic electron impact [110]. The hole created through excitation is filled by a higher shell electron and the energy difference is emitted in form of an electron. This is the so-called resonant Auger process. The

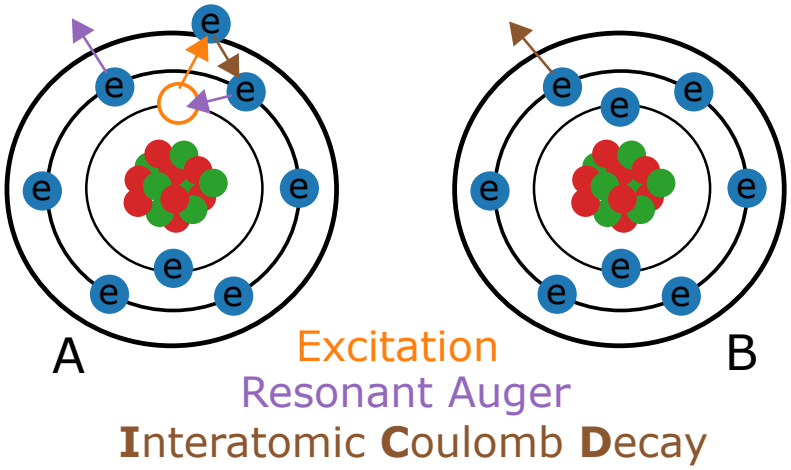

Figure 5.14: Scheme of ICD: After excitation of atom **A**, the created hole is filled by a higher shell electron and the energetic difference is passed to an electron which is released in a resonant Auger process. The subsequent created hole is filled and atom **B** ionized balancing the energy (ICD).

firstly excited electron of atom **A** de-excites and the energy difference leads to ionization of atom **B**. Afterwards the two ionized atoms are pushed apart by Coulomb repulsion. Created electrons through this process have energies $\mathcal{O}$(eV) and would fit the measured background electron energies. Sputtered atoms or molecules created in close proximity to each other at the MS surface can occur in excitation configurations such that ICD can happen. However those states are very short lived, such that there is only a tiny time window $\mathcal{O}(10^{-15}\,\mathrm{s})$ for the process [111]. Based on the velocity of the sputtered atoms, about $1 \cdot 10^{-3}\,\mathrm{s}$ are necessary to distribute the atoms over the MS volume. In addition the probability is low for two atoms being in close proximity to each other within the MS volume. Hence ICD is unlikely the origin of the KATRIN background since atoms are ionized before spreading homogeneously.

2. **Metastable atomic states**: This kind of autoionization does not require a neighboring atom. In case of a molecule the energy for ionization is provided by internal energy such as vibrational or rotational excitations [107]. Since the fraction of sputtered molecules is unclear, atoms are considered in the following. For atoms ionization happens when internal energy prevails the ionization limit. This is an immediate process and hence out of question for KATRIN. However in case of meta-stable states, where spontaneous transition is forbidden by electric dipole selection rules, ionization is delayed resulting in enhanced lifetimes. In case of helium and oxygen lifetimes up to seconds are observed [112]. Oxygen has the highest abundance amongst sputtered particles. However the metastable states in oxygen with sufficient lifetime are

not autoionizing [113]. Existing autoionization states generate electron energies of up to 3 eV, but they have lifetimes in the order of 10^{-15} s. Other sputter products, like chromium or iron, also offer a large variety of autoionizing states [114, 115, 116] enabling electron production $\mathcal{O}$(eV). But like for oxygen their lifetimes are not sufficient to generate a homogeneous background over the MS volume.

3. **Doubly excited atoms** are atoms with at least two excited electrons. Those states are long-lived. They can be differentiated into two types:

   I) No overlap between ground and excited state

   II) Overlap between ground and excited state.

   For the second kind autoionization happens on too short timescales [107] to be a major background inducing candidate. The first type is referred to as planetary atoms since the electron's motion is describable by Kepler orbits and depends only on the core's charge but not on its detailed structure. Those states statistically dominate. They can be produced by scattering of low energetic electrons with atoms or ions [117]:

$$e^- + A^+ \rightarrow A^{**}$$
$$e^- + A \rightarrow A^{**} + e^-.$$

   Both constituents are present in the sputtering process. The excited electrons in planetary atoms are arranged as Rydberg series [118]. When there is energetic overlap those states interfere. In case of destructive interference this leads to enhanced lifetimes of autoionizing states by orders of magnitude. Based on theoretical treatment lifetimes up to 1 s can be obtained [117]. Such lifetimes are more than sufficient for atoms to spread over the MS before decaying. Therefore they can potentially generate a homogeneously distributed background. In principle also atoms of type II can contribute to the background since type I states can decay to type II states. Since this process is a promising candidate further investigations are currently work in progress by D. Hinz [119].

5.1.7 Conclusion

The current elevated background in the spectrometers features characteristics in agreement with highly excited atoms ionized through BBR. In this case background electrons with energies less than 100 meV are expected with a mean energy of about 15 meV. To verify this background generation mechanism the background electron energies are determined by two complementary methods. One approach is based

on electric trapping. Through creation of a Penning trap electrons below a certain energy are trapped and analyzed. By comparison to a simulation an energy spectrum is extracted pointing towards a high fraction of electrons with energies ranging from 0.4 to 2 eV. The second method is based on magnetic electron trapping. It is sensitive to electrons with energies above the MAC-E filter's energy resolution. This measurement provides the following information on low and high energetic contributions:

- $E_\perp > 1.7\,\mathrm{eV}$: $(9.0 \pm 2.1)\,\%$ (residual radon contribution)
- intermediate energies: $(53.4 \pm 6.2)\,\%$
- $E_\perp < 0.05\,\mathrm{eV}$: $(37.7 \pm 1.8)\,\%$.

Since $E_\mathrm{kin} > E_\perp$ those energies are to a large extend higher than expected from thermal ionization. Furthermore the measurement can also be described by the three dominant energies determined from electric trapping. Observed background electron energies from both methods are in the same order of magnitude as determined by previous investigations performed within [98]. Those high energies can not be explained with thermal ionization of Rydberg atoms. Other ionization processes can potentially generate sufficient electron energies. However due to constraints on the lifetime and conditions for ionization only a few come into question. For field and Penning ionization the conditions are only met close to the spectrometer walls. Most autoionizing states do not have sufficient lifetime to generate a homogeneously distributed background. So-called planetary atoms, doubly excited states, are promising because of their extended lifetime. Further investigations are currently work in progress by D. Hinz.

5.2 Verification of Rydberg induced background - ^{223}Ra measurement

The Rydberg background model explains several features of the MS background like radial, temperature and IE dependency. Open questions remain with regard to the exact ionization mechanism and the origin of the Rydberg atoms. The former was investigated within section 5.1. Rydberg atoms are presumably created through α-decays in the vessel walls inducing a sputtering process. Whether such decays can induce background within the spectrometer volume, in particular Rydberg background, is targeted in the subsequently described measurement. Obtained results will be published within [80].

5.2.1 Methodology

In the MS the Rydberg atoms are created following the decay chain of ^{210}Pb:

$$^{210}\mathrm{Pb} \xrightarrow[22.2\,\mathrm{yr}]{\beta} {}^{210}\mathrm{Bi} \xrightarrow[5.01\,\mathrm{d}]{\beta} {}^{210}\mathrm{Po} \xrightarrow[138\,\mathrm{d}]{\alpha} {}^{206}\mathrm{Pb} \tag{5.8}$$

The α-decay of ^{210}Po induces the sputtering process emitting atoms into the spectrometer volume, amongst others in highly excited states. Those atoms are the origin of the Rydberg induced background. To experimentally verify the connection between surface α-decays and spectrometer background a radioactive source is inserted into the MS. For this ^{223}Ra is chosen. Its decay chain is:

$$\begin{aligned} ^{223}\mathrm{Ra} &\xrightarrow[11\,\mathrm{d}]{\alpha} {}^{219}\mathrm{Rn} \xrightarrow[4\,\mathrm{s}]{\alpha} {}^{215}\mathrm{Po} \xrightarrow[1.8\,\mathrm{ms}]{\alpha} {}^{211}\mathrm{Pb} \xrightarrow[36\,\mathrm{min}]{\beta} {}^{211}\mathrm{Bi} \\ &\xrightarrow[2.1\,\mathrm{min}]{\alpha} {}^{207}\mathrm{Th} \xrightarrow[4.8\,\mathrm{min}]{\beta} {}^{207}\mathrm{Pb} \end{aligned} \tag{5.9}$$

It has the advantage of not just one but four α-decays with short lifetimes. Therefore a large amount of Rydberg atoms and hence high background rate is expected to be created through subsequent sputtering processes. In addition all isotopes are short-lived to prevent long term contamination of the MS. After insertion of the source into the spectrometer, the induced background is investigated with respect to its IE dependency, one characteristic of the Rydberg background.

5.2.2 The source

The ^{223}Ra source is produced at the **I**sotope **S**eparator **O**n **L**ine **DE**vice (ISOLDE)[2] [120] facility at CERN. For a low level of contaminants it is created from in-target decay of ^{227}Th. As substrate serves a gold half-sphere with a diameter of 1 cm. Radium is implanted in a depth of about 40 Å. Sufficient purity of the source is confirmed by gamma spectroscopy. Its activity by the time of the performed measurements is roughly estimated based on a dosimeter and a contamination detector. With 0.17 µSv·h^{-1} the activity is in the order of 6 kBq. To insert the source into the MS it is mounted to a steel arm. By a magnetic steering unit the source is moved to spectrometer surface level. The whole apparatus is mounted to a port on top of the MS on the detector side. This way the source can be inserted without breaking the UHV. Once the valve to the source opens, the spectrometer is exposed to the full radium activity. A photo of the complete installed module is shown in fig. 5.15.

[2] https://isolde.web.cern.ch/isolde-facility

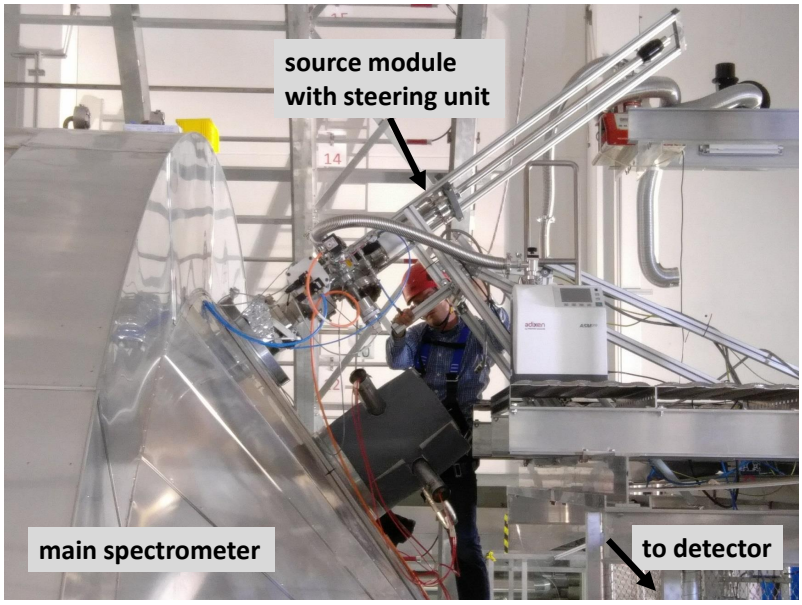

Figure 5.15: Installation of the module at the top side of the MS. The source can be magnetically steered into the spectrometer.

5.2.3 Measurement configuration and analysis cuts

Measurements with the ^{223}Ra source are performed within STS3a. The valve between SDS and transport section remains closed. Superconducting magnets are at 70 % nominal fields corresponding to the neutrino mass measurement configuration

- $B_{\mathrm{PCH}} = 4.2\,\mathrm{T}$
- $B_{\mathrm{PS1}} = 3.1\,\mathrm{T}$
- $B_{\mathrm{PS2}} = 3.1\,\mathrm{T}$.

Two analyzing plane magnetic field configurations are employed. They are illustrated within fig. 5.16. The lines correspond to the 14 magnetic field lines connected to the edges of the FPD rings. Figure 5.16(a) is a symmetric configuration with $B_{\mathrm{ana}} = 3\,\mathrm{G}$. With its maximized flux tube volume high statistics is collected and information on the radial distribution can be obtained. To investigate the induced activity on the surface an asymmetric configuration is employed shown in fig. 5.16(b). Since the PS1 magnet could not be switched off at this time, the magnetic field lines connecting to the innermost rings can not be directed onto the spectrometer walls. None of the field lines connects to the source itself such that electrons emitted directly from the source are not imaged.

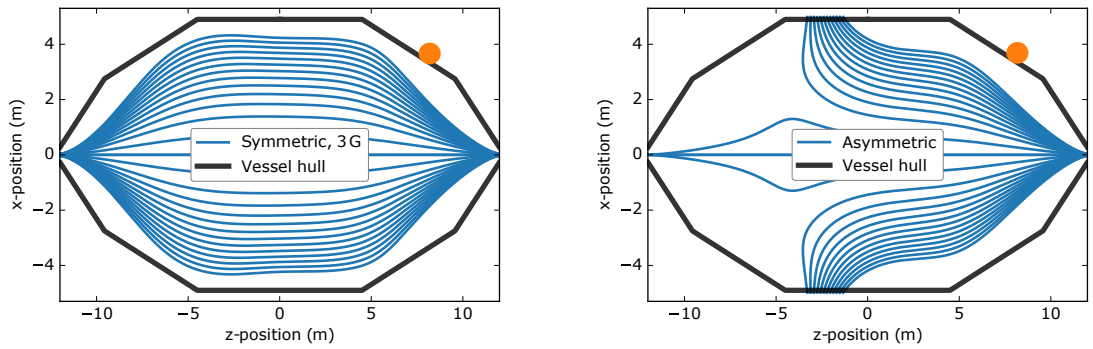

(a) Symmetric

(b) Asymmetric

Figure 5.16: Symmetric (a) and asymmetric (b) magnetic field configuration used for background studies with the artificial background source ^{223}Ra. The orange dot marks the position of the radium source.

For the performed background studies the retarding potential was constant at −18.6 kV with different overall offsets on the IE. The steep cones on the upstream and downstream side are set to $U_{\mathrm{SC}} = 40\,\mathrm{V}$. Within this measurement campaign the standard ROI for such background measurements, with nominal PAE voltage of 10 kV, is a range of 22 to 32 keV. In addition 16 pixels are excluded due to detector effects (4) and misalignment (12).

5.2.4 Experimental results

After introducing the source into the MS the background rate emitted from the surface is monitored with asymmetric magnetic fields. The background within the volume can not be evaluated with inserted source due to the strong radon emanation leading to stored particle induced background in the order of $\mathcal{O}$(kcps). Since the expected Rydberg induced background is a few counts per second (four times higher than the normal MS background) it can not be studied with such high radon background. Therefore it is investigated with withdrawn source and after removal of stored electrons. A special focus of this experimental endeavor lies on the characteristics of the induced background, in particular the IE dependency. Performed measurements together with their results are presented in the following. All FPD run number used for the analysis are listed in appendix A.7.

5.2.4.1 Surface activity

After exposing the MS to the ^{223}Ra source, emitted electrons from the spectrometer surface are monitored in asymmetric magnetic field settings (fig. 5.16(b)). Shortly after opening the valve to the source the measurement is started. A short time delay is caused by technical factors (high voltage clearance and returning to the set values), which takes a few minutes. When exposing the spectrometer to the radioactive source an accumulation of overall surface activity is expected provoked by a sequence of sputtering processes. The background rate as a function of time after insertion of the source is shown in fig. 5.17(a). Without radioactive source the background emitted from the surface is (2418 ± 2) cps, indicated by the green line. When starting the measurement, the rate is already at almost 7 kcps and increasing until saturation around 7.7 kcps. The raise of background rate at the beginning of the measurement indicates accumulation of the radium daughters until transient equilibrium is reached. In this case the time dependency of the accumulated surface activity is given by the Bateman equation [121] which relates the activity of parent and daughter isotope to each other. The maximal activity is reached after the time $t_{\max}$ [122]

$$t_{\max} = \frac{1.44 \cdot T_{\mathrm{P}} T_{\mathrm{D}}}{T_{\mathrm{P}} - T_{\mathrm{D}}} \cdot \ln \frac{T_{\mathrm{P}}}{T_{\mathrm{P}}} \tag{5.10}$$

with the half-lives of parent and daughter isotope T_{P} and T_{D}, respectively. In case of ^{223}Ra the daughters' half-lives are dominated by ^{211}Pb with 36 min. For the other radium daughters, e.g. ^{219}Rn, $t_{\max}$ is reached already after 71 s hence before the presented measurement even started. Maximal activity of ^{211}Pb is expected to be reached after about 5 h. The increase until saturation follows

$$A_{\mathrm{Pb}}(t) = A_{\mathrm{Ra}}(t_0) \cdot \frac{\lambda_{\mathrm{Pb}}}{\lambda_{\mathrm{Pb}} - \lambda_{\mathrm{Ra}}} (e^{-\lambda_{\mathrm{Ra}} t} - e^{\lambda_{\mathrm{Pb}} t}) \cdot BR + A_{\mathrm{Pb}}(t_0) e^{-\lambda_{\mathrm{Pb}} t} \tag{5.11}$$

with the activities, $A_{\mathrm{Ra}}(t_0)$, $A_{\mathrm{Pb}}(t_0)$ at measurement start t_0, and decay rates $\lambda_{\mathrm{Ra}} = 7.02 \cdot 10^{-7}\,\mathrm{s}^{-1}$, $\lambda_{\mathrm{Pb}} = 3.19 \cdot 10^{-4}\,\mathrm{s}^{-1}$ of radium and lead [123, 124]. BR denotes the branching ratio, in this case $BR = 1$. This function is fitted to the observed rate increase, with the free parameter $A_{\mathrm{Ra}}(t_0)$, and provides good agreement. However, the sharp rate increase before start of measurement can not be described by this function. It is presumably attributed to the already saturated radon activity on the surface and to the constant emanation of radon from the source itself. Through the chain of sputtering processes an approximate homogeneous contamination of the surface is expected. The rate distribution amongst the individual detector pixels is shown in fig. 5.17(b). On each pixel the background without radioactive source is subtracted. Pixels excluded from the analysis are shown gray shaded. All pixels, beside the bulls-eye which does not map the spectrometer surface, show a

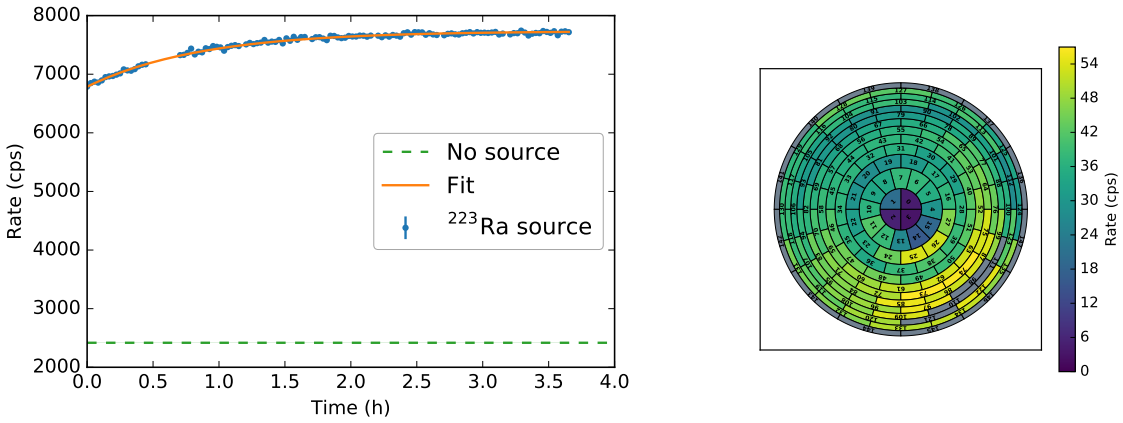

(a) Time evolution

(b) Pixel distribution

Figure 5.17: Rate on the spectrometer surface with inserted ^{223}Ra source. Figure (a) shows the time evolution of the overall rate and (b) the distribution amongst the individual pixels. In the later one the rate without source is subtracted. Gray-shaded pixels are excluded from the analysis.

highly elevated rate. The lower detector half, imaging the spectrometer surface opposite to the source installation, shows a higher rate compared to the upper half indicating a high sputtering occurrence. This inhomogeneous distribution might be attributed to the point like source which is in contrast to the nominal MS surface activity.

5.2.4.2 Background characteristics

Given saturated surface activity induced background in the spectrometer volume is studied. As mentioned previously the source emits radon interfering with potential induced Rydberg background. Hence it can only be investigated with withdrawn source. Prior to a symmetric magnetic field configuration stored particles are removed by either a magnetic pulse or an asymmetric magnetic field setting. Due to the short half-lives of the decay chain, induced background is expected to decay quickly on a time scale dominated by the half-life of ^{211}Pb. To correlate surface activity with potential background within the spectrometer volume, measurements with alternating magnetic field configurations are performed. The sequence, 5 min in asymmetric and 20 min in symmetric settings, is repeated for several hours. This way the electrons emitted at the surface and within the volume are monitored simultaneously. Figure 5.18 shows the results of those measurements, where fig. 5.18(a) refers to the background from the surface and fig. 5.18(b) from the volume. Both show a

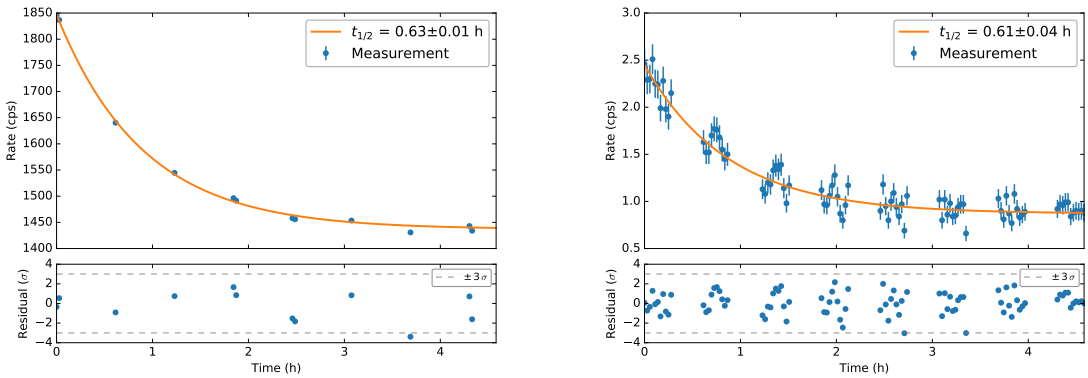

(a) Asymmetric/surface

(b) Symmetric/volume

Figure 5.18: Background rate as a function of time on the spectrometer surface (b) and in the volume (a) with withdrawn source. Prior to this measurement the spectrometer was exposed to the source until transient equilibrium.

clear exponential decay. The data sets are correlated with a correlation coefficient of $\rho = 0.99$[3]. An exponential fit gives the half-lives

- Asymmetric/surface: $T_{\text{surface}} = (0.63 \pm 0.01)\,\text{h} = (37.51 \pm 0.69)\,\text{min}$
- Symmetric/volume: $T_{\text{volume}} = (0.61 \pm 0.04)\,\text{h} = (36.50 \pm 2.54)\,\text{min}$.

Both are well in agreement with each other. In addition the half-lives agree with the literature value of ^{211}Pb with $T_{\text{Pb}} = (36.161 \pm 0.017)\,\text{min}$ [124] within 2σ. This leads to two conclusions:

- Observed background, on the surface as well as in the volume, is induced by ^{223}Ra.
- Surface α-activity induces background in the spectrometer volume. This requires a neutral mediator particle, that transports the electron from the walls into the volume, potentially a highly excited atom.

The background created through the ^{223}Ra source decays with a half-life of 36 min. This gives a short time interval to study this background, before the nominal MS background prevails again. Here the radial as well as the IE dependency is studied.

[3]Computed by binning both data sets into 8 points and under the assumption that they are recorded at the same time

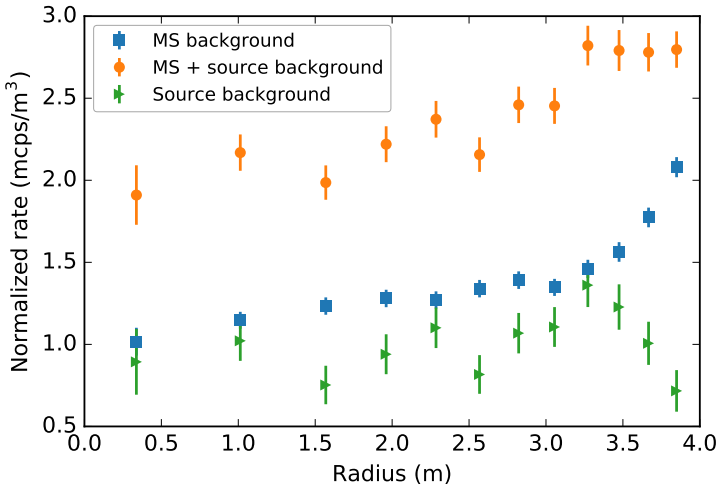

Figure 5.19: Measured rate normalized to the flux volume for the MS background, the observed background with the radium source (on top of the MS background) and their difference corresponding to solely source induced background. They are plotted as a function of MS radius.

Radial distribution

The radial distribution of the α-source induced background within the MS volume is derived from the first three data segments of fig. 5.18(b). Figure 5.19 shows the rate for each FPD ring, normalized to the volume, plotted as a function of spectrometer radius. The blue points correspond to the nominal background without radioactive source (reference). With additional radium induced rate gives the orange trend. Subtracting both gives the radial dependency of the source induced background, shown in green. Until a radius of 3.5 m reference and artificial 'Rydberg' background exhibit a similar trend. Outermost data points run apart. Whereas the MS background increases, the ^{223}Ra induced rate shows no significant radial pattern. Hence the radial profile can not be completely reproduced with the employed α-source. However, previous measurements with a ^{228}Th source could reproduce the radial dependency of the MS background [79]. Therefore it is obvious that this is related to source properties. The ^{223}Ra source is a point-like installation at the MS surface. Unlike the nominal MS background the artificial induced background is not caused by a homogeneous surface contamination (see section 5.2.4.1). This can lead to a different radial pattern.

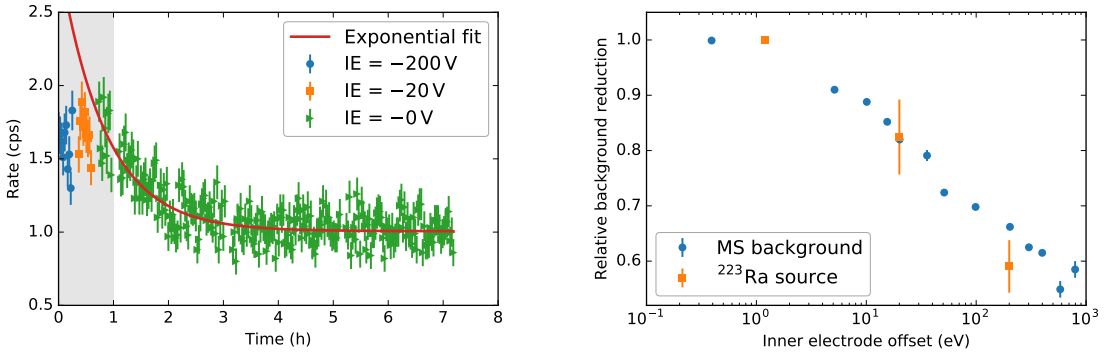

(a) Measurement

(b) IE dependency

Figure 5.20: ^{223}Ra induced background in the spectrometer volume at three different IE voltages. (a): Observed rates in the different potential configurations and the subsequent exponential decay with constant setting. Data used for determination of the IE dependence is shaded grey. (b) Comparison of the determined voltage dependency to nominal MS background, measured within [73].

Dependency on the inner electrode voltage

A key characteristic of the MS background is its dependency on the IE voltage explained within the Rydberg model by field ionization. The α-source induced background is investigated with respect to this behavior. After surface activation the source is withdrawn and stored particles are removed by a magnetic pulse. With symmetric magnetic fields, the IE voltage is switched from $-200\,\mathrm{V}$ to $-20\,\mathrm{V}$ and $0\,\mathrm{V}$. Since the rate decreases exponentially the voltages are set in this order according to the expected background rate. Given limited measurement time due to the exponentially decaying background rate, 18 min are devoted to each setting. Afterwards the measurement is continued with $U_{\mathrm{IE}} = 0\,\mathrm{V}$. The resulting rate as a function of measurement time is shown in fig. 5.20(a). In the first hour source induced background dominates, indicated by the gray shaded area. Here the IE voltages are varied. With constant voltage of $U_{\mathrm{IE}} = 0\,\mathrm{V}$ the exponential decay of ^{211}Pb is observed like in fig. 5.18. The fitted half-life of $(34.83 \pm 3.19)\,\mathrm{min}$ is in agreement with previous results. Extrapolating the fit until measurement start reflects the rate in case of constant voltage. Comparing to the actual observed rates clearly indicates an influence of the IE voltage.

The most accurate measurement of this dependency for the MS background was obtained within [73]. There the background suppression by $U_{\mathrm{IE}} < 0\,\mathrm{V}$ is expressed in terms of relative rate reduction with respect to $U_{\mathrm{IE}} = 0\,\mathrm{V}$. In order to compare the

results with the radium source to those of the MS background, observations from fig. 5.20(a) are converted to the same relative rate reduction. To obtain this quantity the exponential decay as well as the different underlying MS backgrounds need to be considered. From each of the three 18 min data sets the nominal MS background at the respective voltage is subtracted leaving only the radium induced fraction. This gives the number of α-source background events at each voltage, N_{source}, in the respective time interval, listed within table 5.3. To account for the underlying exponential decay, the number of events in each of the time intervals is calculated assuming constant voltage of $U_{\text{IE}} = 0\,\text{V}$ (last time interval). The number of events in the time interval $[t_1, t_2]$ is given by

$$N_{\text{const}} = N_0 \cdot \tau[e^{-t_1/\tau} - e^{-t_2/\tau}]. \tag{5.12}$$

The mean lifetime τ is determined from the exponential fit (see fig. 5.20(a)) to be $\tau = (50.25 \pm 4.61)\,\text{min}$. N_0 is fixed based on the observed events at $U_{\text{IE}} = 0\,\text{V}$, $N_{\text{source}}(U_{\text{IE}} = 0\,\text{eV})$, such that

$$N_0 = N_{\text{source}}(U_{\text{IE}} = 0\,\text{eV}) \cdot [e^{-t_1/\tau} - e^{-t_2/\tau}]^{-1}. \tag{5.13}$$

With eq. (5.12) the expected number of events in the time intervals of the other two IE voltages is retrieved. They are listed in table 5.3 as N_{const} and calculated under the assumption of no voltage dependency. From the ratio between actually observed (N_{source}) and calculated events (N_{const}), the IE voltage dependency is obtained. Comparing the values, more events are expected from the exponential decay than observed at $-200\,\text{V}$ and $-20\,\text{V}$. The ratio

$$\frac{N_{\text{source}}}{N_{\text{const}}}(U_{\text{IE}}) \tag{5.14}$$

gives the relative background change for the different voltage offsets with respect to $U_{\text{IE}} = 0\,\text{eV}$. Figure 5.20(b) shows the computed relative rate reduction in comparison to the one of the MS background. With the artificially induced background by the radium source the same dependency on the IE voltage is observed as for the MS background.

5.2.5 Conclusion

The Rydberg induced background is presumably generated from α-activity at the spectrometer surface. To investigate whether radioactive decays are the background's origin the α-source ^{223}Ra is installed at the spectrometer. Through its four α-decays a high Rydberg induced background rate is expected. Performed measurements show a high correlation between artificially accumulated surface activity and background

Table 5.3: Observed number of events (nominal MS background subtracted) in different voltage configurations (N_{source}). Based on the underlying exponential decay, the expected number of events is calculated assuming no voltage dependency and constant IE voltage of 0 V (N_{const}). The ratio $^{N_{\text{source}}}/_{N_{\text{const}}}$ is the rate reduction relative to $U_{\text{IE}} = 0\,\text{V}$.

U_{IE} (V)	N_{source}	N_{const}	$\frac{N_{\text{source}}}{N_{\text{const}}}$
-200	1079 ± 45	1827 ± 126	0.59 ± 0.05
-20	969 ± 49	1176 ± 77	0.82 ± 0.07
0	755 ± 49	755 ± 49	1.00 ± 0.00

rate within the volume. The radial distribution of the MS background could not be reproduced with this point like source installation. This can be attributed to source properties since past measurements employing ^{228}Th could confirm the radial profile. The nominal background's IE dependency could be successfully reproduced with the ^{223}Ra source induced background. Hence α-activity on the spectrometer surface does not only induce a background within the volume, this background also exhibits the same characteristics as the nominal MS background. This points towards α-decays as a present source of background in the KATRIN MS. Charged particles, like background electrons created at the surface are shielded from the sensitive flux volume. Therefore a neutral mediator is required, like highly excited atoms, that transports the background electron into the spectrometer volume. Therefore this measurement points towards validity of the Rydberg background model. Open questions remain with respect to the exact mechanism of electron creation, since measurements of the background energy spectrum (see section 5.1) show energies that are not in agreement with thermal ionization of highly excited atoms.

5.3 Investigations on the origin of the background's retarding voltage dependence

Towards low retarding energies the background rate continuously decreases (see fig. 5.10). Up to now the origin is unclear. Measurements of the background's voltage dependency with an additional attached radon source show a similar behavior as the MS background [73]. This points towards stored electrons as origin of this behavior. With lower retarding energies a higher fraction of background electrons becomes stored. Based on observations within section 5.1.5, about 10 out of 100 background electrons are trapped at $-18.6\,\text{kV}$ in the MS, whereas at $-1\,\text{kV}$ about 60 out of 100 are stored. It is however not expected that this causes a decrease

in background rate. Stored particles scatter on residual gas, creating secondary electrons. After (multiple) collisions the trapping condition is no longer fulfilled and the primary electron escapes either into the PS or towards the detector. Therefore no drop in background rate is expected with decreasing retarding energy, but more a slight increase since additional secondary electrons are generated. Even if secondary electron creation is neglected, trapped electrons can only provoke the observed high voltage dependency if they are prevented from reaching the FPD by some mechanism. Possible reasons are:

- Electrons preferably leave the MS towards the PS due to transmission characteristics
- Stored particles are removed by a small static dipole caused by non-axial fields or some other unknown effect
- MS transmission properties of low energy electrons.

The first two points are investigated in the following.

In performed measurements the same analysis cuts as described within section 5.1.2.3 are applied. A ROI of $E_{\text{signal}} \pm 3\,\text{keV}$ is set and for potentials $U_{\text{vessel}} \geq -2\,\text{kV}$ four pixels are excluded. Analyzed runs are listed in appendix A.8.

5.3.1 High voltage dependence in different potential configurations

Stored electrons that prefer leaving the MS towards the PS instead of the detector side would cause a background rate that depends on the amount of stored particles. Since a higher fraction of background electrons becomes trapped towards lower retarding energies this would provoke a high voltage dependent background rate. This hypothesis can be tested by investigating the background in different potential configurations. If electrons are blocked towards the PS and forced to leave the spectrometer in direction of the FPD a constant background rate is expected. The efficiency of such blocking can be checked by realizing it on both MS sides such that the background should be maximally suppressed.

An overview of the different potential configurations is given in fig. 5.21. In all cases $B_{\text{PS2}} = B_{\text{Pinch}} = 4.2\,\text{T}$ for equal acceptance angles at both MS exits. Usually the MS potentials are configured for optimal transmission properties. All inner electrodes are more negative with respect to the vessel for electric shielding and both steep cones are set to the same more positive voltage, referred to as symmetric potential setting (see fig. 5.21(a)). This way electrons should have equal chance to exit the

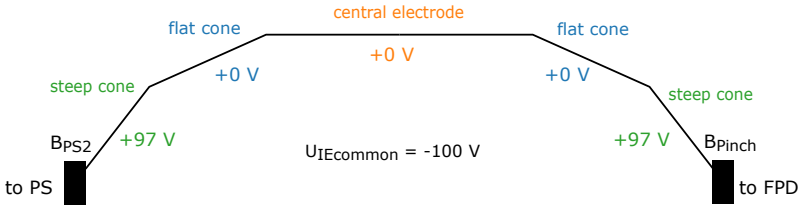

(a) Symmetric potential

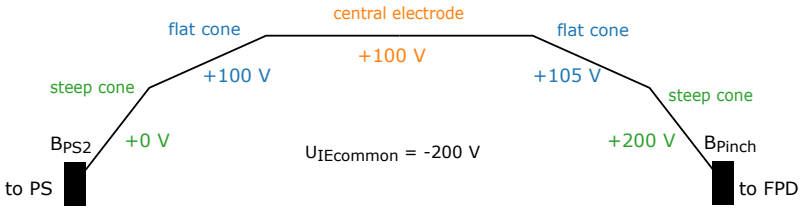

(b) Asymmetric potential

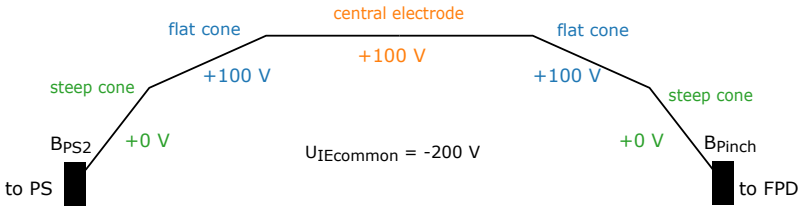

(c) Blocking potential

Figure 5.21: Potential configurations used in section 5.3.1. For all cases $B_{\mathrm{PS2}} = B_{\mathrm{Pinch}} = 4.2\,\mathrm{T}$. (a) Symmetric potential with equal voltages on both steep and flat cones. The steep cones are more positive for good transmission conditions. (b) Asymmetric potential with more positive flat and steep cones on the detector side. Most negative potential is applied to the steep cone on the PS side. This way electrons are more likely transmitted towards the detector than the PS side. (c) Blocking potential with more negative steep cones compared to the other IE. Electrons are blocked at both MS exits.

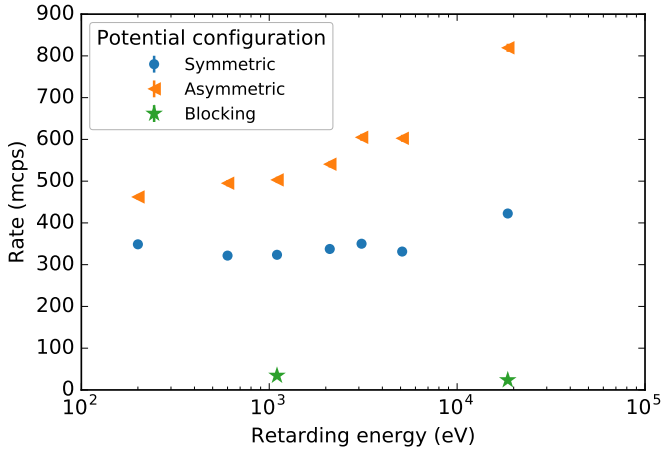

Figure 5.22: Background rate as a function of retarding energy for the three different potential configurations depicted in fig. 5.21.

MS on both sides. In contrast is the asymmetric configuration (see fig. 5.21(b)). Here the steep and flat cone on the detector side are on more positive potential with respect to all other electrodes. This way transmission towards the FPD is promoted whereas it is blocked in direction of the PS. If the voltage dependency originates from electrons having a better transmission towards the PS than the FPD, a constant background rate is expected in this setting. Through more negative potentials on both steep cones relative to the other electrodes a blocking on both MS exits is created, referred to as blocking potential (see fig. 5.21(c)). With this setting the effectiveness of electron blocking is tested. In those three configurations the background's high voltage dependency is studied.

The background rate for different retarding energies in the potential configurations illustrated in fig. 5.21 is shown in fig. 5.22. With symmetric potentials a dependency on the high voltage is observed, especially pronounced from 5 keV to 18.6 keV. The same measurement with asymmetric potential settings shows a heavily amplified drop in rate towards lower retarding energies. From the tested hypothesis such a behavior is not anticipated. The measurement with blocking potentials at both MS exits however reveals a highly suppressed background rate showing that electrons are successfully blocked.

Those measurements show that the high voltage dependency is enhanced when electrons are forced to leave the MS towards the FPD. Therefore electrons preferably leaving in direction of the PS can not be the reason for the background's high voltage dependency.

5.3.2 Impact of non-axial electric fields

Stored electrons are not expected to generate a high voltage dependency since they exit the MS through scattering. Such a dependency could arise if active removal mechanism of stored electrons are considered. In normal operation electric and magnetic pulses can be used for effective removal of such electrons. The later requires strong perturbation of the magnetic field lines through a significant change of the air coil currents or a polarity switch. If such changes occur during a measurement a highly elevated rate would be observed due to collisions of the flux tube with the vessel walls. Besides, air coil parameters are precisely monitored such that variations are detected promptly. Therefore unrecognized magnetic pulses are unlikely responsible for the high voltage dependency. Electric dipole fields can be created through different potentials on the spectrometer half spheres. During usual operation both halves are shorted preventing formation of such a dipole field. Besides the dipole halves the MS voltage system is designed axial symmetric to suppress stray fields, see fig. 5.23. However deformations of the vessel in the order of $10^{-2}\,\mathrm{m}$ with respect to axial symmetry [125] induce non-axial symmetric fields creating a small electric dipole field. By calculating the potentials on a spectrometer radius of $r = 4.65\,\mathrm{m}$ in the $x-y$-plane around $z = 0\,\mathrm{m}$ for the axial-symmetric MS and the actual slightly deformed vessel the resulting potential deviations are computed. They are shown in fig. 5.24. The 'upper MS' half refers to $y > 0\,\mathrm{m}$ from $\phi = 0$ at $x = 4.65\,\mathrm{m}$ to $\phi = \pi$ at $x = -4.65\,\mathrm{m}$. Analogously defined is the 'lower MS' half with $y < 0\,\mathrm{m}$ from $\phi = 0$ at $x = -4.65\,\mathrm{m}$ to $\phi = \pi$ at $x = 4.65\,\mathrm{m}$. Deviations up to $200\,\mathrm{mV}$ occur, potentially forming a small electric dipole field. To investigate whether this is a possible origin of the background's high voltage dependency dedicated measurements are performed.

Assuming non-axial fields are the culprit they can be suppressed by maximizing axial-symmetric components and at the same time suppressing others. In such a configuration no high voltage dependence of the background rate should be observed. It can be achieved by small offsets on all IEs, in the order of $-10\,\mathrm{V}$ or $-50\,\mathrm{V}$, and maximal voltages on the steep cones and the APEs of $300\,\mathrm{V}$. A small overall IE voltage is set to suppress non-axial field contributions and to maintain at the same time electric shielding of the flux tube. Both electrodes, steep cones and APE, induce a strong axial-symmetric component. The configuration is schematically shown in fig. 5.25.

With the IE voltages of $-10\,\mathrm{V}$ and $-50\,\mathrm{V}$ and maximized axial potentials, the background is investigated at the four vessel voltages $-0.1\,\mathrm{kV}$, $-1.1\,\mathrm{kV}$, $-5.1\,\mathrm{kV}$ and $-18.6\,\mathrm{kV}$[4]. As a reference the same measurement is performed with only the

[4]The data point at $U_{\mathrm{IE}} = -50\,\mathrm{V}$ and a vessel voltage of $-0.1\,\mathrm{kV}$ could not be evaluated due to an

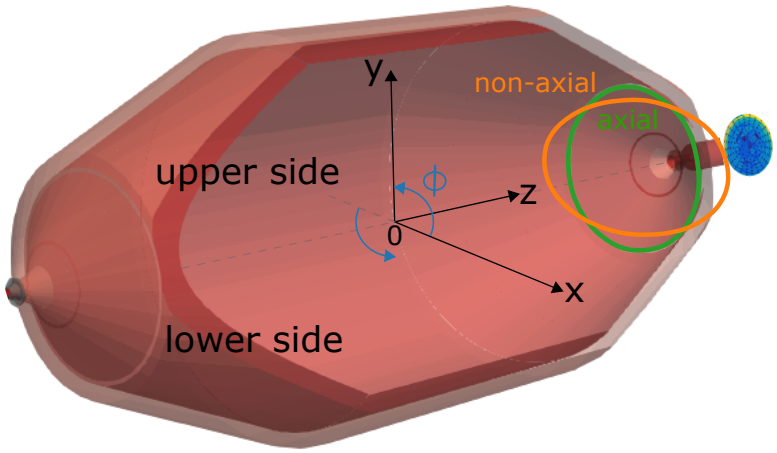

Figure 5.23: Scheme of the MS: For a perfect axial symmetric vessel, resulting electric fields are radially symmetric (green). A slight deformation of the vessel and therewith electrodes leads to a non-axial component (orange). Resulting potential deviations are calculated using Kassiopeia and shown in fig. 5.24.

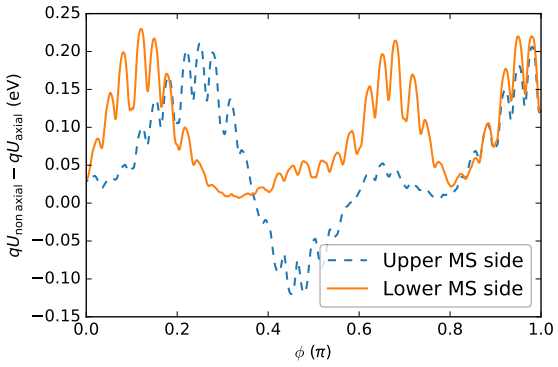

Figure 5.24: Potential difference provoked from non-axial fields arising from vessel deformation. It is plotted for the lower and upper spectrometer side as a function of angle ϕ as illustrated in fig. 5.23.

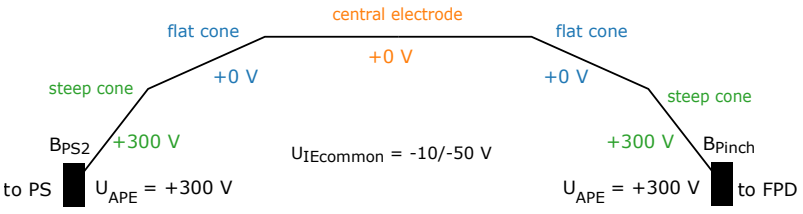

Figure 5.25: Potential configuration for minimized non-axial components accomplished through overall small IEs. Electrodes less affected by the vessel deformation are set to maximal potential of 300 V, the steep cones and the APEs.

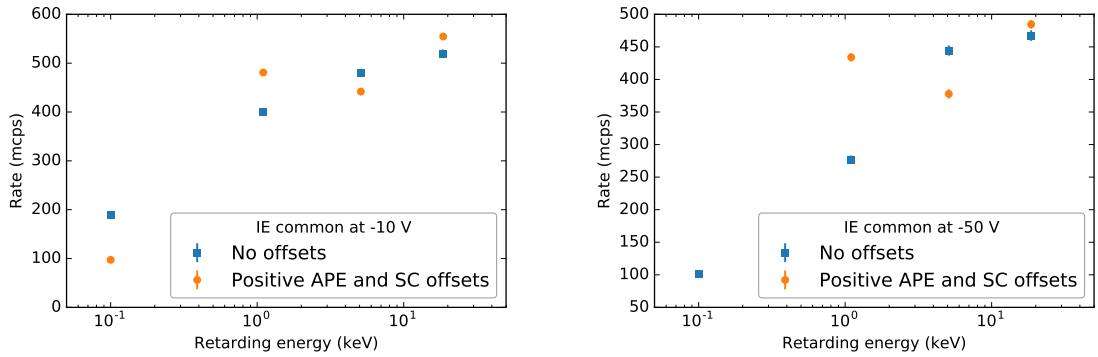

(a) (b)

Figure 5.26: Background rate as a function of high voltage with suppressed non-axial fields (no offsets) and maximized axial potentials (positive APE and SC offsets) for $U_{\mathrm{IEcommon}} = -10\,\mathrm{V}$ (a) and $-50\,\mathrm{V}$ (b).

suppressed non-axial contributions, hence without the positive offset potentials on the steep cones and APEs ($U_{\mathrm{APE}} = U_{\mathrm{SC}} = 0\,\mathrm{V}$). The results of those studies are shown in fig. 5.26. Without positive offset potentials ('no offsets') a significant drop in rate is observed from 18.6 keV to 100 eV for both IE voltages. Switching to the configurations with maximized axial-symmetric fields shows equivocal results. The two measurement points at $-18.6\,\mathrm{kV}$ and $-1.1\,\mathrm{kV}$ indicate a weakened voltage dependence. However the data at $-5.1\,\mathrm{kV}$ and $-0.1\,\mathrm{kV}$ points towards the opposite. Hence no definite statement can be made on the high voltage dependency's origin based on this measurement.

Given those inconclusive results the impact of a small dipole field on the background is investigated further. To do so an artificial dipole field is created through a 2 V offset on one of the IE dipole halves. If a small dipole field caused by the deformed spectrometer vessel generates the background's high voltage dependence it should be affected by an additional static dipole field. Its influence is expected to be lessened with strong axial field, created for instance by 300 V on the steep cones. The results are shown in fig. 5.27. Without reinforced axial-symmetric fields, only with $-50\,\mathrm{V}$ on all IEs, a small static dipole reduces the background's voltage dependence. This is observed independent of the employed dipole half. Hence a small electric dipole field influences the background's behavior at different retarding potentials. Applying the static dipole field with additional 300 V on the steep cones counteracts this effect and even leads to a more pronounced dependency on the potential (red triangles in fig. 5.27). Although impact of the positive steep cone is expected, a more pronounced voltage dependency is not anticipated based on fig. 5.26.

active extractor ion gauge at the PS.

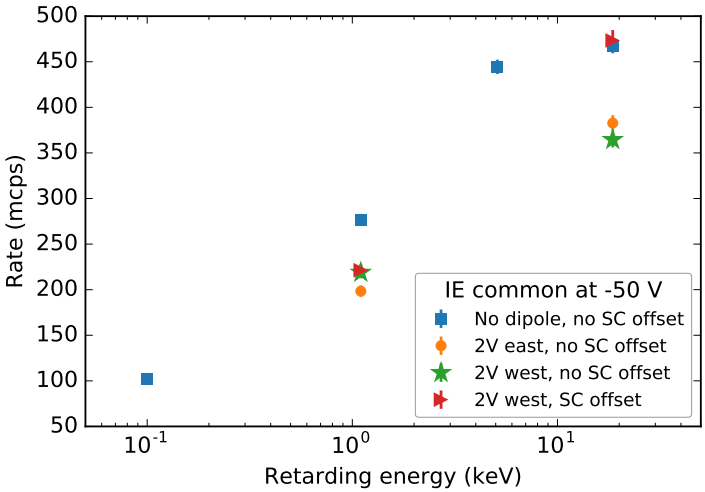

Figure 5.27: Background rate without (no dipole, no SC offset) and with static electric dipole field (2V east/west) at different retarding energies. In addition a measurement with 300 V on the steep cones is performed (2V west, SC offset).

Based on made observations non-axial fields inducing a small electric dipole field can not be excluded as origin of the background's high voltage dependency. Since the results are not definite further investigations should be carried out in this regard.

5.3.3 Conclusion

The background rate in KATRIN drops with decreasing retarding energy. Past investigations pointed towards stored electrons as origin of this behavior. To cause such a high voltage dependency, trapped electrons need to be prevented from reaching the FPD by some mechanism. Two possible reasons were experimentally studied.

- **Uneven transmission probability towards PS and FPD**: Electrons were blocked in direction of the PS by more negative potential and at the same time directed towards the detector by more positive potentials. In this configuration, electrons should be detected with high probability and not escape into the PS. The results however show an enhanced voltage dependency of the background rate instead of the expected suppressed one. Therefore an increased transmission of electrons into the PS does not seem to be the origin of the background's vessel voltage dependency.

- **Electric dipole field**: Such a field removes stored electrons by an $E \times B$-drift. Through non-axial fields within the MS created by slight vessel deformation, a weak dipole field is created. Measuring in a field configuration with suppressed non-axial fields and maximized axial symmetric component is expected to suppress those fields. This configuration impacts the background's behavior, but not consistently over the whole voltage range. Therefore no clear conclusion can be drawn at this stage. Investigations with an artificial induced dipole field show a weakened high voltage dependence which is canceled by improving the transmission conditions.

First results regarding the background's high voltage dependency were achieved. Up to now the origin is still an open question. Measurements show that it is sensitive to transmission conditions and to static dipole fields. More detailed investigations have to be carried out to clarify the situation.

6 Background during the first neutrino mass measurement - KNM1

The first neutrino mass measurement at the KATRIN experiment, **K**atrin **N**eutrino **M**ass 1 (KNM1), took place from April 10th to May 13th 2019. At a column density of $1.1 \cdot 10^{17}\,\mathrm{cm}^{-2}$ (95 % T_2, 4 % DT and 1 % HT), corresponding to 22 % of the nominal value, 274 tritium β-spectra were recorded. A combined bias-free analysis of the taken β-spectra led to the final result of $m_\nu < 1.1\,\mathrm{eV}$ at 90 % C.L. (Lokhov-Tkachov [126]) at a sensitivity of 1.1 eV (90 % C.L.) [29, 127]. This section focuses on the background characterization during the first neutrino mass campaign. The employed measurement time distribution is discussed in section 6.1. Reference measurements prior to the campaign revealed major impact of the measurement configuration on the background rate, leading to the employed setup of the MAC-E-filters, described in section 6.3. The background properties during the tritium spectrum scans are depicted in sections 6.4 to 6.7. Their impact on KNM1 is given in section 6.8.

6.1 Measurement time distribution

The live time of each of the tritium β-spectra amounts to 2 h. This time is distributed over 40 retarding energies as illustrated in fig. 6.1. The voltage points are scanned alternating up (from low to high retarding energy) and down (from high to low retarding energy). For neutrino mass analysis only the interval $E_0 - 40\,\mathrm{eV}$ to $E_0 + 50\,\mathrm{eV}$ is employed. Here most of the measurement time is spent, distributed in order to take into account the shape of the tritium β-decay spectrum and a possible neutrino mass signal. Data points deeper in the spectrum are used for systematic studies and cross-checks. Among other parameters, the deepest point in the spectrum, at $E_0 - 200\,\mathrm{eV}$, can be used to monitor the tritium source stability. Five data points with $qU > E_0$, distributed from $E_0 + 5\,\mathrm{eV}$ to $E_0 + 50\,\mathrm{eV}$, measure the background rate in each spectrum scan. The spacing of the points increases the further they are away

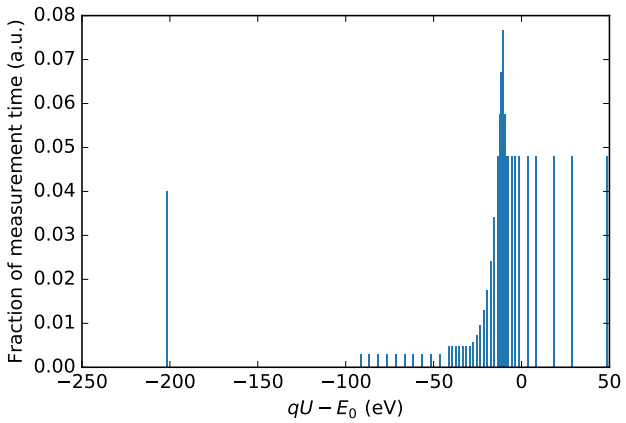

Figure 6.1: Distribution of the measurement time over retarding potential energies used in KNM1.

from the endpoint, resulting in the measurement points $E_0 + 5\,\text{eV}$, $10\,\text{eV}$, $20\,\text{eV}$, $30\,\text{eV}$ and $50\,\text{eV}$. This way they are, on the one hand, close to E_0 such that the measured background rate reflects the one within the tritium β-spectrum. On the other hand, the energy range of $45\,\text{eV}$ provides some sensitivity to a possible retarding voltage dependence of the background. For continuous monitoring, the five background points are evenly distributed over the scan duration, which allows the background rate to be examined with respect to possible time-dependent effects. As will be seen in section 6.8 such non-Poisson behavior has a significant impact on the neutrino mass uncertainty. Overall 25 % of the measurement time is spent in the background region based on neutrino mass sensitivity considerations.

6.2 Analysis cuts

Unless mentioned otherwise the following analysis cuts are applied to KNM1 data within this chapter.

Pixel section

In the analysis not all FPD pixels are analyzed. Figure 6.2(a) shows the pixel distribution of a MS background measurement. Overall 31 out of 148 pixels are excluded, shown in gray: Six of them due to FPD effects (e.g. sporadic noise), the others due to (partial) blocking of the β-electrons by misalignment or the forward beam monitor (detector installed in the transport section that monitors the source activity).

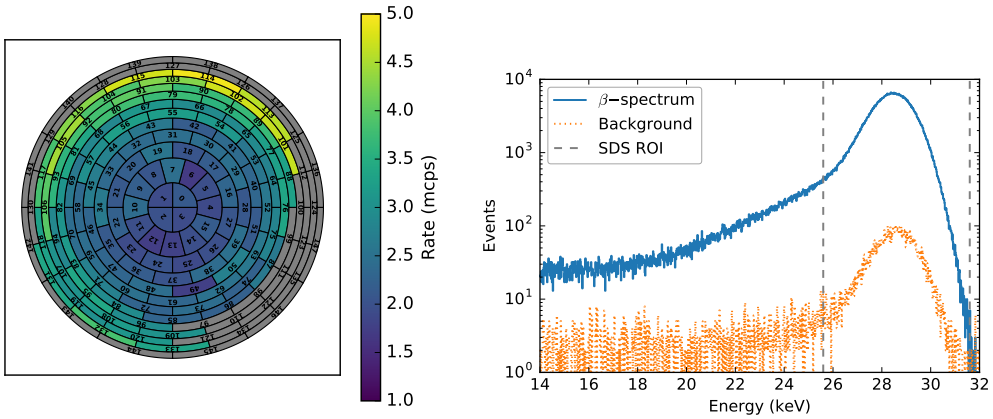

(a) Pixel map

(b) Energy spectrum

Figure 6.2: (a) Pixel selection during KNM1. In the analysis 31 out of 148 pixels are excluded (shown gray). (b) Energy spectrum of background measurement and tritium β-scan within the ROI.

Region of interest

The ROI for SDS measurements[1] is a window of 6 keV around the expected electron energy. In fig. 6.2(b) the energy spectrum of such a SDS measurement together with the corresponding ROI is shown. For comparison the energy spectrum of tritium β-electrons is added to the figure. Application of the SDS ROI would cut a significant fraction of the signal. Therefore the analysis range is extended for maximal signal coverage, leading to the KNM1 ROI of 14 to 32 keV.

6.3 Configuration of the MAC-E filters

6.3.1 Magnetic field

All superconducting magnets are operated at 70 % of their nominal field, resulting in the fields listed in table 6.1.

The magnetic field in the analyzing plane is optimized in terms of neutrino mass sensitivity [47]. A larger magnetic field leads to a lower background rate, improving the sensitivity. This is counteracted by the accompanied worsening of the energy resolution. Best sensitivity is found at a magnetic field of $B_{\mathrm{ana}} = 6.3\,\mathrm{G}$, which is the standard configuration for this campaign.

[1] Measurements involving only the spectrometers and the detector. The valve that connects the SDS to the transport and source section remains closed.

Table 6.1: Superconducting magnetic fields during KNM1.

magnet	field (T)
Source	2.52
PS1	3.1
PS2	3.1
Pinch	4.23
Detector	2.5

6.3.2 Inner electrodes

The background rate depends on the applied IE voltage offset (see fig. 5.20(b)). To decrease the background rate the IE voltage is lowered to −300 V. However, reference measurements reveal a highly fluctuating background rate in this configuration. Although all settings[2] were the same rate variations larger than 50 mcps were observed. This rate fluctuation arises from hydrogen anions created in the MS, investigated within [93]. Their creation is most likely related to electron field emission. Ions can be identified in the energy spectra. They appear at lower energies than electrons since they loose a higher fraction of their energy in the detector's dead layer. Figure 6.3 shows the energy spectra within the ROI of three background measurements with different background rates as listed in the legend. The ion peak appears in the energy spectrum at 18 keV next to the expected electron peak at approximately 29 keV. Its presence is correlated with an increased background rate. With lower PAE voltage of 7 kV instead of 10 kV both peaks move to lower energies indicating further negatively charged particles. In principle the ion peak in the energy spectrum can be cut by adjusting the ROI. However previous investigations of hydrogen anion induced background showed a correlation between events in the ion peak with those in the electron peak. Hence impact of hydrogen anion induced background on the rate determined from solely the electron peak can not be excluded. Therefore the standard IE voltage for KNM1 was increased to −200 V, where hydrogen anions are no longer observed.

6.3.3 Pre-spectrometer

The PS is foreseen to be operated at slightly less negative voltage than the MS thus acting as a first filter for low energy β-electrons. Long term background measurements did not indicate activity of the Penning trap, present between the two spectrometers,

[2] Valve between SDS and transport section closed. Other parameters like the PS and magnetic field configuration are unchanged.

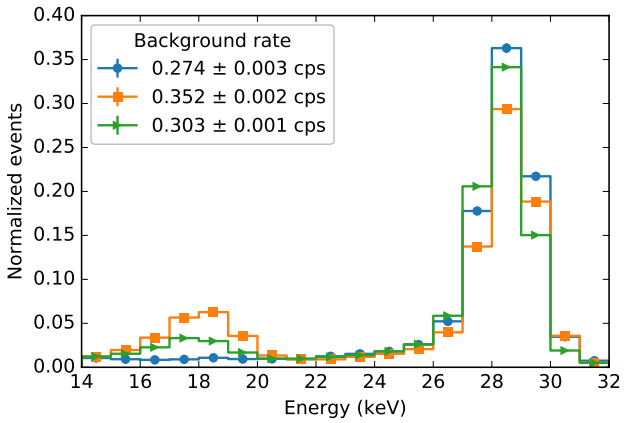

Figure 6.3: Normalized FPD energy spectra of three background reference measurements with an IE voltage of −300 V. The increased background rate coincides with an additional peak in the energy spectrum at an energy of approximately 18 keV which can be attributed to hydrogen anions produced in the MS.

in the configuration where the PS is at −18.3 kV and the MS at −18.6 kV [128]. Therefore this configuration was chosen for the first test β-scans with tritium in the WGTS. In the first scans the IE voltage is at −300 V, but there is no indication for negative ions (see section 6.3.2) in the energy spectra. Therefore the rates are not expected to be affected by this kind of background.

The measured background rates of the first tritium scans are shown in fig. 6.4. At first the column density was set to 5 % of the nominal value (blue). Already in the beginning a slight increase in background rate is visible. Additional scans were performed at about 70 % (orange) and the later ones with declining column density of about 50 % (red and green) in two different Penning wiper modes (see section 4.2.4). With increasing exposure to the tritium source, the background rate continuously increased. This rise is interrupted through application of the Penning wipers that empty the Penning trap between the two spectrometers. The wiper is applied in each tritium spectrum scan during voltage changes, about every 5 min. The wiping restores the background rate almost to the level of $\rho d = 5\,\%$. The observed reduction clearly indicates trap activity as the cause of background increase although the typical discharge-like structure is not observed. Its absence can be explained if some β-electrons create positive ions before entering the PS. The ions either become stored in the trap or hit the walls. In the later case they can generate electrons through sputtering processes similar to the background creation process described in section 4.1.3. Generated electrons are captured by the Penning trap.

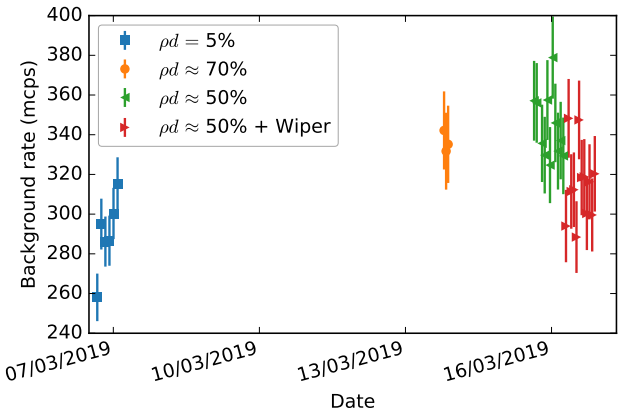

Figure 6.4: Background in tritium scans during ramp up of tritium activity. Application of the Penning wiper interrupts the increasing background rate, indicating the inter-spectrometer Penning trap as the origin of elevated background.

The positive ion hypothesis is confirmed by measurements of the background rate emitted from the spectrometer surface, shown in fig. 6.5. For one hour the rate is monitored. The Penning wiper is activated prior to data taking and after 30 min. At a PS voltage of −18 kV a strong rate increase is observed starting about 10 min after the wiper. Application of the wiper restores the rate back to the starting value. This confirms that electrons feeding the Penning trap between the two spectrometers originate from the spectrometer surface. To investigate the dependence on the PS voltage the measurement is repeated with different voltages. As shown in fig. 6.5 the rate increase is only slightly visible at $U_{\mathrm{PS}} = -10\,\mathrm{kV}$ and vanishes at $U_{\mathrm{PS}} = 0\,\mathrm{kV}$. Therefore the PS is operated with $U_{\mathrm{PS}} = -10\,\mathrm{kV}$ in KNM1. In addition the Penning wipers are triggered in every tritium scan during voltage changes.

Results of the Penning wiper measurement reported here are published within [96].

6.4 Time stability

From the five background measurement points, at retarding energies larger than E_0, an average background rate per tritium scan can be determined by summing the measured counts and times of all scans. The mean background rate over the time span of KNM1 is shown in fig. 6.6. The gap in the data points in the beginning of May is due to an intermediate warming up of the WGTS, where no tritium scans were taken. The mean background rate is (291.5 ± 0.1) mcps. Within KNM1 no

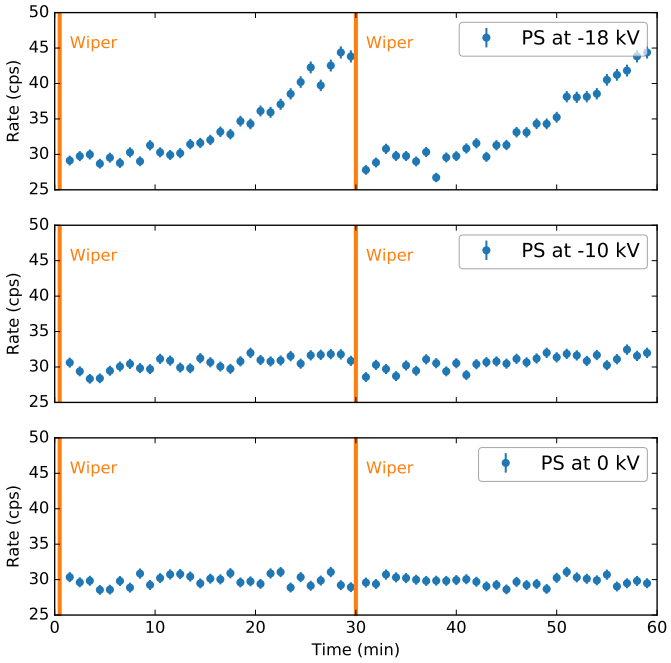

Figure 6.5: Background from the spectrometer surface at three different PS voltages. At the beginning and in the middle of the measurement the Penning wiper is triggered, marked by the orange line. With −18 kV on the PS clear activity of the trap is visible. At higher voltages its activity is highly suppressed.

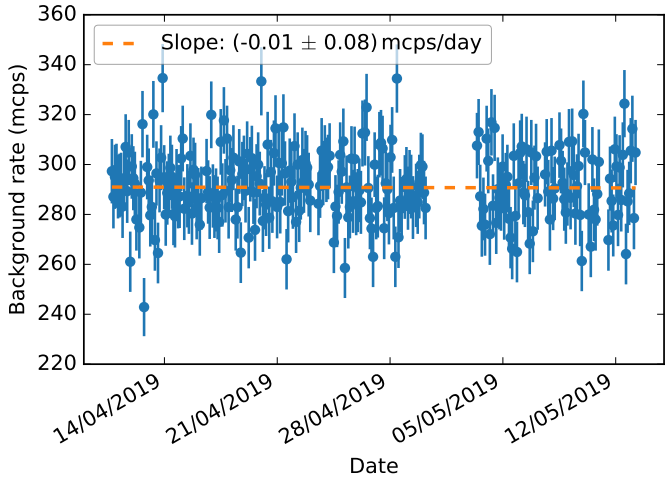

Figure 6.6: Evolution of the background rate during tritium scans over the timespan of KNM1. The fitted slope (orange dashed) is in agreement with no time dependency.

trend of the background rate is observed. Indeed, a slope of $(-0.01 \pm 0.08)\,\mathrm{mcps \cdot d^{-1}}$ fitted to the data confirms that there is no linear time dependence of the background rate within uncertainty.

6.5 Pixel distribution

The FPD is divided into 148 pixels, where each pixel records its individual background rate. Employing all background data points of the KNM1 tritium scans provides sufficient statistics for the background rate on each pixel. Figure 6.7 shows the mean background rate per pixel during KNM1. The pixel map shows an increase in rate towards outer radii, which is expected due to the higher Rydberg induced rate closer to the spectrometer walls. Without volume normalization of the rate the radial dependence is enhanced by the higher flux volumes mapped on the outer pixel rings compared to the inner ones. In addition, the radial increase of the rate is not centered around the detector's bulls-eye but slightly shifted to the lower right due to misalignment. The same background pixel distribution is also observed in reference background measurements without tritium in the WGTS [128].

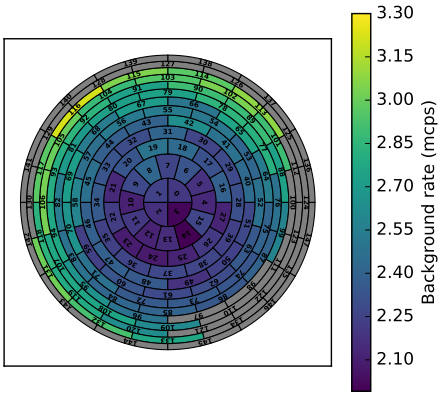

Figure 6.7: Distribution of the background rate over the active pixels during KNM1 based on the 274 tritium β-scans.

6.6 Non-Poisson background component

Each of the five background data points recorded within one tritium scan has a duration of 360 s. The summed number of counts over all pixels in each of the background data points is used to study the distribution of background events. In fig. 6.8 the counts of each β-scan are binned in a histogram. If radon-induced background is negligible, the counts are expected to be distributed according to a Poisson distribution with the mean λ and the corresponding width $\sqrt{\lambda}$. However, the actual distribution of the background rate is broader than expected. The observed broadening points towards a non-Poisson background mechanism, hence stored particle induced background caused by radon (see section 4.1.2). The amount by which the actual background distribution is wider than a Poisson distribution can be expressed either as

- **relative** non-Poisson fraction f_{relative}: This quantity expresses the relative amount by which the distribution, fitted by a Gaussian distribution with the width σ_{Gauss}, is broader with respect to a Poisson distribution and is defined by

$$f_{\text{relative}} = \frac{\sigma_{\text{Gauss}}}{\sqrt{\lambda}} - 1. \tag{6.1}$$

- **absolute** non-Poisson width f_{absolute}: This quantity expresses the absolute width by which the distribution is broader than a Poisson distribution. It can be obtained by either

$$f_{\text{absolute}} = \sqrt{\sigma^2_{\text{Gauss}} - \lambda} \tag{6.2}$$

  or by fitting a convolution of Poisson and Gauss distribution to the actual background distribution.

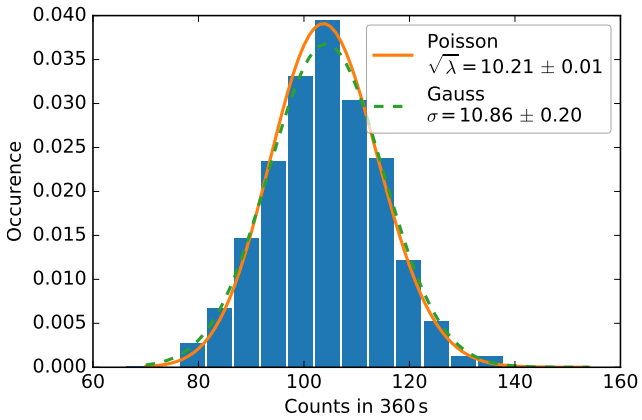

Figure 6.8: Distribution of background events in 360 s. The width of the distribution is broader than expected from a Poisson distribution. Corresponding uncertainties of the width are calculated with the bootstrap method.

For KNM1 the relative non-Poisson fraction f_{relative} from eq. (6.1) is $(6.4 \pm 1.9)\,\%$. The absolute non-Poisson width f_{absolute} from eq. (6.2) is (10.28 ± 1.67) mcps. In both cases the uncertainty was determined by the bootstrap method [129]. By fitting a convolution of Gauss and Poisson distribution to the data, the absolute non-Poisson width f_{absolute} of (10.34 ± 1.69) mcps is obtained with a significance of $3.3\,\sigma$. The deviation from a Poisson distribution acts like an increased statistical uncertainty and needs to be considered in the neutrino mass analysis. Its impact is described in section 6.8.

6.7 Retarding voltage dependence

Towards very low retarding energies the background rate decreases (see chapter 5). Such a dependence in the energy range of neutrino mass analysis introduces a bias if it is not considered. Dedicated measurements are carried out to investigate a possible retarding energy dependence in the region close to the measured spectral endpoint. Investigations performed within [130] in a range of 18 to 19 keV did not show a significant energy dependence of the background rate. During tritium scans the five points above E_0 are used to monitor the retarding energy dependence. Summing up the counts of all pixels and the live times of all tritium scans at the individual retarding energies leads to the background rate as a function of retarding energy shown in fig. 6.9. A fit gives a slope of (47.0 ± 48.3) mcps·keV^{-1}, which is in agreement with previous observations of no significant slope. Compared to dedicated measurements the sensitivity of this method is only finite due to the limited energy

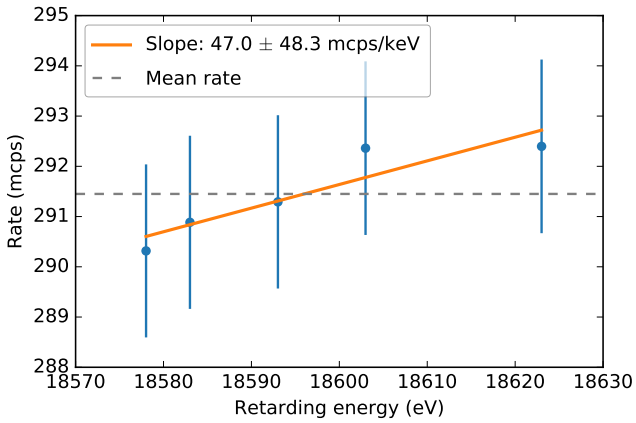

Figure 6.9: Background rate during the KNM1 tritium scans. The fitted slope is not significant. For comparison the mean background rate is indicated by the dashed line.

window.

Therefore the background slope is constrained by a separate dedicated measurement in the neutrino mass analysis. During the FT campaign the background was studied in a 1.6 kV range. The corresponding data set is shown in fig. 6.10. For yet unknown reason the background rate is higher during FT than in KNM1. A fit gives a slope of $(4.44 \pm 4.77)\,\mathrm{mcps{\cdot}keV^{-1}}$, which is not significant and in agreement with previous investigations [130]. The FT measurement is the latest reference for the background's retarding voltage dependence with sufficient uncertainty prior to KNM1. Therefore the FT data set is used to constrain the retarding voltage dependence in the neutrino mass analysis. Since no significant slope was observed in carried out measurements, a zero slope with an uncertainty of $5\,\mathrm{mcps{\cdot}keV^{-1}}$ is assumed. The impact of the systematic uncertainty in the neutrino mass analysis is discussed in section 6.8.

6.8 Impact on the neutrino mass sensitivity

The final KATRIN sensitivity requires precise knowledge of the system properties, e.g. response function, to achieve the targeted systematic uncertainty. Several quantities contribute to the systematics budget. By the time of KNM1 not all are known to their final level. Further commissioning measurements will improve the understanding of systematic effects.

The statistical and systematic uncertainties contributing to the overall neutrino mass

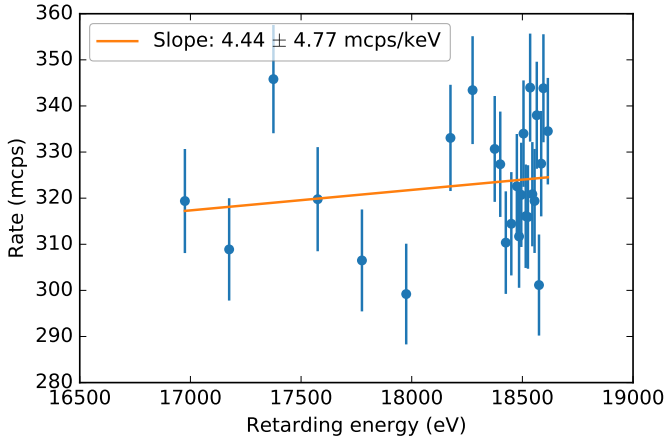

Figure 6.10: Background rate over a range of 1.6 keV measured prior to KNM1 within the FT measurement campaign. The fitted slope is not significant.

uncertainty obtained from KNM1 are shown in fig. 6.11. Given the measurement time of one month the overall uncertainty is clearly dominated by the statistical contribution. From all contributing systematic effects the most dominant contributions are related to the background. Of the highest importance is the non-Poisson background component caused by a radon-induced background fraction. Due to its uncorrelated nature its contribution is currently by far the largest among the systematic effects. Hence mitigation of this background characteristic is of high importance for KATRIN. For future measurements a sub-cooler will be installed for the baffle system (see section 4.1.2) allowing operation at lower temperatures. In this way, the radon retention capability will be more robust against copper surface properties. The second most dominant systematic contribution in terms of background is the high voltage dependency. The contribution is relatively large due to the limited amount of statistics available in the dedicated background slope measurement. In future measurements the statistics will be greatly increased and thus the corresponding systematic uncertainty reduced.

Additional contributions to the systematic uncertainty arise from the response function ($\rho d\sigma$, magnetic fields and energy loss function), the FSD and the analysis strategy (Stacking). The latest refers to the summing of all counts, pixels and tritium spectra at the individual retarding voltages. This way one tritium spectrum with averaged retarding potentials is created, which is analyzed. Through this approximation a certain systematic uncertainty is introduced.

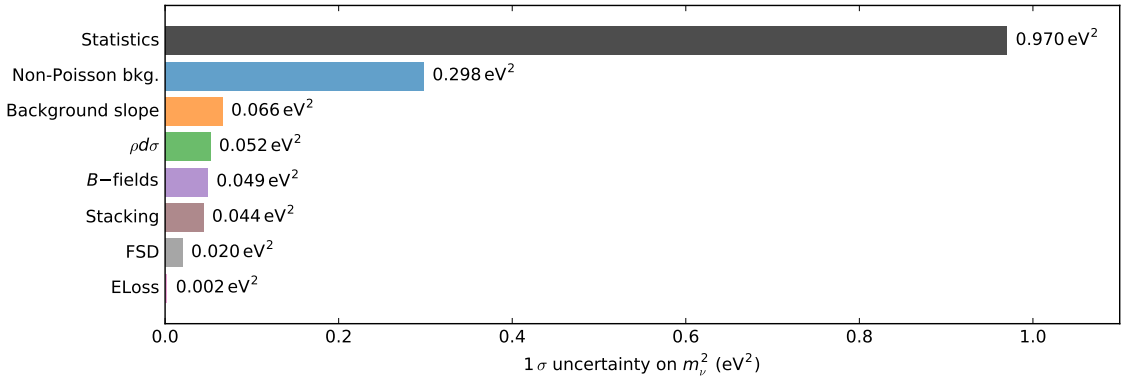

Figure 6.11: Uncertainty budget in the first neutrino mass measurement. Shown are the $1\,\sigma$ (standard deviation) uncertainties of the observable m_ν^2 from individual contributions: statistical-only, background-related and other systematic effects as described in the text. Values kindly provided by Christian Karl.

7 Background mitigation strategy - Shifted Analyzing Plane

The background rate of about 290 mcps during KNM1 exceeds the KATRIN design value of 10 mcps. Sensitivity studies show that the targeted neutrino mass sensitivity of 0.2 eV at 90 % C.L. can not be achieved under those conditions (see section 3.4). The background rate is predominantly induced by the Rydberg mechanism with small contributions from radon and detector background. Through an improved baffle system radon will be suppressed to a negligible amount in future measurements. Detector induced background can be vastly reduced through the application of optimized analysis cuts. As these contributions make up only a small part of the background, the Rydberg background must be targeted in order to achieve a significant reduction of background rate. A promising strategy is the so-called **S**hifted **A**nalyzing **P**lane (SAP), which is presented within this chapter. This approach is based on the background rate's flux volume dependency. The concept is presented in section 7.1. First test and characterization measurements were carried out and are presented within sections 7.2 and 7.3. The potential of this concept in terms of achievable sensitivity is depicted in section 7.4.

7.1 Concept

Background electrons generated through the Rydberg mechanism have low energies (based on the investigations presented in section 5.1 up to 2 eV). In the standard electric field configuration, the maximal retarding energy is reached in the spectrometer center. Low energetic background electrons do not have sufficient energy to overcome this potential barrier. Hence only electrons created in the volume between the maximal retarding energy and the spectrometer exit can contribute to the measured background, referred to as visible volume or downstream volume. In case of the standard measurement configuration, where the analyzing plane is in the spectrometer center, the visible volume amounts to about half of the flux tube volume. The visible volume and thus the background rate can be reduced through a shift of the analyzing plane further towards the FPD. This is visualized in

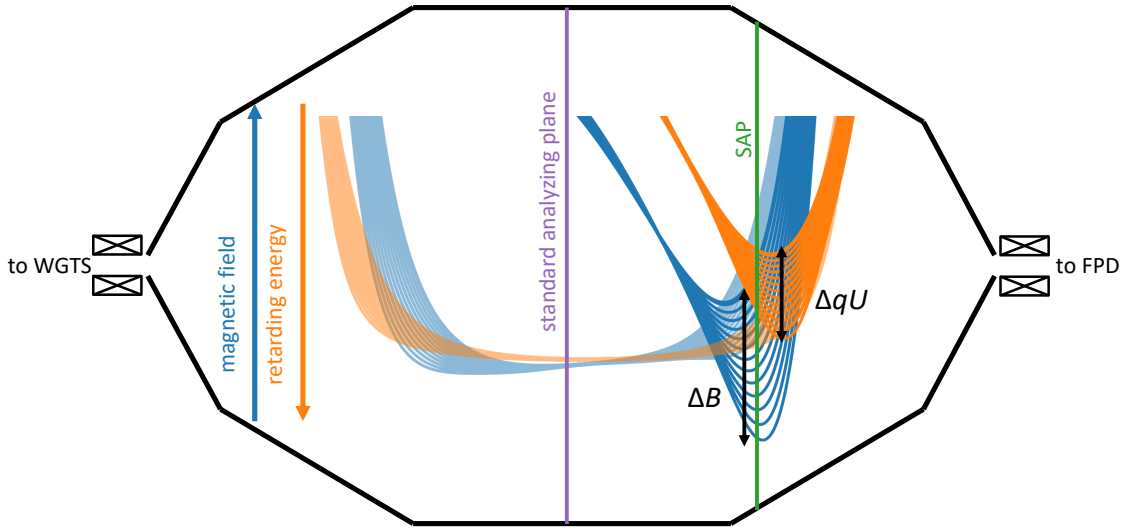

Figure 7.1: Scheme of the magnetic fields and electric potentials along the guiding magnetic field lines for the standard/central (transparent) and **S**hifted **A**nalyzing **P**lane (solid) configuration. The vertical lines indicate the position of the analyzing plane. Through a shift the visible flux volume is changed and therewith the background rate.

fig. 7.1. In the shown scheme of the MS, the magnetic field lines pointing towards the detector rings are indicated in blue and the retarding energy along them in orange. For the standard measurement configuration the magnetic field is slowly reduced towards center. Analogous the retarding energy is increased towards the center, where the maximum is reached. This defines the analyzing plane in the middle of the spectrometer. Due to the technical design of the air coils and the IE system, it is possible to shift the analyzing plane further in direction of the FPD by adjusting the currents and voltages. The resulting magnetic field and retarding energy for an example SAP configuration are indicated in fig. 7.1 in analogy to the standard setting. Shown SAP setting reduces the visible volume by a factor of about 2.5 compared to the standard configuration. Expected background reduction from such a setting is of similar magnitude. The SAP does not only affect Rydberg induced background electrons, but all low energy electrons created within the spectrometer [1]. Therefore this configuration is also expected to weaken radon-induced secondary electrons. Due to the potential of this method, test measurements were carried out to check validity of the assumed volume dependency of the background rate and to confirm the expected reduced background rate, see section 7.2.

[1] The electromagnetic field configuration of the SAP also affects the storing conditions of high energetic electrons within the spectrometer. Therefore this approach is also expected to reduce stored-particle induced background.

The significant lower background rate with a SAP configuration is accompanied with a severe distortion of electric potential and magnetic field. In the standard measurement configuration with central analyzing plane the magnetic fields and electric potentials are characterized by maximal homogeneity among the detector pixels. This means that electrons detected on the different pixels experience nearly the same retarding potential and analyzing plane magnetic field. Thereby systematic uncertainties are reduced since

- simulations of field and potential are less sensitive to incomplete knowledge of alignment
- field/potential can be assumed constant within one pixel.

When the analyzing plane is shifted away from the center sizable inhomogeneities, indicated by ΔqU and ΔB in fig. 7.1, are introduced. In such a configuration, electrons experience significantly different magnetic field and retarding potential, depending on their path through the spectrometer. Therefore, higher uncertainties in the fields/potentials can be expected in this configuration. Sensitivity studies, see section 7.4, show that the uncertainties must be reduced to a minimum to benefit from the lower background rate. Depending on the size of inhomogeneities the analyzing plane magnetic field needs to be known with a precision of at least 1 %. Thus the accuracy of simulation must be verified. This can only be accomplished by precise measurements of the magnetic fields and electric potentials in the analyzing plane. Available methods and first results are described within section 7.3.

7.2 Background measurements with a Shifted Analyzing Plane

Given the potential background reduction, measurements in various SAP configurations with different visible flux volumes are carried out. The magnetic flux tubes of two such settings are shown in fig. 7.2. Compared to the KNM1 configuration, the two configurations shift the analyzing plane towards the detector by about 6 m with respect to the spectrometer center. Both have a similar downstream volume of about 40 m^3. Their flux tube radii differ because of unequal analyzing plane magnetic fields. Assuming a background rate proportional to the downstream volume a reduction by almost a factor of 4 is expected. Figure 7.3(a) shows the measured background rates for different SAP configurations as a function of visible flux volume. The same analysis cuts as in KNM1 are applied (see section 6.3). For comparison a line reflecting a background rate proportional to the volume is added in green. Since the

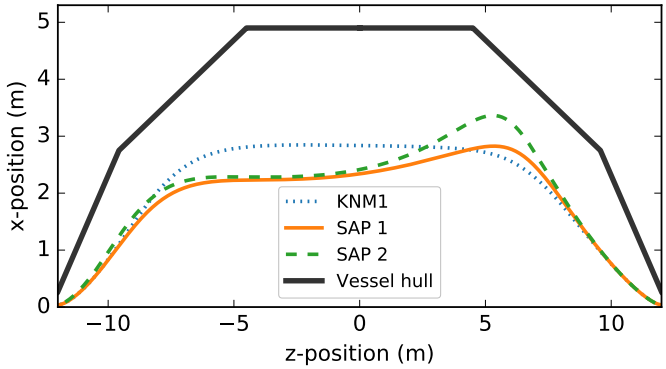

Figure 7.2: Magnetic flux tube in the MS for the nominal KNM1 setting and two example SAP configurations.

detector background is not affected by the visible flux volume it acts like a constant offset.

The measurements show a lower background rate with reduced downstream volume. Although the background rates do not follow linearly the amount of visible volume, the rate could be reduced by a factor of 2.5 compared to KNM1. Deviations from the linear behavior are most likely caused by the uneven distribution of Rydberg induced background within the spectrometer volume (due to field ionization and radiative de-excitation of Rydberg atoms). This affects above all SAP configurations with low magnetic field in the analyzing plane and low downstream volume, since their flux tubes are closer to the vessel walls. Those configurations usually also suffer from high magnetic field and electric potential inhomogeneity. It can be counteracted by an increased magnetic field in this region. However limitations to the air coil currents and the finite amount of the coils in the relevant region did not allow to increase the magnetic field at the time of the measurement. Ignoring such restrictions, the background rate can in principle be reduced as desired.

Given above results, additional air coils were installed [131]. They allow to shift the analyzing plane further towards the detector. Additionally they increase the flexibility when implementing such settings, which enables improved field and potential homogeneity. After a spectrometer bake-out and the air coil upgrade, further background measurements in SAP configuration were carried out. The results are depicted in fig. 7.3(b). The spectrometer bake-out reduced the background rate by 90 mcps. By means of the SAP the background rate could be further reduced down to the detector background level. However, those measurement configurations suffer from extreme inhomogeneities and are thus not suitable for neutrino mass measurements. Compared to fig. 7.3(a) an improved agreement with a linear relation of background rate and volume could be achieved. These results confirm the potential

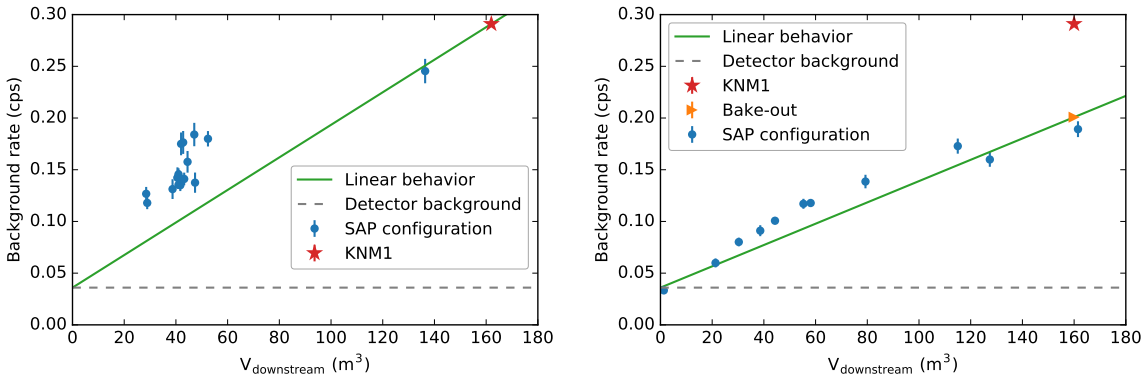

(a) pre-baking

(b) post-baking and hardware upgrade

Figure 7.3: Background rates with various SAP configuration carried out directly after KNM1 (a) and after the subsequent bake-out and air coil upgrade (b). They are shown in dependence of the flux volume between the analyzing plane and the spectrometer exit (downstream volume). The gray dashed line indicates the detector induced background which is not affected by the measurement configuration. A background rate proportional to the volume is expected to follow the solid green line.

of the SAP for background mitigation.

7.3 Determination of analyzing plane fields

The SAP enables a significant reduction of background rate. It is accompanied by a spread of analyzing plane magnetic fields and electric potentials. Especially as a function of MS radius large differences are introduced. These inhomogeneities are directly mapped onto the detector. The corresponding magnetic field and electric potential per detector ring are visualized in fig. 7.4 (misalignment neglected). For standard KNM1 settings retarding potential as well as analyzing plane magnetic field are nearly constant over the whole FPD. The spread of potential amounts to 0.1 V and of magnetic field to 0.1 G. In case of a SAP configuration with low inhomogeneities (SAP 1) they are in the order of 4.9 V and 1.6 G (misalignment neglected). This causes variations within one pixel that are larger than the spread over the whole detector in the standard configuration. The variations need to be taken into account in the neutrino mass analysis because they impact the transmission properties. Therefore the magnetic fields and electric potentials per pixel and their spread within one pixel need to be determined with high accuracy to limit systematic uncertainties.

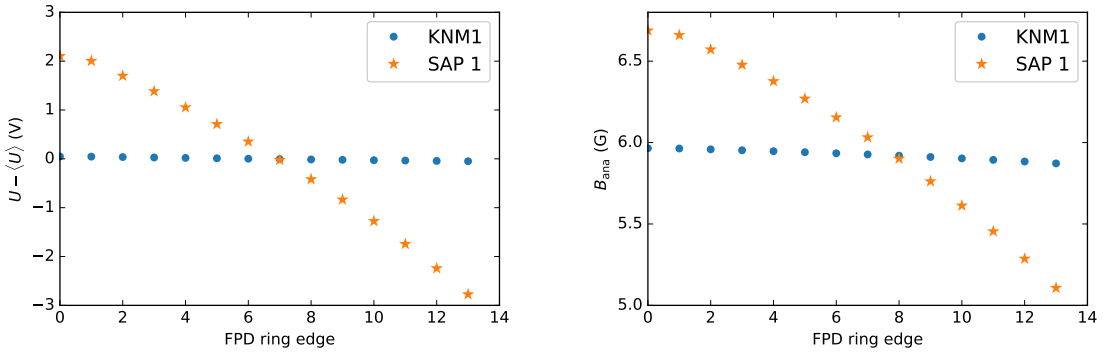

(a) Electric potential

(b) Magnetic field

Figure 7.4: Electric potential (a) and magnetic field (b) in the analyzing plane for the KNM1 and the SAP 1 configuration. They are shown as a function of detector ring. Misalignment is not considered in this simulation.

Due to the high inhomogeneities in SAP configuration simulations of those settings are very sensitive with respect to alignment. In standard settings the fields and potentials are very homogeneous such that the simulation is not very sensitive to the exact position of the analyzing plane within the MS. Whereas in a SAP setting wrong knowledge by only a few centimeters has significant impact on the magnetic field and electric potential. Therefore high precision measurements of the analyzing plane fields and potentials are needed. Sensitivity studies (see section 7.4) show that accurate knowledge of the analyzing plane properties is essential to benefit from the reduced background rate. This holds especially in case of large inhomogeneities. Several methods are available in KATRIN to determine the analyzing plane magnetic fields and potentials, which are depicted in the following. The measurement configuration of the investigated SAP setting, referred to as SAP 1, is depicted in appendix A.9. Corresponding run numbers are listed in the same section. With a background rate of (131.3 ± 9.5) mcps, the background is by more than a factor 2 lower in this configuration compared to KNM1. In addition the spread of magnetic field and electric potential is still moderate for a SAP setting.

7.3.1 Simulation

With Kassiopeia (see section 3.3.1) the electric potential and magnetic field in the analyzing plane can be calculated. The current knowledge on the experiment's alignment is implemented in the simulation geometry to simulate the fields and potentials with best possible accuracy. Based on such simulations the per pixel retarding potential offsets and magnetic field values in the analyzing plane shown in

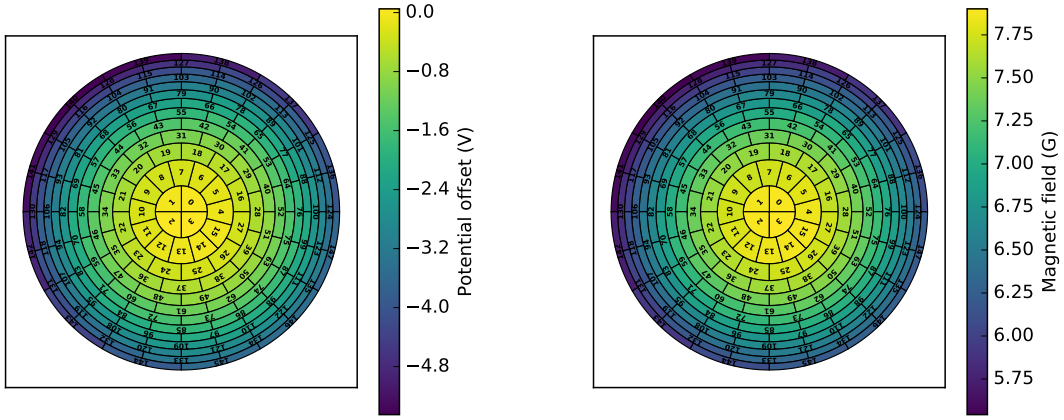

(a) Potential offsets

(b) Magnetic field

Figure 7.5: Simulation of the retarding potential offsets shown relative to pixel 0 (a) and the corresponding analyzing plane magnetic field (b) in SAP 1 configuration. Simulation carried out by Jan Behrens.

fig. 7.5 are obtained. The potential offsets are shown relative to the offset at pixel 0. Towards outer rings/radii the electrons experience a higher retarding energy. The analyzing plane magnetic field drops towards the outer detector rings, reflecting the increasing radius of the magnetic flux tube in the MS. Due to the slight misalignment of the experiment, the maximal potential and highest magnetic field is not exactly in the detector center but shifted to the lower right.

7.3.2 Electron gun

With the electron gun (angular selective, mono-energetic) the transmission properties can be measured [68, 132]. They depend on the energy and angular distribution of the electron source and the spectrometer characteristics. To extract the magnetic field and electric potential within the spectrometer from such a measurement the impact of electron gun characteristics needs to be separated from the impact of the spectrometer properties. This requires a precise characterization of the electron gun features, which need to be determined by dedicated measurements (see [132]). With a characterized electron gun a measurement of the transmission function at the individual FPD pixels can be used to determine magnetic field and electric potential in the analyzing plane. The fields can be interpolated to obtain their values over the complete detector. The precision of such a determination depends on the stability of the electron gun and on the accurate knowledge of electron gun characteristics. An

additional uncertainty is related to the localization of the electron gun beam within the pixel. In case of a SAP setting there are sizable inhomogeneities within one pixel, which can not be resolved. First measurements with the electron gun are planned to investigate the achievable accuracy.

7.3.3 Tritium

A pixel dependent retarding potential leads to a corresponding shift of transmission function. If a tritium β-spectrum is measured in SAP configuration, it is shifted at each pixel accordingly. Therefore the pixel wise potential offsets can be obtained by

- comparing the measured rates on the individual pixels at the same retarding energy deep in the spectrum
- fitting the spectrum with one single endpoint and per pixel retarding potential offsets.

In principle the per pixel magnetic fields, influencing the width of the transmission function, can also be estimated from the tritium spectrum if they are treated as free parameters. But such a technique requires measurements of high statistics, implying a long measurement time, to achieve sufficient uncertainties. Therefore tritium spectra are not the preferred option to determine the fields. In addition, high statistics spectra contain sufficient information on the neutrino mass so both would have to be fitted at the same time.

Nevertheless test measurements were carried out as a proof of principle. In SAP configuration, seven tritium β-scans were recorded. The spectra are analyzed using the nominal KNM1 analysis cuts (see section 6.3) leading to 31 excluded pixels. The spectra of the individual active pixels were stacked, meaning that the counts at the individual retarding potentials were summed up. This way one tritium spectrum per pixel is obtained. From the rate at $E_0 - 200\,\mathrm{eV}$, as well as from fitting, the retarding potential offsets per pixel are determined and compared to the simulation. Given the limited statistics the per-pixel magnetic fields are not analyzed.

Retarding potential offsets from measured rates

The rate deep in the spectrum can be utilized to determine the shift of potential from one pixel to another. The technique is visualized in fig. 7.6(a). It shows the rate of two pixels, number 0 and 20, 200 eV below the measured endpoint. Due to the radial dependent retarding potential the rates differ. Electrons detected at pixel

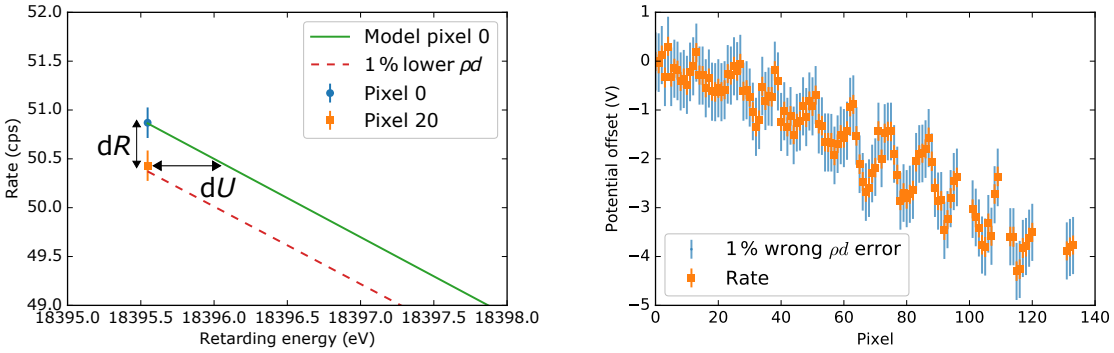

(a) Methodology

(b) Error estimation

Figure 7.6: (a) Measured rate 200 eV below the endpoint for pixels 0 and 20 and the tritium spectrum model to pixel 0 (solid green line). The later is also shown assuming a 1 % wrong column density (dashed red line). The rate difference between pixels dR can be converted to a voltage difference dU. (b) Determined potential offsets with error bars arising from statistical rate fluctuations (orange) and a wrong model assumption (blue).

20 experience a higher retarding energy than those at pixel 0. Therefore each pixel measures a rate corresponding to a different part of the tritium β-spectrum. By means of the tritium spectrum model (green solid line) the rate difference dR can be converted to a voltage difference dU. Obtained potential offsets relative to pixel 0 are shown in orange in fig. 7.6(b). Uncertainties arise from statistical fluctuations of the rate and uncertainties of the model prediction. The statistical error on the rate can be directly converted to a voltage range, like the dR to dU conversion. Uncertainties on the model parameters, like the column density ρd, introduce an additional error on the determined voltage offsets. A 1 % wrong assumed column density results in the error bars (belonging to the orange points) shown in blue in fig. 7.6(b). They predominate the error bars originating from the statistical rate uncertainty by far. Therefore, unless model uncertainties are significantly reduced this method is not sufficient for precise potential offsets determination.

Retarding potential offsets from fit

The stacked tritium spectrum is fitted with a single endpoint, per pixel background rate, per pixel normalization and per pixel retarding potential offset. The simulated values, shown in fig. 7.5(b), are used for the magnetic field per pixel. In this fit the neutrino mass is fixed to zero which is a good approximation in a short measurement with low sensitivity. Given the statistics of only seven tritium scans, systematics are

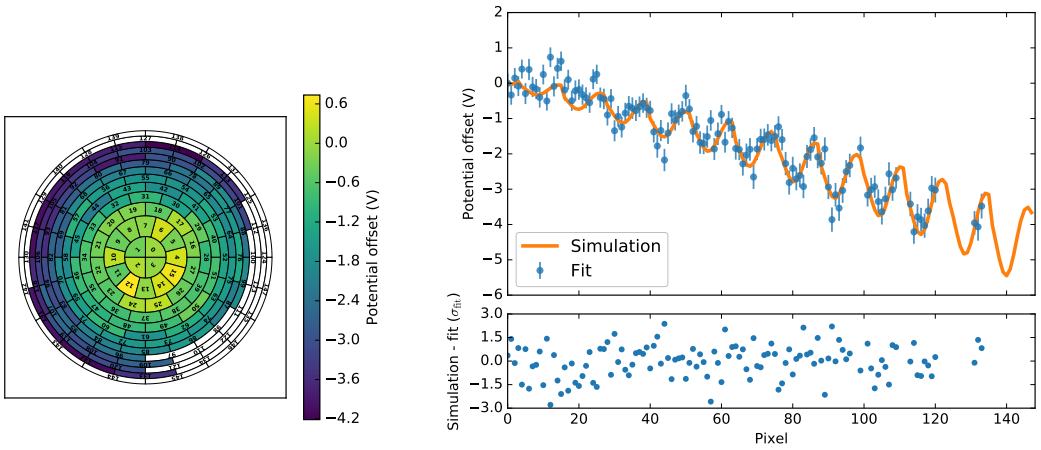

(a) Pixel map of fitted offsets

(b) Comparison to simulation

Figure 7.7: Fitted retarding potential offsets from tritium spectra (a) and the comparison to simulation (b). They are shown relative to pixel 0.

neglected in the presented analysis. The fitted potential offsets are shown in fig. 7.7(a). Similarly as for the simulation they are plotted relative to pixel 0. Figure 7.7(b) shows the comparison of fitted retarding potential offsets to simulation (see fig. 7.5(a)). Within the uncertainties good agreement is achieved. The residuals show no structure and the deviations are within 3 σ_{fit}. However the uncertainties on the fitted retarding potential offsets are with 0.27 to 0.39 V rather large such that the statistics of this measurement are not sufficient for a precise determination.

7.3.4 Krypton

For calibration and characterization $^{83\text{m}}$Kr can be injected into the WGTS. This isotope emits mono-energetic conversion electrons with energies up to 32 keV. Of high interest is the conversion electron line at an energy of 17.8 keV with a line width of 2.8 eV [57], here referred to as K-32 line, since its energy is close to the endpoint of the measured tritium spectrum. A shift of retarding potential at the individual FPD pixels causes a shift in line position. In addition, the line width per pixel reflects changes in the magnetic field. Krypton injected into the WGTS illuminates all detector pixels in the same way tritium does. Therefore the conversion electron lines reflect the same transmission properties that also tritium β-electrons experience. This is in contrast to the electron gun, where the measured transmission characteristics correspond to those of a position within the pixel. Given the similar energies, the K-32 line is well suited for a characterization of the analyzing plane.

Unfortunately this line can only be used for characterization of the setup without tritium in the source, since the tritium background is dominant otherwise. Without tritium in the source, there is only tritium induced background originating from tritium that accumulated on the rearwall, which amounts to about 10 % of the total background in the presented measurements. The accompanied background slope is estimated from rearwall tritium scans. Residual background originates from higher energetic conversion electrons and involves no additional retarding voltage dependence. In case of the conversion electron line at an energy of 30.5 keV with a line width of 1.2 eV [57], referred to as L_3-32 line, tritium induced events are no issue since all tritium β-electrons are blocked. Hence this line can also be accessed with tritium in the WGTS. In addition the L_3-32 line is more sensitive to analyzing plane properties due to its narrower line width. However the potential configuration needs to be slightly adopted with respect to the nominal tritium scanning configuration to improve the transmission conditions for such high energetic electrons. Consequently the configuration is not the same as in tritium scans anymore, thus it must be checked whether the results can be transferred.

To test the concept of magnetic field and electric potential determination based on krypton line scans, the K- and L_3-32 line is scanned in SAP 1 configuration. For the scan of the L_3-32 line the steep cone offsets are 40 V more positive, relative to the SAP 1 setting, for good transmission properties. In the analysis only statistical errors are considered, systematic uncertainties are not included. To compare to the simulation, the line width and position are fitted per pixel, assuming the simulated potential offsets and magnetic field values (see fig. 7.5). This results in four free parameters per pixel: normalization, background, line position and line width. The obtained line positions and widths for the K-32 and L_3-32 line are shown in fig. 7.8 and fig. 7.9, respectively. In both cases the line position shows a significant slope to lower energies with increasing pixel number. This points towards inaccuracies of the simulation with respect to the per-pixel retarding potential offsets. The shifted overall line position, which is about 2 eV above the previously measured value [57] points in the same direction. In contrast to the line position, the line widths are constant within the uncertainties as a function of pixel number. The absolute value of the widths are comparable to the previously measured ones of 2.77 eV and 1.15 eV for the K-32 and L_3-32 line [57], respectively. Hence no significant deviation from the simulated magnetic field values can be stated.

To quantify the deviation of the retarding potential offsets from the simulation, a second fit is performed. A single line position is fitted for all pixels together with per-pixel retarding potential offsets, normalization and background rate. Since the line width shows no pixel dependency, a single value is fitted for the whole detector. The obtained retarding potential offsets in comparison to the simulated ones are shown

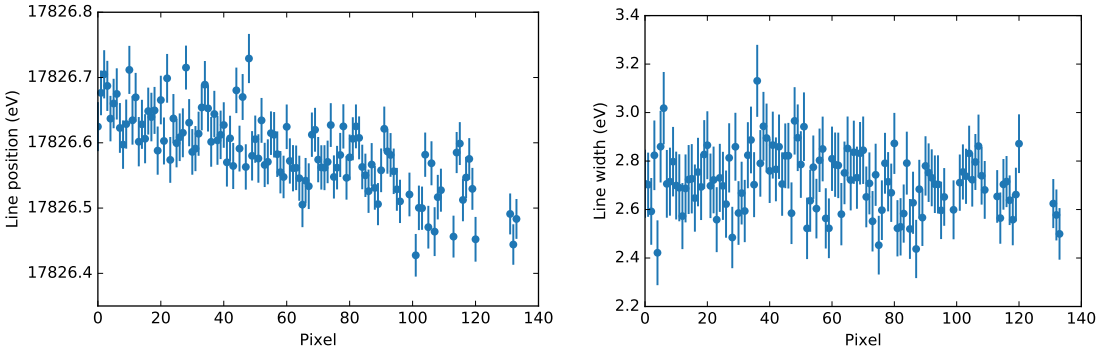

(a) K-32 line position

(b) K-32 line width

Figure 7.8: Fitted line position (a) and line width (b) of the K-32 line for each pixel in SAP 1 configuration. The fit is based on the simulated magnetic field and potential offsets.

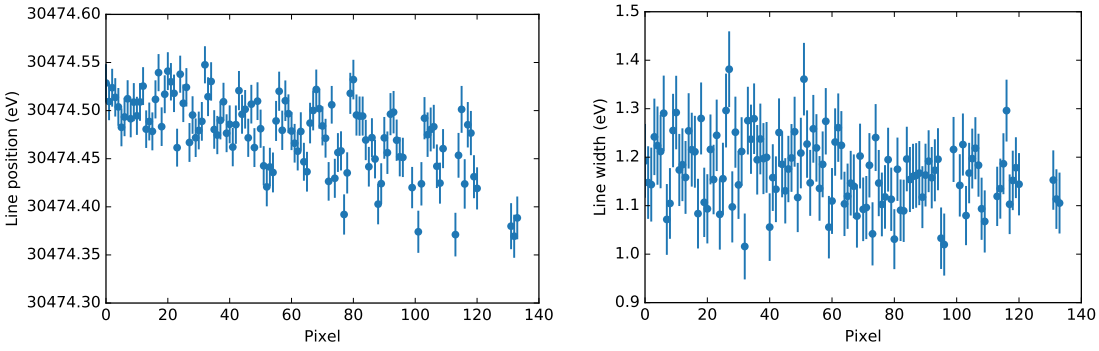

(a) L_3-32 line position

(b) L_3-32 line width

Figure 7.9: Fitted line position (a) and width (b) of the L_3-32 line for each pixel. The measurement configuration is similar to SAP 1 but adjusted for the transmission of 30 keV electrons. The fitted model is based on the simulated magnetic field and electric potential.

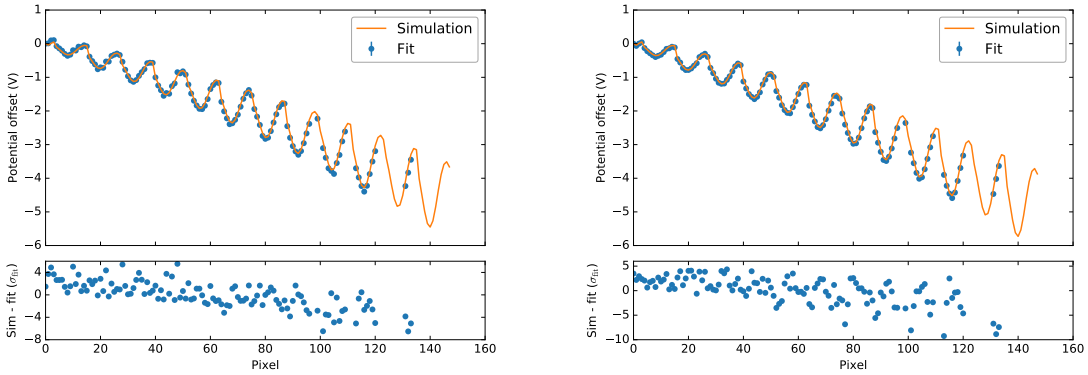

(a) K-32 line

(b) L_3-32 line

Figure 7.10: Fitted retarding potential offsets in comparison to the simulation for the K-32 line (a) and the L_3-32 line (b). They are shown relative to the offset on pixel 0.

in fig. 7.10 for both conversion electron lines. Like for the simulation and the tritium scans, the offsets are shown relative to the one on pixel 0. Significant deviations, strongly depending on the pixel number, up to $10\,\sigma_{\text{fit}}$ occur. In absolute numbers, observed differences are up to 0.16 V in case of the K-32 line and up to 0.12 V for the L_3-32 line. The discrepancy is potentially caused by the limited knowledge of alignment in this configuration. Later investigations in SAP configuration show that a shift of the detector position in the simulation reduces the deviations [133]. Compared to tritium, the uncertainties of the potential offsets determined with krypton, are with 0.028 to 0.023 V and 0.012 to 0.018 V for the K-32 and L_3-32 line, an order of magnitude smaller.

Summing up, krypton lines are well suited to determine the per-pixel retarding potential offsets and magnetic fields. Conclusions are possible even with a limited measurement time of 2.5 h per line due to the high rates provided by the krypton source. Within the uncertainty of the first test measurement no deviation of the magnetic field values can be stated. In addition to the determination of electric potential and magnetic field, the measurements can be used as calibration of alignment to improve accuracy of simulation.

7.4 KATRIN neutrino mass sensitivity with a Shifted Analyzing Plane

The SAP approach enables a significant reduction of the background rate. This configuration is accompanied by inhomogeneous magnetic fields and electric potentials in the analyzing plane, which requires their determination through dedicated measurements. Therefore, a greater degree of uncertainty can be expected compared to the normal neutrino mass measurement configuration. To investigate the impact of the inhomogeneities and the corresponding uncertainties on the neutrino mass, sensitivity studies are performed with the software Fitrium (see section 3.3.2).

As reference the sensitivity is calculated for a KNM1 like configuration with $B_{\text{ana}} = 6\,\text{G}$ in a centralized analyzing plane with negligible electric potential and magnetic field spread over the pixels. Two background rate cases are considered:

- 280 mcps over the whole detector: This rate is below the background rate observed in KNM1 and above the one measured directly after the spectrometer bake-out. It is estimated to be a realistic reference for next neutrino mass campaigns.
- 130 mcps over the whole detector: Expected background rate to be achieved by an optimized SAP configuration.

For the SAP a background rate of 130 mcps is assumed and two levels of inhomogeneity:

- $\mathrm{d}B = 7.0 - 5.2\ \text{G} = 1.9\,\text{G}$, $\mathrm{d}U = 3.4\,\text{V}$
- $\mathrm{d}B = 7.8 - 4.1\ \text{G} = 3.7\,\text{G}$, $\mathrm{d}U = 6.8\,\text{V}$.

These inhomogeneities are in the order of magnitude that is typically obtained when simulating such a configuration. Depending on whether the SAP is designed for maximal homogeneity or minimal background rate the level of inhomogeneity varies. For example the first listed configuration reflects a SAP configuration with very little inhomogeneity. For both considered SAP cases the mean analyzing plane magnetic field is the same, namely 6.3 G, which is comparable to the KNM1 setting. The course of the fields/potentials over the pixels is estimated from a simulation (misalignment neglected).

The final neutrino mass uncertainty, after a measurement time of 3 yr with full column density of $5 \cdot 10^{21}\,\text{m}^{-2}$, is calculated for the above configurations. A fit range of $E_0 - 30\,\text{eV}$ is assumed and the same measurement time distribution as employed during KNM1. This measurement time distribution is most likely not perfect for a SAP setting, due to the spread in electric potential. Therefore the

optimized measurement time, especially in the most sensitive region for the neutrino mass, where most of the time is spent, matches only for pixels with small potential deviations. The pixels where the potential is highly shifted measure in this region for a much shorter time. To prevent an overall shift with respect to the measurement time distribution, the electric potential variations are implemented such that their mean over all pixels is zero. Furthermore two analysis strategies are considered, the uniform and multi-ring fit.

7.4.1 Uniform fit

For the uniform fit, which was used for the analysis of KNM1, the measured counts at the individual pixels are combined to one single β-spectrum. A single endpoint, neutrino mass, background and normalization is fitted to this spectrum. For the fit the transmission functions of the individual pixels are averaged. In case of negligible inhomogeneity in magnetic fields and electric potential such averaging has minor impact. However, if there are significant differences in the analyzing plane fields over the pixels, the averaging of transmission functions results in a broadening. The broadening is visualized in fig. 7.11, where the resulting transmission function for a 6 G setting with negligible inhomogeneity as well as for the two investigated SAP configurations is shown. Although all configurations have about the same mean analyzing plane magnetic field, the transmission functions of the SAP settings are significantly broader. Effectively, the settings with field variations within pixels have a poorer spectrometer resolution. This is a consequence of averaging transmission functions that are shifted in energy and of different widths caused by the spread of retarding potentials and magnetic fields over the individual pixels. Note that by averaging the transmission function over all pixels, the inhomogeneities within one pixel are already included.

The impact of the transmission function's shape on the $1\,\sigma$-uncertainty of the observable m_ν^2 is visible in fig. 7.12. Each bar corresponds to one of the investigated cases. The statistical uncertainty is visualized in blue. Given a standard 6 G configuration, the neutrino mass squared uncertainty is significantly improved, from $0.053\,\mathrm{eV}^2$ to $0.044\,\mathrm{eV}^2$, when the background is reduced from 280 mcps to 130 mcps. Assuming such a reduction is realized by a SAP configuration, the achievable sensitivity depends on the accompanied inhomogeneity. Considering the case with $\mathrm{d}B = 1.9\,\mathrm{G}$, $\mathrm{d}U = 3.4\,\mathrm{V}$, there is still improvement in statistical uncertainty compared to 280 mcps without inhomogeneity. However, the sensitivity is worse compared to 130 mcps without inhomogeneity. For the SAP configuration with higher field and potential spread, the broadened transmission outbalances the gain of the reduced background rate. The statistical uncertainty becomes worse than in standard

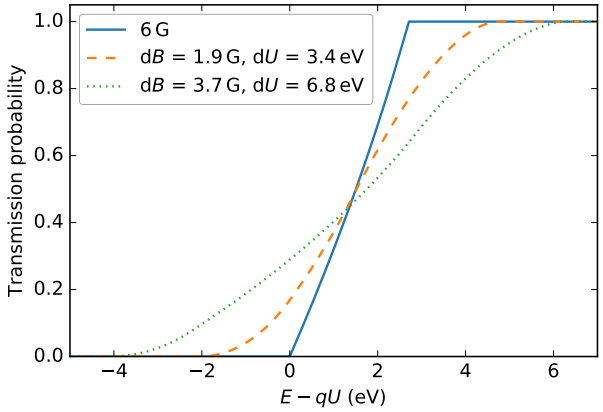

Figure 7.11: Averaged transmission function over all detector pixels for a homogeneous 6 G setting and the two studied SAP configurations.

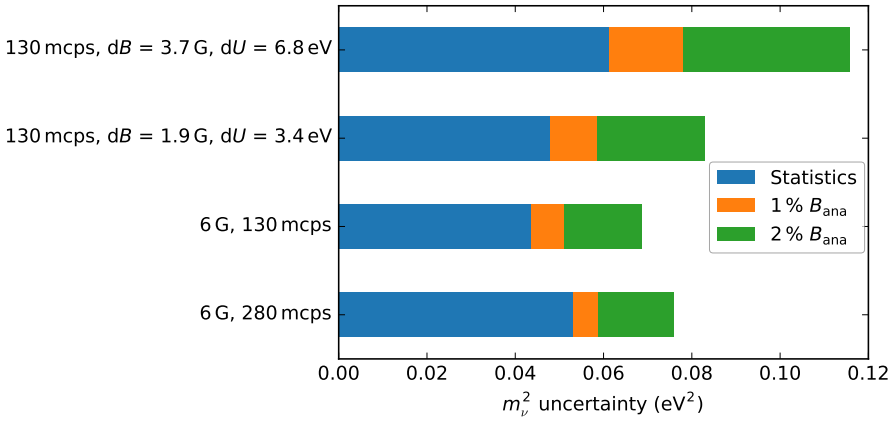

Figure 7.12: Neutrino mass squared uncertainty ($1\,\sigma$) for a uniform analysis and a measurement time of 3 yr. The lower two bars correspond to the nominal KNM1 setting under the assumption of two different background levels. The upper two bars correspond to the two SAP configurations.

configuration with elevated background.

Especially in case of the SAP, systematic uncertainties arising from imperfect knowledge of the analyzing plane properties can not be neglected since they are expected to be larger than for the standard configuration. In case of KNM1 the analyzing plane magnetic field uncertainty is 1 % and there is negligible uncertainty on the retarding potential value. For the uniform analysis the magnetic field uncertainties are included with a Covariance matrix (see section 3.3.2), where the magnetic field is varied at all pixels according to the assumed systematic uncertainty. Assuming this uncertainty budget, the uncertainty on the neutrino mass squared is increased, as shown by the orange bars. Under those conditions the SAP configuration with low inhomogeneities has a comparable uncertainty as the standard configuration at elevated background. However for the SAP a magnetic field uncertainty at least as big as in the nominal configuration is expected, because the simulation is more sensitive to alignment and is dependent on experimental validation. Increasing the magnetic field uncertainty to 2 %, indicated in green, results in a much worsened sensitivity of the SAP settings compared to the 6 G configuration. The worse sensitivity becomes even more pronounced for the SAP configuration with $\mathrm{d}B = 3.7\,\mathrm{G}$, $\mathrm{d}U = 6.8\,\mathrm{V}$. In principle uncertainties on the electric potential also need to be considered. However systematically wrong determined potential offsets causing an overall shift will be absorbed by the fitted endpoint or qU-offset. Statistical variations of the measured per-pixel potentials will average out in the averaged transmission function and hence not affect the sensitivity. Hence the neutrino mass uncertainty is predominantly affected if the determined potentials as a function of pixel number are tilted with respect to the truth, which affects the width of the transmission function similar to a magnetic field uncertainty. Hence no separate systematic uncertainty on the electric potential offsets is assumed.

When employing a uniform fit analysis, a background reduction through a SAP is only beneficial in terms of neutrino mass uncertainty when the introduced inhomogeneities in the analyzing plane are reduced to a very small level. In addition accompanied systematic uncertainties from inaccurate determination of analyzing plane properties need to be reduced. Already with a magnetic field uncertainty of 1 % the gain in neutrino mass uncertainty through the reduced background is counteracted.

7.4.2 Multi-ring fit

The SAP approach with an uniform fit is only advantageous under strict criteria on the inhomogeneity and its uncertainty. This is due to the broadening of the transmission function. Through an analysis, where the transmission is not averaged

over the whole detector, the impact of broadening can be reduced. A suitable analysis would be a multi-pixel or multi-ring fit. For such fits the measured counts within one detector pixel or ring are combined to one spectrum. The resulting spectra are fitted by evaluating a single likelihood function with a common endpoint and neutrino mass and a ring-/pixel-wise background and normalization. For more details on this method see [46]. In this fit a separate transmission function is used for each detector ring or pixel. This way the transmission function is not as broadened as in the uniform analysis. In case of a SAP configuration a slight widening of the individual transmission functions still occurs due to the inhomogeneity in the fields/potentials within one ring or pixel. Neglecting the experiment's misalignment, the electric potentials and magnetic fields are radially symmetric without azimuthal dependence. Therefore there is no benefit of a pixel-wise analysis compared to a per-ring analysis. Hence the latter is employed for the presented neutrino mass sensitivity calculations.

The ring-wise transmission functions for the 6 G and the studied SAP configuration of low inhomogeneity are shown in fig. 7.13. They are plotted as a function of ring-wise surplus energy such that the shift of transmission functions, due to the different retarding potential offsets, is not visible. Compared to the standard configuration, there is a large ring-wise spread in the SAP transmissions due to the different analyzing plane magnetic fields and the present ring-wise inhomogeneities. Depending on the ring, the corresponding spectrometer resolution is worse or improved compared to 6 G.

Employing a multi-ring analysis results in the uncertainties on the neutrino mass squared depicted in fig. 7.14. The same four cases as for the uniform analysis are shown. Unlike for the uniform analysis the statistical uncertainty is not worsened with the two SAP configurations. This is because the transmission function is no longer averaged over all pixels, but only over the fields/potentials present within one ring[2], which produces a much smaller variation than over the whole detector. Aside from the inhomogeneity within one ring, the statistical uncertainty is also affected by the magnetic field and electric potential distribution over the detector rings, leading to slightly different values for the two studied SAP configurations. Including a systematic uncertainty on the analyzing plane magnetic field nevertheless reveals again a strong dependence on the inhomogeneities. In case of the multi-ring analysis, uncertainties are included with the MC propagation (see section 3.3.2). For the studied SAP configuration of large inhomogeneity ($\mathrm{d}B = 3.7\,\mathrm{G}$, $\mathrm{d}U = 6.8\,\mathrm{V}$) the impact of the magnetic field uncertainty is highly increased compared to more homogeneous settings. However, SAP configurations of moderate field and potential

[2] In case of axial-symmetric potentials and magnetic fields the inhomogeneity is the same for all pixels within one ring.

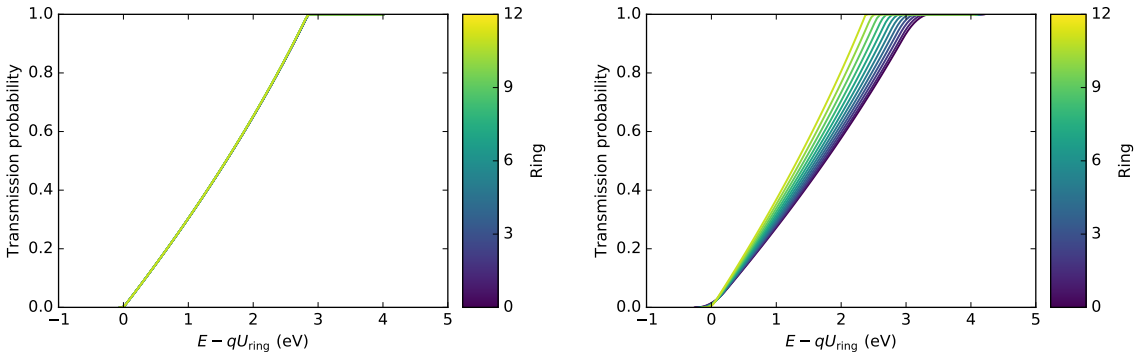

(a) 6 G (b) SAP

Figure 7.13: Transmission functions for the individual FPD rings for the nominal 6 G configuration (a) and the SAP configuration with $\mathrm{d}B = 1.9\,\mathrm{G}$, $\mathrm{d}U = 3.4\,\mathrm{V}$ (b). The absolute shift of the transmission due to the radial dependent retarding potential, especially in case of the SAP, can not be seen since the transmission probability is shown as a function of ring dependent surplus energy.

spread improve the neutrino mass squared uncertainty compared to the one with 280 mcps background rate as long as they do not suffer from an increased analyzing plane magnetic field uncertainty compared to the standard configuration. Assuming a 1 % magnetic field uncertainty for the nominal and the SAP setting, the SAP can improve the neutrino mass squared uncertainty by 18 %. In terms of neutrino mass uncertainty an improvement of 9 % can be achieved.

Above studies show that the achievable neutrino mass uncertainty depends on the transmission function properties. To investigate further how a magnetic field or electric potential inhomogeneity affects the sensitivity at a background level of 130 mcps an additional study is performed, where magnetic field and potential inhomogeneity are considered separately. For this purpose one pixel is assumed with a certain spread of potential or field and the resulting uncertainty on m_ν^2 is calculated. The neutrino mass squared uncertainty for three different analyzing plane magnetic fields as a function of field inhomogeneity is shown in fig. 7.15(a). In the pixel the magnetic field ranges from B_{ana} to $B_{\text{ana}} + \Delta B$. Considering statistical uncertainty, only minor impact of the magnetic field spread is visible. However, when a 1 % uncertainty on the magnetic field is added, a significant dependence appears. The m_ν^2 uncertainty is more affected with increasing spread of magnetic field. This increase is more prominent for large analyzing plane magnetic fields. Hence the magnetic field accuracy is especially relevant for larger analyzing plane magnetic fields.

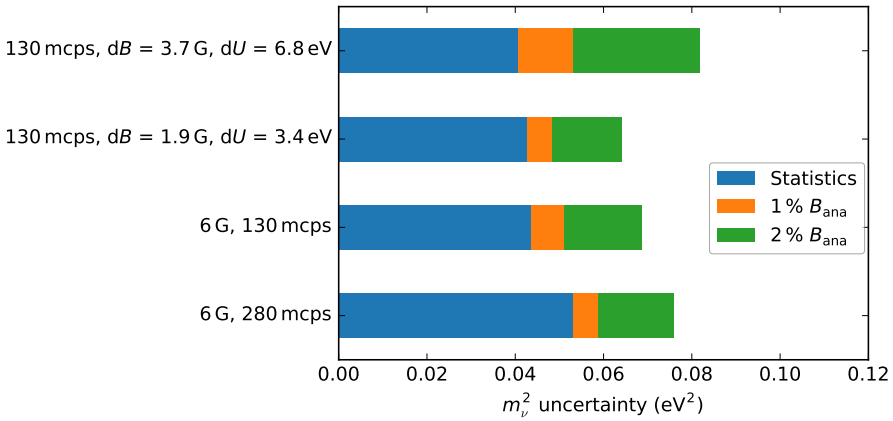

Figure 7.14: Uncertainty on the neutrino mass squared m_ν^2 when employing a multi-ring analysis for two SAP configurations in comparison to the standard 6 G configuration.

A similar study is performed assuming an electric potential inhomogeneity within one pixel. Considering the case of $\mathrm{d}U = 2\,\mathrm{V}$ the voltage within the pixel ranges from $-\frac{\mathrm{d}U}{2}$ to $+\frac{\mathrm{d}U}{2}$, to prevent an overall shift with respect to the measurement time distribution. Figure 7.15(b) shows the neutrino mass squared uncertainty as a function of potential inhomogeneity for two different analyzing plane magnetic fields. A significant dependence on the voltage spread is visible due to the broadening of the transmission function. This trend is the same for both considered analyzing plane magnetic fields.

For comparison, the m_ν^2 uncertainty in standard 6 G configuration with a background rate of 280 mcps and no inhomogeneity is $0.053\,\mathrm{eV}^2$ considering statistics only and $0.059\,\mathrm{eV}^2$ when a 1 % magnetic field uncertainty is included (see fig. 7.14). Neglecting systematics, the achievable uncertainty is better than with high background even with a per-pixel inhomogeneity of $\mathrm{d}B = 3\,\mathrm{G}$ or $\mathrm{d}U = 5\,\mathrm{V}$. Including a magnetic field uncertainty of 1 %, the improvement with respect to the elevated background case depends on the analyzing plane magnetic field and the inhomogeneity. With better energy resolution for instance through $B_\mathrm{ana} = 3\,\mathrm{G}$, the neutrino mass uncertainty is improved even with a spread of 3 G (also when comparing to the statistical uncertainty with elevated background). Given 5 G magnetic field in the analyzing plane and a field spread of 3 G, the m_ν^2 uncertainty is still improved compared to the case of elevated background (but worse when comparing to the statistical uncertainty with elevated background). At a magnetic field of 6 G the lowered background at cost of a magnetic field inhomogeneity is outbalanced with $\mathrm{d}B = 3\,\mathrm{G}$. Since the combination of electric potential and magnetic field inhomogeneity worsens the energy resolution more than either of them separately, the gain in neutrino mass uncertainty through the lowered background is not outbalanced only when the per-pixel spread

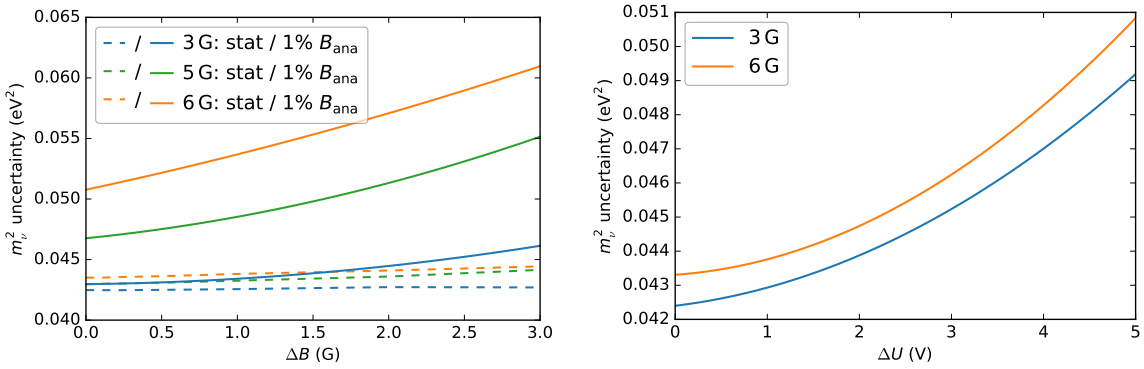

(a) Magnetic field

(b) Electric potential

Figure 7.15: Neutrino mass uncertainty for different analyzing plane magnetic fields as a function of magnetic field inhomogeneity (a) and spread of electric potential (b).

of magnetic field reaches 3 G. Therefore, when a SAP configuration is designed, two aspects need to be considered:

- Minimal inhomogeneity in magnetic field and electric potential to reduce impact of magnetic field uncertainties
- Low analyzing plane magnetic field for good energy resolution which improves the neutrino mass sensitivity and lowers the impact of magnetic field uncertainties.

7.5 Conclusion

A promising approach to reduce the background is a change of visible flux volume achievable through a SAP. Measurements show that this method can reduce the background rate by more than a factor of two. However, this approach is accompanied by a strong variation of electric potential and magnetic field within the analyzing plane. Carried out sensitivity studies show that the variations need to be taken into account in a multi-ring analysis in order to benefit from the reduced background rate. In addition the analyzing plane properties need to be known at least to the same level of precision as in the standard configuration. Especially for large analyzing plane magnetic fields, the corresponding uncertainty is of high relevance for the achievable neutrino mass uncertainty. Therefore SAP configurations should be designed with the smallest possible inhomogeneity. In addition low magnetic fields in the analyzing plane are preferred since they are less sensitive with respect to field uncertainties. The

studied example SAP configuration with low inhomogeneities enables an improvement of the neutrino mass squared uncertainty by 18 % compared to standard measurement settings. Since the SAP configuration is due to its inhomogeneity more sensitive with respect to the experiment's alignment, simulations need to be verified by measurements for a precise characterization. Several approaches are available within KATRIN, for instance ^{83m}Kr. In case of krypton, the line width and position of the electron conversion lines can be used to determine the electric potential as well as the magnetic field in the analyzing plane. First test measurements show a high sensitivity to the retarding potentials in the analyzing plane even with a short measurement time. Furthermore, electron gun measurements allow for an independent measurement of the electric potential of the analyzing plane. Further measurements are planned to validate the simulations and to guarantee a high accuracy.

8 Summary

In the presented work, the background in the KATRIN **m**ain **s**pectrometer was examined with regard to its origin, characteristics and mitigation. Currently the background rate is more than one magnitude above the technical design value of 10 mcps. Hence a mature strategy to reduce the background rate is essential to achieve the experiment's goal, which requires a precise knowledge of the background's origin. The background predominantly consists of three components: detector background, radon-induced background and the so-called Rydberg background, which is the most dominant part. According to the Rydberg model this background is created through radioactive decays on the spectrometer surface, in particular α-decays. Through a sputtering process highly excited atoms, Rydberg atoms, are emitted that contribute to the background when they are ionized within the magnetic flux volume. Within this thesis dedicated measurements were carried out at the KATRIN **m**ain **s**pectrometer to characterize and validate the Rydberg background. First, measurements with various electromagnetic field settings of the spectrometer allowed to determine the energy distribution of background electrons. Secondly, a measurement with a radioactive radium source installed at the spectrometer was used to imitate the background and to verify that radioactive decays in the spectrometer walls depict the origin of the observed background.

The background electron energy spectrum measurement revealed significant contributions from electrons above 100 meV. Those energies are larger than expected from ionization of Rydberg atoms by **b**lack-**b**ody **r**adiation. A possible explanation could be that a sizable amount of Rydberg atoms is ionized via the process of autoionization, which yields higher energy electrons up to 2 eV.

The correlation between spectrometer surface activity and background rate was investigated by inserting the α-source ^{223}Ra into the **m**ain **s**pectrometer. Carried out measurements show, that the background rate in the spectrometer volume is highly correlated with the induced activity on the surface. In addition, the artificially induced background exhibits the same dependence on the **I**nner **E**lectrode voltage as the normal spectrometer background. These results are strong indications that the **m**ain **s**pectrometer background is caused by radioactive decays at the surface.

In this thesis, the relevant background parameters, such as fraction of non-Poisson background, upper limit on the retarding potential dependence of the background as well as stability of the background rate were provided for the final fit of the first neutrino mass campaign of KATRIN. Moreover, the measurement time distribution of the first neutrino mass campaign in the background region, i.e. the region above the spectral endpoint, was optimized with respect to maximizing the statistical sensitivity and minimizing background-related systematic effects.

As an approach to mitigate the elevated background, the **S**hifted **A**nalyzing **P**lane method is investigated. This method decreases the background rate through a reduction of visible magnetic flux volume. Within the framework of this thesis first test measurements were carried out and the resulting neutrino mass uncertainty was calculated. Background measurements in **S**hifted **A**nalyzing **P**lane configuration enabled a rate reduction by more than a factor of two. Nevertheless the **S**hifted **A**nalyzing **P**lane settings are accompanied by inhomogeneities of the magnetic fields and electric potentials which need to be taken into account in the spectral analysis. Carried out studies show that the neutrino mass uncertainty is improved as long as the induced inhomogeneities are reduced to a minimum and systematic uncertainties remain the same as with a central analyzing plane. The later can be achieved through a precise measurement of the analyzing plane magnetic fields and electric potentials. Promising in this regard is a characterization with the electron gun and ^{83m}Kr.

In summary, this thesis provided essential insights to the understanding of the background in the KATRIN experiment. The results of this thesis will be of key importance for the development of future means to further mitigate the background. In the framework of this thesis major contributions were made to the first neutrino mass result of KATRIN: The key background model parameters were provided for the final fit and prior to the data taking the measurement time distribution in the background region was optimized. Finally, a novel concept to reduce the background, the so-called **S**hifted **A**nalyzing **P**lane, was tested for the first time in this thesis.

A Appendix

A.1 Overview of KASPER tools

The software KASPER comprises the following tools:

- **Kommon**: Libraries for basic functionality such as reading/writing files, physical and mathematical constants, mathematical elements like numerical integrators.
- **KGeoBag**: Geometry definitions for navigation of particle trajectories.
- **KEMField**: Library for the computation of electromagnetic potentials and fields.
- **Kassiopeia**: Particle tracking MC simulation.
- **Beans**: Analysis and readout of data, in particular of the FPD, supporting near and real-time analysis.
- **KaLi**: Data library to access slow-control and run data on the database.
- **KaFit**: Fitting tool, also used to investigate systematics and their impact on neutrino mass sensitivity.
- **SSC**: Tool for source modeling and calculation of differential and integral beta decay spectra of gaseous tritium.
- **KSC**: KATRIN specific code, e.g. geometries.
- **KTrap**: Program for analysis and simulation of transmission properties.
- **IDLE**: Intermediate Data Layer, a shared file storage.
- **Kess**: Simulation code to track electrons in silicon and simulate their energy deposition.
- **Keloss**: Tool to determine the electron energy loss function.
- **Tabree**: Table and tree structure.

- **Kebap**: General syntax parsing engine.

A.2 Settings for sensitivity shown in fig. 3.9

Shown signal amplitudes and sensitivities are computed based on the KNM1 measurement configuration:

- Background rate constant in time and independent of qU
- $B_{\text{Pinch}} = 4.2\,\text{T}$
- $B_{\text{Source}} = 2.5\,\text{T}$
- $B_{\text{min}} = 6\,\text{G}$
- $\rho d = 5 \cdot 10^{21}\,\text{m}^{-2}$
- 95 % of T_2, 4 % HT, 1 % DT.

As measurement time distribution the so-called Isostat is used [47], shown in fig. A.1, with 15 % time above the tritium endpoint in the background region. The time per retarding potential is based on the statistics in the tritium spectrum. For improved neutrino mass sensitivity the time in the most sensitive region with respect to a non-zero mass is increased (neutrino boost). Since this region depends on the background level the measurement time distribution is adjusted for the different rates. Both, sensitivities and background rates, refer to the whole detector, no pixels are excluded.

A.3 Run list for background evolution

The inputs for fig. 4.16 are listed in table A.1. For fig. 4.17 the following runs are analyzed:

- October 2017: reference background run 34537, electric dipole run 34538
- February 2019: reference background run 47451, electric dipole runs 47452 - 47455

campaign	FPD run number	IE voltage (V)	flux volume (m^3)

SDS-II	24696 - 24699	-100	576
	24700 - 24717	-100	818
	24718 - 24722	-100	576
	24765 - 24775	-100	818
	25705 - 25720	-100	818
SDS-III	30209 - 30212	0	616
	30224 - 30240	0	613
	33637 - 33654	-100	686
	33655 - 33677	-100	806
	33859 - 33953	-100	806
	35023 - 35030	-200	391
	35116 - 35123	-200	391
	35356 - 35360	-200	391
	35426 - 35430	-200	391
	35517 - 33539	-200	391
FT	40004 - 40007	-200	391
	40089 - 40105	-200	391
	40366 - 40381	-200	391
	41078 - 41084	-200	391
STS3a	43694	-200	391
	44167	-200	391
	46884 - 46888	-200	391
KNM1	47417	-200	391
	50992 - 50995	-200	391
	54717	-200	391
	54817 - 54820	-200	391
KNM2	54843 - 54849	-200	391
	56480 - 56483	-200	391

Table A.1: Input for background evolution overview fig. 4.16: Run numbers, IE voltages and computed flux volumes for the different measurement configurations. In addition to the voltage the data sets differ in maximal magnetic field (B_{Pinch}), minimal magnetic field (B_{ana}) and PS magnet currents. Flux volumes are determined based on Kassiopeia simulations.

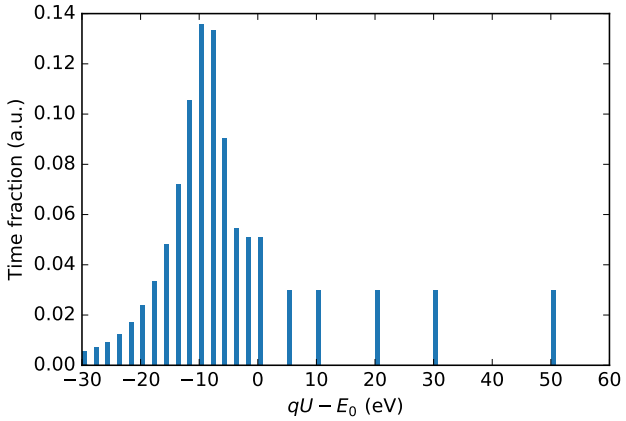

Figure A.1: Fraction of measurement time at the different retarding potentials relative to the tritium endpoint. 15 % of the time is spent in the background region. To improve the neutrino mass sensitivity most measurement time is foreseen in the most sensitive region.

A.4 Run list for background electron energy determination

Runs for evaluation of the voltage dependency of the background rate are listed in table A.2. Magnetic trapping measurements are specified in table A.3. For all runs with dipole pulse the same sequence is employed, 1 s dipole pulse and 4 s without dipole field. Runs performed for electric trapping investigations are enumerated in table A.4.

A.5 Relaxation of stored particle background

The electric dipole pulse removes stored electrons from the MS. If such electrons exist a rate reduction is observed. After a certain time the background rate is expected to recover. To determine the rate after removal of stored particles it is important that the dipole pulses are applied frequently enough such that no rate relaxation occurs. In the performed measurements for the energy spectrum determination the pulse is repeated every 5 s. A separate measurement with 299 s between the pulses is performed to determine when the rate actually starts to relax. This measurement is performed at a retarding voltage of −1.1 kV and a magnetic field of $B_{\text{ana}} = 3.8\,\text{G}$. The former is chosen since a significant rate reduction is observed in this configuration such that a potential background relaxation would be clearly visible. Although the magnetic field in the analyzing is the same as in measurements presented within

U_{vessel} (kV)	U_{IE} (V)	B_{ana} (G)	run number
-18.5	-100	3.8	34537
-7	-100	3.8	34539
-5	-100	3.8	34541
-3	-100	3.8	34543
-1	-100	3.8	34545
-0.5	-100	3.8	34547
-18.5	-100	1.9	34536
-5	-100	1.9	34535
-3	-100	1.9	34534
-2	-100	1.9	34532
-1	-100	1.9	34530
-0.5	-100	1.9	34529
-18.5	-100	9	34519
-5	-100	9	34520
-3	-100	9	34521
-2	-100	9	34523
-1	-100	9	34525
-0.5	-100	9	34527

Table A.2: Run list for the high voltage dependency shown in fig. 5.10. The measurements were performed within SDS-III with $B_{\text{PCH}} = B_{\text{PS2}} = 4.2\,\text{T}$ and $B_{\text{PS1}} = 0\,\text{T}$.

U_{vessel} (kV)	U_{IE} (V)	B_{ana} (G)	run number reference	run number dipole pulse
-18.5	-100	3.8	34537	34538
-7	-100	3.8	34539	34540
-5	-100	3.8	34541	34542
-3	-100	3.8	34543	34544
-1	-100	3.8	34545	34546
-0.5	-100	3.8	34547	34548
-2	-100	1.9	34532	34533
-1	-100	1.9	34530	34531
-3	-100	9	34521	34522
-2	-100	9	34523	34524

Table A.3: Run list for magnetic trapping measurements shown in fig. 5.11 and fig. 5.5. All measurements were performed within SDS-III with $B_{\text{PCH}} = B_{\text{PS2}} = 4.2\,\text{T}$ and $B_{\text{PS1}} = 0\,\text{T}$.

central electrode offset (V)	run number
0	35236
0.3	35237
0.6	35238
1	35239
1.5	35240
2	35241
2.5	35242
3	35243
4	35244
6	35245

Table A.4: Run list for electric trapping measurements presented in section 5.1.4. The measurements were performed within SDS-III with $B_{\mathrm{PCH}} = B_{\mathrm{PS2}} = 4.2\,\mathrm{T}$ and $B_{\mathrm{PS1}} = 0\,\mathrm{T}$. The retarding potential is constant at $U_{\mathrm{ret}} = 18.6\,\mathrm{keV}$.

section 5.1.5 the rates can not be directly compared due to different configurations of superconducting magnets. In the here presented background rate relaxation study, the magnets are set to $B_{\mathrm{PCH}} = 4.2\,\mathrm{T}$, $B_{\mathrm{PS2}} = 3.1\,\mathrm{T}$ and $B_{\mathrm{PS1}} = 0\,\mathrm{T}$. Applied cuts are the same as in section 5.1.5, only rings 0 to 4 are considered. The result of this measurement is shown in fig. A.2. Due to the limited time of 1 h for the reference background (run number: 34495) and 4 h with electric dipole (run number: 34496) the error bars are rather large. Nevertheless the measurement fulfills its purpose. In the first about 70 s after the dipole pulse, the rate is clearly reduced with respect to the reference. Afterwards an increase in rate is observed, reaching the nominal level after about 200 s. The increase can be described by the exponential function

$$R(t) = A \cdot (1 - e^{-\frac{t}{\tau}}) \tag{A.1}$$

as expected for stored particles. A denotes the amplitude and τ the time constant. A fit of this function to the data after 70 s provides good agreement. The fit result gives:

- $A = (109.3 \pm 5.2)\,\mathrm{mcps}$
- $\tau = (56.5 \pm 12.0)\,\mathrm{s}$
- $\chi^2/\mathrm{ndof} = 0.64$.

Given that the relaxation of background starts only after more than one minute after the dipole pulse, a repetition every 4 s is more than sufficient.

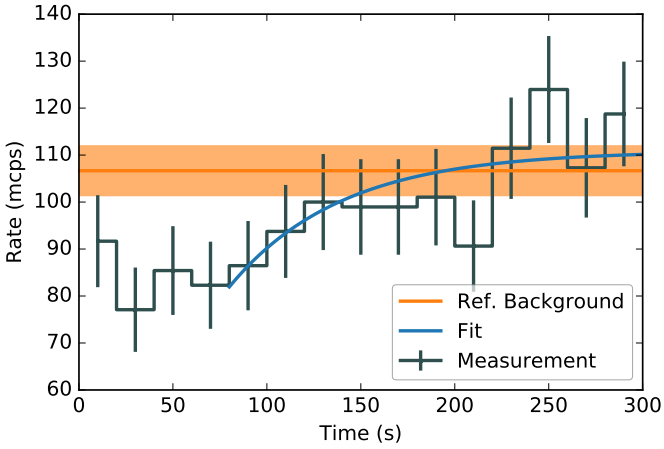

Figure A.2: Background rate in 299 s after application of the dipole pulse for 1 s. The time fraction with active dipole field is included within the first bin. Normal background in this configuration is indicated by the orange line. After about 70 s the rate starts to relax back to reference background level.

A.6 Impact of high voltage PR on electric dipole measurements

In measurements performed with the electric dipole pulse to determine the background electrons energy spectrum the high voltage PR was not available yet. To investigate whether thereby present high voltage fluctuations impact the storing of particles or the effect of the electric dipole, measurements are performed at later stage with and without PR. Results of those investigations are shown in fig. A.3. The relative rate reduction for three spectrometer resolutions is shown, each once with and once without active PR. Within the statistical uncertainties no impact of high voltage fluctuations is visible.

A.7 Run list of ^{223}Ra measurements

The analysis of the measurements is based on the FPD runs listed in table A.5.

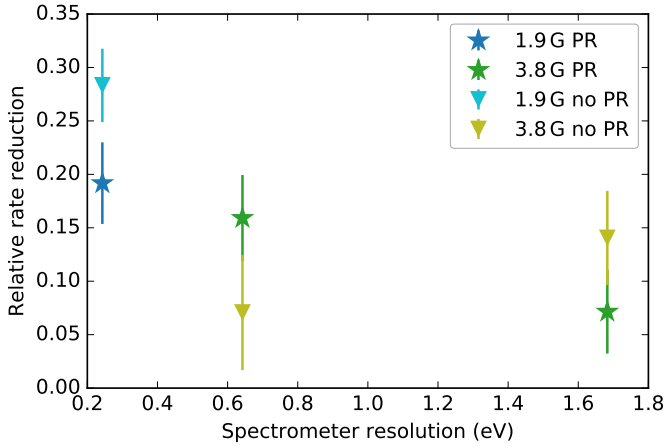

Figure A.3: Relative rate reduction obtained after reduction of stored particles via an electric dipole pulse for three spectrometer resolutions. Within their statistical uncertainties no impact of the high voltage PR is present.

Measurement	**Run numbers**
Reference asymmetric magnetic fields	44146
Accumulation of surface activity	44148 - 44155
Decay surface	43739 43741 43743 43745 43747 43749 43751 43753 43755 43757 43759 43761 43763
Decay volume	43738 43740 43742 43744 43746 43748 43750 43752
Inner electrode dependency	44159 (200V), 44160 (20V), 44161-44164 (0V)
Reference for inner electrode dependency	44143 (200V), 44144 (20V), 44145 (0V)
Radial dependency source	43738 43740 43742
Radial dependency reference	44145

Table A.5: List of runs used for analysis of the measurements with the ^{223}Ra source.

A.8 Run list of retarding voltage dependency investigations

The FPD run numbers for the background measurements carried out in different potential configuration (see section 5.3.1) are listed in table A.6. Studies on the impact of non-axial electric fields (see section 5.3.2) are performed on the runs depicted in table A.7.

potential configuration	run numbers
symmetric	34509 - 34515
asymmetric	34501 - 34507
blocking	34516, 34517

Table A.6: Corresponding FPD runs of the measurements presented in fig. 5.22.

configuration	U_{IE} (V)	run numbers
no offsets	-10	35210 - 35213
positive SC and APE offsets	-10	35202-35204, 35218
no offsets	-50	35214 - 35217
positive SC and APE offsets	-50	35206, 35207, 35209
east dipole, no offsets	-50	35246, 35247
west dipole, no offsets	-50	35252, 35253
west dipole, SC offset	-50	35254, 35255

Table A.7: Corresponding FPD runs of the measurements presented in figs. 5.26 and 5.27.

A.9 Configuration of SAP 1 and SAP run numbers

Magnetic field and potential configuration:

- Aircoil currents from coil 1 to coil 14: 100, 100, 120, 120, 120, 120, 120, 120, 70, 70, 70, 80, 20 and −70
- Earth magnetic field compensation coils: 45 and 0 (vertical/horizontal)
- IE common: −220 V
- Upstream steep cones: 180 V
- Upstream flat cones: 180 V
- Central electrodes: 35 V
- Downstream large flat cone: 20 V
- Downstream middle flat cone: 15 V
- Downstream small flat cone: 30 V
- Downstream steep cones: 35 V (comb), 120 V (fulmetal); 160 V (fulmetal) for the L-line

Run numbers:

- Reference background: 51995
- Tritium scan: 51998, 52 012 to 52 017
- Krypton K-line: 54 311 to 54 328
- Krypton L-line: 54 329 to 54 354

Bibliography

[1] W. Pauli. Offener Brief an die Gruppe der Radioaktiven bei der Gauvereins-Tagung zu Tübingen, 1930. URL https://cds.cern.ch/record/83282/files/meitner_0393.pdf.

[2] C. L. Cowan et al. Detection of the free neutrino: a confirmation. *Science*, 124(3212):103–104, 1956. ISSN 0036-8075. doi: 10.1126/science.124.3212.103. URL https://science.sciencemag.org/content/124/3212/103.

[3] Q. R. Ahmad et al. (SNO Collaboration). Measurement of the rate of $\nu_e + d \rightarrow p + p + e^-$ interactions produced by ^8B solar neutrinos at the sudbury neutrino observatory. *Phys. Rev. Lett.*, 87(7), 2001. doi: 10.1103/PhysRevLett.87.071301. URL https://journals.aps.org/prl/abstract/10.1103/PhysRevLett.87.071301.

[4] J. Angrik et al. (KATRIN Collaboration). KATRIN design report 2004. Technical report, 2005. URL https://www.katrin.kit.edu/publikationen/DesignReport2004-12Jan2005.pdf.

[5] M. Kaplinghat et al. Determining Neutrino Mass from the Cosmic Microwave Background Alone. *Phys. Rev. Lett.*, 91:241301, Dec 2003. doi: 10.1103/PhysRevLett.91.241301. URL https://link.aps.org/doi/10.1103/PhysRevLett.91.241301.

[6] C. Hall (EXO Collaboration). EXO: A Next generation double beta decay experiment. In *4th Workshop on Neutrino Oscillations and their Origin (NOON2003)*, pages 332–337, 2 2003. URL https://s3.cern.ch/inspire-prod-files-e/e62671dfe96994da849295331acf99eb.

[7] C. Kraus et al. Final results from phase II of the Mainz neutrino mass search in tritium β decay. *Eur. Phys. J. C*, 40(4):447–468, Apr 2005. ISSN 1434-6052. doi: 10.1140/epjc/s2005-02139-7. URL https://link.springer.com/article/10.1140/epjc/s2005-02139-7.

[8] V. N. Aseev et al. Upper limit on the electron antineutrino mass from the Troitsk experiment. *Phys. Rev. D*, 84:112003, Dec 2011. doi: 10.1103/PhysRevD.84.112003. URL https://link.aps.org/doi/10.1103/PhysRevD.84.112003.

[9] G. Danby et al. Observation of high-energy neutrino reactions and the existence of two kinds of neutrinos. *Phys. Rev. Lett.*, 9:36–44, Jul 1962. doi: 10.1103/PhysRevLett.9.36. URL https://link.aps.org/doi/10.1103/PhysRevLett.9.36.

[10] K. Kodama et al. (DONUT collaboration). Observation of tau neutrino interactions. *Phys. Lett. B*, 504:219–224, 2001. doi: 10.1016/S0370-2693(01)00307-0. URL https://www.sciencedirect.com/science/article/abs/pii/S0370269301003070?via%3Dihub.

[11] W.-M. Yao et al. (Particle Data Group). Number of neutrino types. *J. Phys. G*, 33, 1, (2006) and 2007 partial update for edition 2008. URL http://pdg.lbl.gov/2007/listings/s007.pdf.

[12] M. Goldhaber et al. Helicity of neutrinos. *Phys. Rev.*, 109:1015–1017, Feb 1958. doi: 10.1103/PhysRev.109.1015. URL https://link.aps.org/doi/10.1103/PhysRev.109.1015.

[13] R. Davis Jr. et al. Search for neutrinos from the sun. *Phys. Rev. Lett.*, 20, 1205, 1968. doi: 10.1103/PhysRevLett.20.1205. URL https://journals.aps.org/prl/abstract/10.1103/PhysRevLett.20.1205.

[14] B. Pontecorvo. Mesonium and Antimesonium. *Soviet Journal of Experimental and Theoretical Physics*, 6:429, 1958.

[15] B. Pontecorvo. Neutrino Experiments and the Problem of Conservation of Leptonic Charge. *Sov. Phys. JETP*, 26(5):984–988, 11 1968. URL http://jetp.ac.ru/cgi-bin/dn/e_026_05_0984.pdf.

[16] Z. Maki et al. Remarks on the Unified Model of Elementary Particles. *Prog. Theor. Phys.*, 28(5):870–880, 11 1962. ISSN 0033-068X. doi: 10.1143/PTP.28.870. URL https://doi.org/10.1143/PTP.28.870.

[17] E. K. Akhmedov and A. Y. Smirnov. Paradoxes of neutrino oscillations. *Physics of Atomic Nuclei*, 72:1363–1381, 8 2009. doi: 10.1134/S1063778809080122. URL https://link.springer.com/article/10.1134/S1063778809080122.

[18] M. Tanabashi et al. (Particle Data Group). Review of Particle Physics. *Phys. Rev. D*, 98, 030001, 2018. ISSN 2470-0010. doi: 10.1103/PhysRevD.98.030001. URL https://journals.aps.org/prd/abstract/10.1103/PhysRevD.98.030001.

[19] A. Bellerive. Review of solar neutrino experiments. *Int. J. Mod. Phys. A*, 19:1167–1179, 2004. doi: 10.1142/S0217751X04019093. URL https://www.worldscientific.com/doi/abs/10.1142/S0217751X04019093.

[20] E. K. Akhmedov et al. Atmospheric neutrinos at super-Kamiokande and parametric resonance in neutrino oscillations. *Nucl. Phys. B*, 542:3–30, 1999. doi: 10.1016/S0550-3213(98)00825-6. URL https://www.sciencedirect.com/science/article/pii/S0550321398008256.

[21] K. Abe et al. (Super-Kamiokande Collaboration). Solar neutrino measurements in Super-Kamiokande-IV. *Phys. Rev. D*, 94:052010, Sep 2016. doi: 10.1103/PhysRevD.94.052010. URL https://link.aps.org/doi/10.1103/PhysRevD.94.052010.

[22] J. Lesgourgues and S. Pastor. Massive neutrinos and cosmology. *Phys. Rep.*, 429(6):307 – 379, 2006. ISSN 0370-1573. doi: 10.1016/j.physrep.2006.04.001. URL http://www.sciencedirect.com/science/article/pii/S0370157306001359.

[23] D. Perkins. *Particle Astrophysics, Second Edition*. Oxford University Press, 2009. ISBN 978-0-19-954546-9.

[24] N. Aghanim et al. (Planck Collaboration). Planck 2018 results. VI. Cosmological parameters, 2018. URL https://arxiv.org/pdf/1807.06209.pdf.

[25] J. Engel and J. Menéndez. Status and future of nuclear matrix elements for neutrinoless double-beta decay: A review, 2017. URL https://arxiv.org/abs/1610.06548.

[26] M. Agostini et al. (GERDA Collaboration). Probing majorana neutrinos with double-β decay. *Science*, 365:1445–1448, Jul 2019. doi: 10.1126/science.aac8613. URL https://science.sciencemag.org/content/365/6460/1445.

[27] G. Drexlin. Direct neutrino mass measurement. talk at Topics in Astroparticle and Underground Physics (TAUP), 2019. URL http://www-kam2.icrr.u-tokyo.ac.jp/indico/event/3/contribution/27/material/slides/0.pdf.

[28] L. Gastaldo et al. The electron capture in ^{163}Ho experiment — ECHo. *The European Physical Journal Special Topics*, 226(8):1623–1694, Jun 2017. ISSN 1951-6401. doi: 10.1140/epjst/e2017-70071-y. URL https://doi.org/10.1140/epjst/e2017-70071-y.

[29] M. Aker et al. (KATRIN Collaboration). An improved upper limit on the neutrino mass from a direct kinematic method by KATRIN. *Phys. Rev. Lett*, 123 (22), 2019. ISSN 221802. doi: 10.1103/PhysRevLett.123.221802. URL https://journals.aps.org/prl/abstract/10.1103/PhysRevLett.123.221802.

[30] M. Arenz et al. (KATRIN Collaboration). First transmission of electrons and ions through the KATRIN beamline. *Journal of Instrumentation*, 13 (04):P04020–P04020, Apr 2018. doi: 10.1088/1748-0221/13/04/p04020. URL https://doi.org/10.1088%2F1748-0221%2F13%2F04%2Fp04020.

[31] J. Behrens. *Design and commissioning of a monoenergetic photoelectron source and active background reduction by magnetic pulse at the KATRIN experiment*. PhD thesis, WWU, Münster, 2016. URL https://www.katrin.kit.edu/publikationen/phd_behrens.pdf.

[32] M. Röllig. *Tritium analytics by beta induced X-ray spectrometry*. PhD thesis, 2015. URL https://publikationen.bibliothek.kit.edu/1000054050. 51.03.01; LK 01.

[33] R. Gehring et al. The Windowless Gaseous Tritium Source for the KATRIN Experiment. *IEEE T. Appl. Supercon.*, 18(2):1459–1462, June 2008. ISSN 2378-7074. doi: 10.1109/TASC.2008.920625. URL https://ieeexplore.ieee.org/abstract/document/4518944?section=abstract.

[34] M. Schlösser et al. Online Laser-Raman-Spektroskopie an Tritium für KATRIN. Frühjahrstagung DPG, Fachverband Quantenoptik und Photonen, Hannover, 8.-12. März 2010 Verhandlungen der Deutschen Physikalischen Gesellschaft, R.6, B.45(2010) Q 54.6, 2010. URL http://bibliothek.fzk.de/zb/veroeff/79333.pdf. 51.54.01; LK 02.

[35] M. Schlösser et al. Accurate calibration of the laser Raman system for the Karlsruhe Tritium Neutrino Experiment. *J. Mol. Struct.*, 1044:61 – 66, 2013. ISSN 0022-2860. doi: 10.1016/j.molstruc.2012.11.022. URL http://www.sciencedirect.com/science/article/pii/S0022286012010629. MOLECULAR SPECTROSCOPY AND MOLECULAR STRUCTURE 2012.

[36] D. Vénos et al. Properties of ^{83m}Kr conversion electrons and their use in the KATRIN experiment. *J. Instrum.*, 13(02):T02012–T02012, Feb 2018. doi: 10.1088/1748-0221/13/02/t02012. URL https://doi.org/10.1088%2F1748-0221%2F13%2F02%2Ft02012.

[37] S. Lukić et al. Measurement of the gas-flow reduction factor of the KATRIN DPS2-F differential pumping section. *Vacuum*, 86(8):1126 – 1133, 2012. ISSN 0042-207X. doi: 10.1016/j.vacuum.2011.10.017. URL http://www.sciencedirect.com/science/article/pii/S0042207X11003800.

[38] W. Gil et al. (KATRIN Collaboration). The Cryogenic Pumping Section of the KATRIN Experiment. *IEEE T. Appl. Supercon.*, 20(3):316–319, Jun

2010. ISSN 2378-7074. doi: 10.1109/TASC.2009.2038581. URL https://ieeexplore.ieee.org/document/5371979.

[39] M. Kleesiek. *A Data-Analysis and Sensitivity-Optimization Framework for the KATRIN Experiment*. PhD thesis, Karlsruhe Institute of Technology, Karlsruhe, 2014. URL https://publikationen.bibliothek.kit.edu/1000043301.

[40] P. Kruit and F. H. Read. Magnetic field paralleliser for 2π electron-spectrometer and electron-image magnifier. *J. Phys. E Sci. Instrum.*, 16(4):313–324, Apr 1983. doi: 10.1088/0022-3735/16/4/016. URL https://doi.org/10.1088%2F0022-3735%2F16%2F4%2F016.

[41] T. Thümmler et al. Precision high voltage divider for the KATRIN experiment. *New Journal of Physics*, 11(10):103007, Oct 2009. doi: 10.1088/1367-2630/11/10/103007. URL https://doi.org/10.1088%2F1367-2630%2F11%2F10%2F103007.

[42] C. Rodenbeck. Calibration and Monitoring of KATRIN's Precision High Voltage System with First ^{83m}Kr Measurements. Master's thesis, Karlsruher Institut für Technologie (KIT), 2018. URL https://www.katrin.kit.edu/publikationen/mth-rodenbeck.pdf.

[43] J. F. Amsbaugh et al. Focal-plane detector system for the KATRIN experiment. *Nucl. Instrum. Meth. A*, 778:40 – 60, 2015. ISSN 0168-9002. doi: 10.1016/j.nima.2014.12.116. URL http://www.sciencedirect.com/science/article/pii/S0168900215000236.

[44] M. Aker et al. (KATRIN Collaboration). KATRIN Hardware Paper (working title). in prep., 2020.

[45] M. Kleesiek et al. β-Decay spectrum, response function and statistical model for neutrino mass mesaurement with the KATRIN experiment. *Eur. Phys. J. C*, 79, 2019. doi: 10.1140/epjc/s10052-019-6686-7. URL https://link.springer.com/article/10.1140%2Fepjc%2Fs10052-019-6686-7.

[46] C. Karl. Analysis of First Tritium Data of the KATRIN Experiment. Master's thesis, Technical University of Munich, 2018. URL https://www.katrin.kit.edu/publikationen/mth-karl.pdf.

[47] L. Schlüter. Development of New Methods to Include Systematic Effects in the First Tritium Data Analysis and Sensitivity Studies of the KATRIN Experiment. Master's thesis, Technical University of Munich, 2019. URL https://www.katrin.kit.edu/publikationen/SchlueterLisaMSc19%20(1).pdf.

[48] A. Saenz et al. Improved Molecular Final-State Distribution of HeT^+ for the β-Decay Process of T_2. *Phys. Rev. Lett.*, 84:242–245, Jan 2000. doi: 10.1103/PhysRevLett.84.242. URL https://link.aps.org/doi/10.1103/PhysRevLett.84.242.

[49] J. W. Liu. Total Inelastic Cross Section for Collisions of H_2 with Fast Charged Particles. *Phys. Rev. A*, 7:103–109, Jan 1973. doi: 10.1103/PhysRevA.7.103. URL https://link.aps.org/doi/10.1103/PhysRevA.7.103.

[50] S. Groh. *Modeling of the response function and measurement of transmission properties of the KATRIN experiment*. PhD thesis, Karlsruhe Institute of Technology, Karlsruhe, Feb 2015. URL https://publikationen.bibliothek.kit.edu/1000046546/3459156.

[51] D. F. R. Hilk. *Electric field simulations and electric dipole investigations at the KATRIN main spectrometer*. PhD thesis, Karlsruher Institut für Technologie (KIT), 2017. URL https://publikationen.bibliothek.kit.edu/1000065869.

[52] F. Heizmann. *Analysis tools and methods for tritium data taking with the KATRIN experiment*. PhD thesis, Karlsruher Institut für Technologie (KIT), 2019. URL https://publikationen.bibliothek.kit.edu/1000093536. 51.03.01; LK 01.

[53] Center for Experimental Nuclear Physics and Astrophysics University of Washington. Annual report, Apr 2014. URL https://www.npl.washington.edu/sites/default/files/annual-reports/2014-CENPA-Annual-Report.pdf.

[54] R. Brun and F. Rademakers. ROOT — An object oriented data analysis framework. *Nucl. Instrum. Meth. A*, 389(1):81 – 86, 1997. ISSN 0168-9002. doi: 10.1016/S0168-9002(97)00048-X. URL http://www.sciencedirect.com/science/article/pii/S016890029700048X. New Computing Techniques in Physics Research V.

[55] D. Furse et al. Kassiopeia: a modern, extensible C++ particle tracking package. *New J. Phys.*, 19(5):053012, May 2017. doi: 10.1088/1367-2630/aa6950. URL https://doi.org/10.1088%2F1367-2630%2Faa6950.

[56] L. Predrag et al. The Robin Hood method – A novel numerical method for electrostatic problems based on a non-local charge transfer. *J. Comput. Phys.*, 213 (1):117 – 140, 2006. ISSN 0021-9991. doi: 10.1016/j.jcp.2005.08.006. URL http://www.sciencedirect.com/science/article/pii/S0021999105003712.

[57] K. Altenmüller et al. (KATRIN Collaboration). High-resolution spectroscopy of gaseous ^{83m}Kr conversion electrons with the KATRIN experiment. *J. Phys. G*, 47(6), 2020. doi: 10.1088/1361-6471/ab8480. URL https://iopscience.iop.org/article/10.1088/1361-6471/ab8480.

[58] C. Köhler. Determination of the Column Density in the KATRIN Beamline with Electrons from the Photo-Electric Source. Master's thesis, Technical University of Munich, 2019.

[59] The HDF Group. Hierarchical Data Format, version 5, 1997-2020. URL http://www.hdfgroup.org/HDF5/.

[60] A. Pollithy and C. Karl. Analysis strategy and background in the KATRIN experiment, 2019. URL https://fuzzy.fzk.de/bscw/bscw.cgi/1294980?op=preview&back_url=1291548. poster at 698. WE-Heraeus-Seminar on 'Massive Neutrinos'.

[61] M. Aker et al. (KATRIN Collaboration). First operation of hte KATRIN experiment with tritium. *Eur. Phys. J. C*, 80(264), 2020. doi: 10.1140/epjc/s10052-020-7718-z. URL https://link.springer.com/article/10.1140%2Fepjc%2Fs10052-020-7718-z.

[62] S. Enomoto. Detector Analysis and Run Summary for KNM2. talk at the 37nd KATRIN Collaboration meeting, 2019. URL https://fuzzy.fzk.de/bscw/bscw.cgi/1305999?op=preview&back_url=1305884.

[63] S. Mertens et al. Background due to stored electrons following nuclear decays in the KATRIN spectrometers and its impact on the neutrino mass sensitivity. *Astropart. Phys.*, 41:52 – 62, 2013. ISSN 0927-6505. doi: 10.1016/j.astropartphys.2012.10.005. URL http://www.sciencedirect.com/science/article/pii/S0927650512001892.

[64] F. T. Harms. *Characterization and Minimization of Background Processes in the KATRIN Main Spectrometer*. PhD thesis, 2015. URL https://publikationen.bibliothek.kit.edu/1000050027. 51.03.01; LK 01.

[65] S. Mertens. *Study of Background Processes in the Electrostatic Spectrometers of the KATRIN Experiment*. PhD thesis, 2012. URL https://publikationen.bibliothek.kit.edu/1000027058.

[66] S. Görhardt et al. Impact of a cryogenic baffle system on the suppression of radon-induced background in the KATRIN pre-spectrometer. *J. Instrum.*, 13 (10):T10004–T10004, Oct 2018. doi: 10.1088/1748-0221/13/10/t10004. URL https://doi.org/10.1088%2F1748-0221%2F13%2F10%2Ft10004.

[67] F. M. Fränkle et al. Radon induced background processes in the KATRIN pre-spectrometer. *Astropart. Phys.*, 35(3):128 – 134, 2011. ISSN 0927-6505. doi: 10.1016/j.astropartphys.2011.06.009. URL http://www.sciencedirect.com/science/article/pii/S0927650511001290.

[68] N. Wandkowsky. *Study of background and transmission properties of the KATRIN spectrometers*. PhD thesis, Karlsruhe Institute of Technology, 2013. URL https://publikationen.bibliothek.kit.edu/1000036631.

[69] Bundesamt für Strahlenschutz, Radon in Innenräumen in Deutschland. URL https://www.bfs.de/DE/themen/ion/umwelt/radon/karten/innenraeume.html;jsessionid=5F1F742E33D98091E68742596E472AB0.1_cid391. Accessed: 2020-06-23.

[70] M. S. Rapaport et al. K-shell electron shake-off accompanying alpha decay. *Phys. Rev. C*, 11:1740–1745, May 1975. doi: 10.1103/PhysRevC.11.1740. URL https://link.aps.org/doi/10.1103/PhysRevC.11.1740.

[71] C. F. Liang et al. Configurations and level structure of ^{215}Po. *Phys. Rev. C*, 59:648–654, Feb 1999. doi: 10.1103/PhysRevC.59.648. URL https://link.aps.org/doi/10.1103/PhysRevC.59.648.

[72] G. Drexlin et al. Calculations and TPMC simulations of the reduction of radioactive decays of a noble gas by cryo-panels. *Vacuum*, 138, 12 2016. doi: 10.1016/j.vacuum.2016.12.013. URL https://www.sciencedirect.com/science/article/pii/S0042207X16309873?via%3Dihub.

[73] N. R.-M. Trost. *Modeling and measurement of Rydberg-State mediated Background at the KATRIN Main Spectrometer*. PhD thesis, Karlsruher Institut für Technologie (KIT), 2019. URL https://publikationen.bibliothek.kit.edu/1000090450. 51.03.01; LK 01.

[74] M. Arenz et al. (KATRIN Collaboration). Reduction of stored-particle background by a magnetic pulse method at the KATRIN experiment. *Eur. Phys. J. C*, 78(9):778, Sep 2018. ISSN 1434-6052. doi: 10.1140/epjc/s10052-018-6244-8. URL https://doi.org/10.1140/epjc/s10052-018-6244-8.

[75] M. Kraus. *Energy-Scale Systematics at the KATRIN Main Spectrometer*. PhD thesis, Karlsruher Institut für Technologie (KIT), 2016. URL https://publikationen.bibliothek.kit.edu/1000054447.

[76] D. Hinz and T. Thümmler. Radioactivity indcued backgrond electrons in the KATRIN spectrometers, 2019. URL https://fuzzy.fzk.de/bscw/bscw.cgi/1291676?op=preview&back_url=1291166. poster at 698. WE-Heraeus-Seminar on 'Massive Neutrinos'.

[77] A. Osipowicz. SRIM simulations on alpha recoil nuclei in the main spectrometer. talk at the 32nd KATRIN Collaboration meeting, 2017. URL https://fuzzy.fzk.de/bscw/bscw.cgi/1079947?op=preview&back_url=1079816.

[78] D. Hinz. Ionisation mechanisms of ^{206}Pb induced Rydberg atoms. Master's thesis, Karlsruhe Institute of Technology, 2018. URL https://www.katrin.kit.edu/publikationen/mth-hinz.pdf.

[79] F. Fränkle. SDS3 measurements - status and outlook. talk at 32nd KATRIN Collaboration meeting, 2016. URL https://fuzzy.fzk.de/bscw/bscw.cgi/1079599?op=preview&back_url=1079553.

[80] F. Fränkle et al. KATRIN background due to surface radioimpurities. in prep., 2020.

[81] A. Müller. Investigation of the secondary electron emission characteristics of the KATRIN main spectrometer. Master's thesis, Karlruhe Insititue of Technology, 2016. URL https://www.katrin.kit.edu/publikationen/mth_mueller_axel.pdf.

[82] M. L. Yu. *Charged and excited states of sputtered atoms*, pages 91–160. Springer Berlin Heidelberg, Berlin, Heidelberg, 1991. ISBN 978-3-540-46881-3. doi: 10.1007/3540534288_17. URL https://doi.org/10.1007/3540534288_17.

[83] R. Kelly. On the origin of sputtered excited atoms. *Nucl. Instrum. Methods*, 194(1):583 – 588, 1982. ISSN 0167-5087. doi: 10.1016/0029-554X(82)90585-7. URL http://www.sciencedirect.com/science/article/pii/0029554X82905857.

[84] F. Friedel et al. Time-dependent simulation of the flow reduction of D2 and T2 in the KATRIN experiment. *Vacuum*, 159:161 – 172, 2019. ISSN 0042-207X. doi: 10.1016/j.vacuum.2018.10.002. URL http://www.sciencedirect.com/science/article/pii/S0042207X18313873.

[85] M. Klein and F. Glück. Tritium ion blocking and detection in the KATRIN experiment. *J. Phys. Conf. Ser.*, 888:012073, Sep 2017. doi: 10.1088/1742-6596/888/1/012073. URL https://doi.org/10.1088%2F1742-6596%2F888%2F1%2F012073.

[86] M. Klein. *Tritium ions in KATRIN: blocking, removal and detection*. PhD thesis, Karlsruher Institut für Technologie (KIT), 2019. URL https://publikationen.bibliothek.kit.edu/1000093526. 51.03.01; LK 01.

[87] M. A. Furman and M. T. F. Pivi. Probabilistic model for the simulation of secondary electron emission. *Phys. Rev. Spec. Top.-Ac.*, 5:124404, Dec 2002. doi: 10.1103/PhysRevSTAB.5.124404. URL https://link.aps.org/doi/10.1103/PhysRevSTAB.5.124404.

[88] K. Valerius. Electromagnetic design and inner electrode for the KATRIN main spectrometer. *Prog. Part. Nucl. Phys.*, 57(1):58 – 60, 2006. ISSN 0146-6410. doi: 10.1016/j.ppnp.2005.11.011. URL http://www.sciencedirect.com/science/article/pii/S0146641005001353. International Workshop of Nuclear Physics 27th course.

[89] M. Arenz et al. (KATRIN Collaboration). Commissioning of the vacuum system of the KATRIN main spectrometer. *J. Instrum.*, 11(04):P04011–P04011, Apr 2016. doi: 10.1088/1748-0221/11/04/p04011. URL https://doi.org/10.1088%2F1748-0221%2F11%2F04%2Fp04011.

[90] K. Altenmüller et al. (KATRIN Collaboration). Muon-induced background in the KATRIN main spectrometer. *Astropart. Phys.*, 108:40 – 49, 2019. ISSN 0927-6505. doi: 10.1016/j.astropartphys.2019.01.003. URL http://www.sciencedirect.com/science/article/pii/S0927650518302597.

[91] K. Altenmüller et al. (KATRIN Collaboration). Gamma-induced background in the KATRIN main spectrometer. *Eur. Phys. J. C*, 79:807, 2019. doi: 10.1140/epjc/s10052-019-7320-4. URL https://link.springer.com/article/10.1140%2Fepjc%2Fs10052-019-7320-4.

[92] B. Leiber. *Investigations of background due to secondary electron emission in the KATRIN-experiment*. PhD thesis, 2014. URL https://publikationen.bibliothek.kit.edu/1000042415.

[93] J. S. Schwarz. *The Detector System of the KATRIN Experiment - Implementation and First Measurements with the Spectrometer*. PhD thesis, 2014. URL https://publikationen.bibliothek.kit.edu/1000042772.

[94] F. M. Fränkle et al. Penning discharge in the KATRIN pre-spectrometer. *J. Instrum.*, 9(07):P07028–P07028, Jul 2014. doi: 10.1088/1748-0221/9/07/p07028. URL https://doi.org/10.1088%2F1748-0221%2F9%2F07%2Fp07028.

[95] K. Valerius. *Spectrometer-related background processes and their suppression in the KATRIN experiment*. PhD thesis, Westfälische Universität Münster, 2009. URL http://repositorium.uni-muenster.de/document/miami/93137705-73f4-404a-a438-09d487cbff63/diss_valerius.pdf.

[96] M. Aker et al. (KATRIN Collaboration). Suppression of Penning discharges between the KATRIN spectrometers, 2019. URL https://arxiv.org/abs/1911.09633. submitted to Eur. Phys. J. C.

[97] A. Schwemmer. Master's thesis, Ludwig-Maximilians-Universität München, München, 2020. in prep.

[98] S. Dyba. *Background reduction by the inner wire electrode and set-up of the condensed krypton source at the neutrino mass experiment KATRIN*. PhD thesis, WWU, Münster, 2019. URL https://repositorium.uni-muenster.de/document/miami/4a73b204-96e6-4922-9d88-a640cd4ad191/diss_dyba.pdf.

[99] L. Schimpf. KATRIN Analysis Report - GKrS transmission function analysis. Internal report, 2017. URL https://fuzzy.fzk.de/bscw/bscw.cgi/d1208984/Schimpf-GKrS-transmission-function.pdf.

[100] J. Behrens. Another look at the Transmission Function. talk at 34th KATRIN Collaboration meeting, 2018. URL https://fuzzy.fzk.de/bscw/bscw.cgi/d1196192/95-TRP-6418-P4-JBehrens.pdf.

[101] F. M. Penning. Über Ionisation durch metastabile Atome. *Naturwissenschaften*, 15:815, 1927. doi: 10.1007/BF01505431. URL https://link.springer.com/content/pdf/10.1007/BF01505431.pdf.

[102] M. J. Shaw. Penning ionization. *Contemp. Phys.*, 15, 1974. doi: 10.1080/00107517408210804. URL https://www.tandfonline.com/doi/abs/10.1080/00107517408210804.

[103] H. Hotop et al. Penning electron spectra from ionization of hydrogen atoms by He(2^1S) and He(2^3S) metastables. *Chem. Phys. Lett.*, 10(5):493 – 497, 1971. ISSN 0009-2614. doi: 10.1016/0009-2614(71)87021-5. URL http://www.sciencedirect.com/science/article/pii/0009261471870215.

[104] M. R. Flannery et al. Long-range interaction between polar rydberg atoms. *J. Phy. B-At. Mol. Opt.*, 38(2):S279–S293, Jan 2005. doi: 10.1088/0953-4075/38/2/020. URL https://doi.org/10.1088%2F0953-4075%2F38%2F2%2F020.

[105] F. Robicheaux. Ionization due to the interaction between two rydberg atoms. *J. Phys. B-At. Mol. Opt.*, 38(2):S333–S342, Jan 2005. doi: 10.1088/0953-4075/38/2/024. URL https://doi.org/10.1088%2F0953-4075%2F38%2F2%2F024.

[106] R. E. Olsen. Ionization Cross Sections for Rydberg-Atom-Rydberg-Atom Collisions. *Phys. Rev. Lett.*, 43:126–129, Jul 1979. doi: 10.1103/PhysRevLett.43.126. URL https://link.aps.org/doi/10.1103/PhysRevLett.43.126.

[107] J. E. Collin. Autoionization in atomic and molecular physics. *Endeavour*, 1(3):122 – 128, 1977. ISSN 0160-9327. doi: 10.1016/0160-9327(77)90170-3. URL http://www.sciencedirect.com/science/article/pii/0160932777901703.

[108] T. Jahnke. Interatomic and intermolecular coulombic decay: the coming of age story. *J. Phys. B-At. Mol. Opt.*, 48(8):082001, Mar 2015. doi: 10.1088/0953-4075/48/8/082001. URL https://doi.org/10.1088%2F0953-4075%2F48%2F8%2F082001.

[109] K. Gokhberg et al. Site- and energy-selective slow-electron production through intermolecular Coulombic decay. *Nature*, 505:661–663, 2014. doi: 10.1038/nature12936. URL https://www.nature.com/articles/nature12936#citeas.

[110] J. Titze et al. Ionization Dynamics of Helium Dimers in Fast Collisions with He^{++}. *Phys. Rev. Lett.*, 106:033201, Jan 2011. doi: 10.1103/PhysRevLett.106.033201. URL https://link.aps.org/doi/10.1103/PhysRevLett.106.033201.

[111] S. Scheit et al. Time-dependent interplay between electron emission and fragmentation in the interatomic Coulombic decay. *J. Chem. Phys.*, 118, 2003. doi: 10.1063/1.1531996. URL https://aip.scitation.org/doi/10.1063/1.1531996.

[112] I. V. Hertel et al. *Atoms, Molecules and Optical Physics 1*. Springer, 2016. URL https://www.springer.com/de/book/9783642543210.

[113] R. Guillemin et al. Doppler effect in fragment autoionization following core-to-valence excitation in o_2. *Phys. Rev. A*, 82:051401, Nov 2010. doi: 10.1103/PhysRevA.82.051401. URL https://link.aps.org/doi/10.1103/PhysRevA.82.051401.

[114] T. Day Goodacre et al. The identification of autoionizing states of atomic chromium for the resonance ionization laser ion source of the ISOLDE radioactive ion beam facility. *Spectrochim. Acta B*, 129:58 – 63, 2017. ISSN 0584-8547. doi: 0.1016/j.sab.2017.01.001. URL http://www.sciencedirect.com/science/article/pii/S0584854717300095.

[115] E. F. Worden et al. The ionization potential of neutral iron, Fe i, by multistep laser spectroscopy. *J. Opt. Soc. Am. B*, 1(2):314–316, Apr 1984. doi: 10.1364/JOSAB.1.000314. URL http://josab.osa.org/abstract.cfm?URI=josab-1-2-314.

[116] M. A. Bautista. Atomic data from the Iron Project. XVI. Photoionization cross sections and oscillator strengths for Fe V. *Astron. Astrophys. Suppl. Ser.*, 119:105–110, 1996. doi: 10.1051/aas:1996231. URL https://aas.aanda.org/articles/aas/abs/1996/13/ds1134/ds1134.html.

[117] I. C. Percival. Planetary atoms. *P. Roy. Soc. A-Math. Phy.*, 1977. doi: 10.1098/rspa.1977.0035. URL https://royalsocietypublishing.org/doi/abs/10.1098/rspa.1977.0035.

[118] A. Bürgers and D. Wintgen. Inhibited autoionization of planetary atom states. *J. Phys. B-At. Mol. Opt.*, 27(8):L131–L135, Apr 1994. doi: 10.1088/0953-4075/27/8/001. URL https://doi.org/10.1088%2F0953-4075%2F27%2F8%2F001.

[119] D. Hinz. PhD thesis, Karlsruhe Institute of Technology, 2022. in prep.

[120] M. J. G. Borge and K. Blaum. Focus on exotic beams at ISOLDE: A laboratory portrait. *Journal of Physics G: Nuclear and Particle Physics*, 45(1):010301, Nov 2017. doi: 10.1088/1361-6471/aa990f. URL https://doi.org/10.1088%2F1361-6471%2Faa990f.

[121] H. Bateman. The solutions of differential equations occurring in the theory of radioactive transformations. In *Proceedings of the Cambridge Philosphical Society, Mathematical and phyiscal scicences*, pages 423–427, 1910. URL https://archive.org/details/cbarchive_122715_solutionofasystemofdifferentia1843/mode/2up.

[122] G. B. Saha. *Physics and Radiobiology of Nuclear Medicine*. Springer, 2006. ISBN 978-0-387-36281-6. doi: 10.1007/978-0-387-36281-6. URL https://link.springer.com/book/10.1007/978-0-387-36281-6.

[123] H. W. Kirby et al. Half-life of radium-223. *J. Inorg. Nucl. Chem.*, 27(9):1881 – 1887, 1965. ISSN 0022-1902. doi: 10.1016/0022-1902(65)80039-2. URL http://www.sciencedirect.com/science/article/pii/0022190265800392.

[124] P. M. Aitken-Smith and S. M. Collins. Measurement of the 211Pb half-life using recoil atoms from 219Rn decay. *Appl. Radiat. Isotopes*, 110:59 – 63, 2016. ISSN 0969-8043. doi: 10.1016/j.apradiso.2016.01.004. URL http://www.sciencedirect.com/science/article/pii/S0969804316300045.

[125] T. Corona. *Methodology and application of high performance electrostatic field simulation in the KATRIN experiment*. PhD thesis, University of North Carolina at Chapel Hill, 2014. URL https://cdr.lib.unc.edu/concern/parent/7s75dd144/file_sets/tx31qj30s.

[126] A. V. Lokhov and F. V. Tkachov. Confidence intervals with a priori paramter bounds. *Phys. Part. Nuclei*, 46:347–365, 2015. doi: 10.1134/S1063779615030089. URL https://link.springer.com/article/10.1134%2FS1063779615030089.

[127] M. Aker et al. (KATRIN Collaboration). Analysis methods for the first KATRIN direct kinematic neutrino mass measurement. in prep., 2020.

[128] F. Fränkle et al. KATRIN Executive Board Report, WG1: SDS3 'Christmas measurement' analysis. Internal report, 2018. URL https://ikp-katrin-wiki.ikp.kit.edu/katrin/images/9/9e/SDS3Xmas180123.pdf.

[129] B. Efron and R. T. Tibshirani. *An Introduction to the Bootstrap*. Chapman & Hall, 1994.

[130] F. Block. Characterisation of the Background in the KATRIN Experiment. Master's thesis, Karlsruhe Institute of Technology, 2018. URL https://www.katrin.kit.edu/publikationen/mth_fblock.pdf.

[131] T. Thümmler. SDS Status 2020. talk at 38th KATRIN Collaboration meeting, 2020. URL https://fuzzy.fzk.de/bscw/bscw.cgi/1318629?op=preview&back_url=1318494.

[132] M. G. Erhard. *Influence of the magnetic field on the transmission characteristics and the neutrino mass systematic of the KATRIN experiment*. PhD thesis, Karlsruher Institut für Technologie (KIT), 2016. URL https://publikationen.bibliothek.kit.edu/1000065003.

[133] A. Lokhov. Shifted analyzing plane: measurements and simulation. talk at 37th KATRIN Collaboration meeting, 2019. URL https://fuzzy.fzk.de/bscw/bscw.cgi/1306297?op=preview&back_url=1306251.